

AD-A195 333

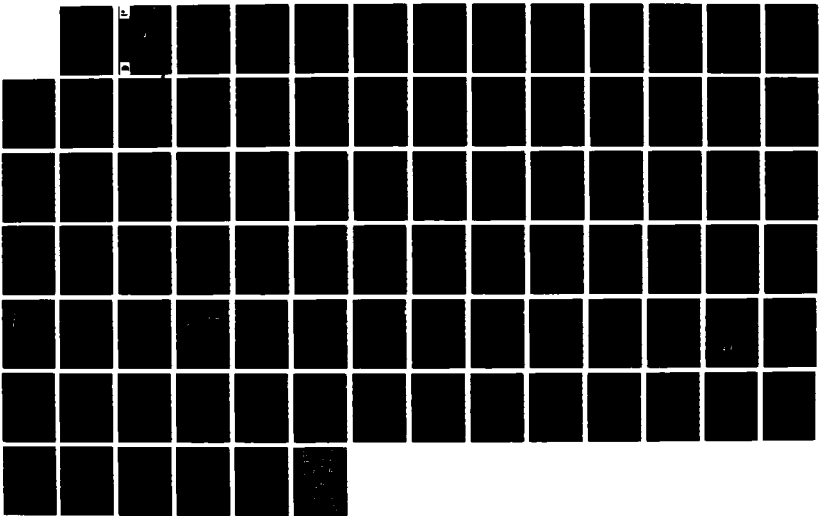
AN IMPLICIT FINITE DIFFERENCE FORMULATION FOR TREATING
MULTIPHASE FLOW IN WET POROUS SOILS(U) CALIFORNIA
RESEARCH AND TECHNOLOGY INC CHATSWORTH P J HASSIG
APR 88 WES/CR/5L 88-2

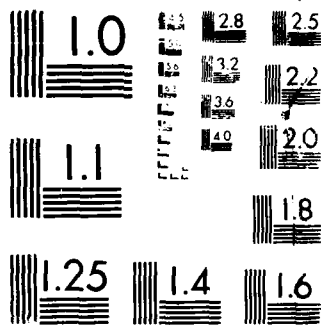
1/1

UNCLASSIFIED

F/G 8/18

NL





MICROCOPY RESOLUTION TEST CHART
NATIONAL BUREAU OF STANDARDS-1963-A



US Army Corps
of Engineers

AD-A195 333

DTIC FILE COPY (2)

CONTRACT REPORT SL-88-2

AN IMPLICIT FINITE DIFFERENCE FORMULATION FOR TREATING MULTIPHASE FLOW IN WET POROUS SOILS

by

Paul J. Hassig

California Research and Technology, Inc.
20943 Devonshire Street
Chatsworth, California 91311-2376

DTIC
SELECTED
MAY 24 1988
S D
C&D



April 1988

Final Report

Approved For Public Release Distribution Unlimited

Prepared for DEPARTMENT OF THE ARMY
US Army Corps of Engineers
Washington, DC 20314-1000

Contract Project No. 4A162784A140, Task AO, Work Unit 026
(Contract No. DACA 89-84-D 0003)

Monitored by Structures Laboratory
US Army Engineer Waterways Experiment Station
PO Box 631, Vicksburg, Mississippi 39180-0631



Unclassified
 SECURITY CLASSIFICATION OF THIS PAGE

REPORT DOCUMENTATION PAGE				
1a. REPORT SECURITY CLASSIFICATION Unclassified		1b. RESTRICTIVE MARKINGS		
2a. SECURITY CLASSIFICATION AUTHORITY		3. DISTRIBUTION / AVAILABILITY OF REPORT Approved for public release; distribution unlimited.		
2b. DECLASSIFICATION / DOWNGRADING SCHEDULE				
4. PERFORMING ORGANIZATION REPORT NUMBER(S) CRT3140-F		5. MONITORING ORGANIZATION REPORT NUMBER(S) Contract Report SL-88-2		
6a. NAME OF PERFORMING ORGANIZATION California Research & Technology, Inc.	6b. OFFICE SYMBOL (if applicable)	7a. NAME OF MONITORING ORGANIZATION USAEWES Structures Laboratory		
6c. ADDRESS (City, State, and ZIP Code) 20943 Devonshire Street Chatsworth, CA 91311-2376		7b. ADDRESS (City, State, and ZIP Code) PO Box 631 Vicksburg, MS 39180-0631		
8a. NAME OF FUNDING / SPONSORING ORGANIZATION US Army Corps of Engineers	8b. OFFICE SYMBOL (if applicable)	9. PROCUREMENT INSTRUMENT IDENTIFICATION NUMBER DACA39-84-D-0003		
8c. ADDRESS (City, State, and ZIP Code) 20 Massachusetts Avenue, N.W. Washington, DC 20314-1000		10. SOURCE OF FUNDING NUMBERS		
		PROGRAM ELEMENT NO.	PROJECT NO. 4A162784AT40	TASK NO. A0
				WORK UNIT ACCESSION NO. 026
11. TITLE (Include Security Classification) An Implicit Finite Difference Formulation for Treating Multiphase Flow in Wet Porous Soils				
12. PERSONAL AUTHOR(S) Hassig, Paul J.				
13a. TYPE OF REPORT Final report	13b. TIME COVERED FROM Jun 87 TO Oct 87	14. DATE OF REPORT (Year, Month, Day) April 1988	15. PAGE COUNT 89	
16. SUPPLEMENTARY NOTATION Available from National Technical Information Service, 5285 Port Royal Road, Springfield, VA 22161.				
17. COSATI CODES			18. SUBJECT TERMS (Continue on reverse if necessary and identify by block number)	
FIELD	GROUP	SUB-GROUP		
			See reverse.	
19. ABSTRACT (Continue on reverse if necessary and identify by block number)				
<p>→ A one-dimensional (1-D) implicit multiphase finite difference formulation which calculates the relative flow and dynamic stress behavior in wet porous soils has been developed and incorporated into a computer code called CRIME. Various 1-D test cases are presented which demonstrate the ability of CRIME to efficiently calculate to very late times with time steps much larger (factors > 1000) than permitted by standard explicit techniques. In particular, the loading and subsequent consolidation of a realistic layered geology of varying saturation has been successfully simulated.</p> <p>The basic approach is to characterize the geologic materials in terms of both solid (soil lattice) and pore-fluid properties. A variety of constitutive models can be used to describe the effective stress behavior of the soil lattice. (e.g., linear-elastic, WES cap-type elastic-plastic, etc.). The pore-fluid properties are those of water and/or air with separate hydrodynamic equations of state (EOS) for each. In the case of partially</p> <p style="text-align: right;">(Continued)</p>				
20. DISTRIBUTION / AVAILABILITY OF ABSTRACT <input checked="" type="checkbox"/> UNCLASSIFIED/UNLIMITED <input type="checkbox"/> SAME AS RPT. <input type="checkbox"/> DTIC USERS		21. ABSTRACT SECURITY CLASSIFICATION Unclassified		
22a. NAME OF RESPONSIBLE INDIVIDUAL		22b. TELEPHONE (Include Area Code)		22c. OFFICE SYMBOL

18. SUBJECT TERMS (Continued)

Consolidation
Effective stress
Ground motion
Implicit finite difference
Multiphase constitutive model
Multiphase flow
Pore pressure
Wet porous soils

19. ABSTRACT (Continued)

saturated soils, a pressure equilibrium condition is used for the water-air mixture EOS in the soil pores. The relative flow of pore-fluid through the soil lattice is governed by internal "drag" interaction forces which reduce to Darcy's Law for the special case of steady flow. The soil permeability, the pore-fluid pressure and effective stress gradients, and the pore-fluid viscosity all determine the relative flow velocity.

7.

Instructions For	
NEWS GRA&I	<input checked="" type="checkbox"/>
DIC TAB	<input type="checkbox"/>
Unannounced	<input type="checkbox"/>
Justified	
Date	
By	
Availability Codes	
Dist	Avail and/or Special
A-1	



PREFACE

Work reported herein was performed by California Research and Technology, Inc., (CRT) during the period June 1987 through October 1987 for the US Army Engineer Waterways Experiment Station (WES) under Contract No. DACA39-84-D-0003 (Task A-6, Item 0034). It was sponsored by the Office, Chief of Engineers, US Army, as a part of Project 4A162784AT40, Task A0, Work Unit 026, "Blast-Induced Soil Liquefaction Effects on Hardened Structures and Obstacle Craters."

Mr. Paul J. Hassig was the CRT Principal Investigator for this study which involved development of a one-dimensional implicit numerical technique for solving the dynamic conservation equations for a multiphase (solid/fluid) system, including the relative flow of fluid and soil. The resulting computer code is called CRIME. Mr. Martin Rosenblatt and Dr. Douglas Hatfield provided invaluable support and assistance in the preliminary calculations which led to the development of CRIME. Mr. Hassig prepared this report with the help of Ms. JoAnne Clark, who prepared the figures. The work was technically supported and monitored by Dr. G. Y. Baladi of the Geomechanics Division, Structures Laboratory (SL), WES. Dr. Y. Marvin Ito was the CRT Project Manager for Contract No. DACA39-84-D-0003; Dr. J. G. Jackson, Jr., was the WES Contracting Officer's Representative. Mr. Bryant Mather is Chief, SL.

COL Dwayne G. Lee, CE, is Commander and Director of WES. Dr. Robert W. Whalin is WES Technical Director.

TABLE OF CONTENTS

	PAGE
PREFACE.....	i
CONVERSION FACTORS, NON-SI TO SI (METRIC) UNITS OF MEASUREMENT.....	iii
CHAPTER 1 INTRODUCTION.....	1
CHAPTER 2 METHODOLOGY.....	3
2.1 GOVERNING EQUATIONS.....	3
2.2 APPROACH.....	6
2.3 FINITE DIFFERENCING.....	9
CHAPTER 3 NUMERICAL RESULTS.....	19
3.1 EFFECTIVE STRESS DEVIATORS.....	19
3.2 RELATIVE FLOW AND LATE TIME STRESS REDISTRIBUTION.....	21
3.3 COMPARISON CALCULATION.....	23
3.4 LAYERED GEOLOGY WITH VARYING SATURATION.....	24
CHAPTER 4 SUMMARY, CONCLUSIONS, AND RECOMMENDATIONS....	77
REFERENCES.....	80

**CONVERSION FACTORS, NON-SI TO
SI (METRIC) UNITS OF MEASUREMENT**

Non-SI units of measurement used in this report can be converted to SI (metric) units as follows:

<u>Multiply</u>	<u>By</u>	<u>To Obtain</u>
feet	0.3048	metres
feet per second (ft/sec)	0.3048	metres per second
g's (standard free fall)	9.806650	metres per second squared
inches	25.4	millimetres
kips (force)	4.448222	kilonewtons
kips (force) per square inch	6.894757	megapascals
pounds (mass)	0.4535924	kilograms

AN IMPLICIT FINITE DIFFERENCE FORMULATION FOR
TREATING MULTIPHASE FLOW IN WET POROUS SOILS

CHAPTER 1

INTRODUCTION

The effects of multiphase flow on the cratering and ground motions in response to surface bursts (conventional and nuclear) in layered saturated soils is not yet fully understood. The typical state-of-the-art cratering calculations are just beginning to address the multiphase aspects with regards to the constitutive relationships (material models) which describe the wet soil behavior. Initial attempts describe the total stress behavior of a wet soil layer and the effective stress behavior of the soil lattice, enabling the separate determination of the pore-fluid pressures (Reference 1).

The M-DICE code was developed to further examine the multiphase issues by including separate models of the pore-fluid pressures and soil lattice effective stress behavior. More importantly, the relative flow of the pore-fluid and soil lattice is also treated by calculating the separate flow of each, including their mutual interactions due to drag. With this fully multiphase modeling, the M-DICE code was used to calculate the ground motions and crater formation from the MISERS BLUFF II-1 high-explosive test event and from a postulated 1 Mt nuclear surface burst (References 2-5).

Both M-DICE calculations went beyond the time most cratering codes stop. In so doing, they showed the existence of significant residual pore pressures and associated relative velocities, particularly in the 1 Mt nuclear calculation. The subsequent dissipation and redistribution of these excess pore

pressures provide a potential mechanism for significant late time ground motions, including further slumping of the crater slopes and surface settlements.

Current explicit numerical methodologies are not practical for calculating to very late times, as the time step is limited by stress wave speeds. Implicit numerical techniques should remove the explicit time step limitation, allowing for much larger time steps (factors of 1000 or more), limited perhaps only by the particle velocities. Our ultimate objective is to develop such a multiphase implicit formulation in two dimensions (2-D) in order to efficiently calculate relative flow and stress redistribution in wet porous soils. The focus of the current study is the development of a suitable technique in one dimension (1-D). The resulting finite-difference code is called **CRIME** (California Research Implicit Multiphase Eulerian).

The implicit multiphase formulation is discussed in Chapter 2 of this report. Various 1-D numerical test results are presented in Chapter 3. A summary is provided in Chapter 4 along with conclusions and recommendations.

CHAPTER 2

METHODOLOGY

2.1 GOVERNING EQUATIONS

The following equations summarize the 1-D conservation equations for mass and momentum for a solid-fluid multiphase system (energy and gravitational considerations are ignored for simplicity). The equations are presented in differential form. The subscripts f and s refer to the fluid phase and solid phase, respectively.

$$\frac{\partial}{\partial t} (\rho_f) = - \frac{\partial}{\partial x} (\rho_f u_f) \quad (1)$$

$$\frac{\partial}{\partial t} (\rho_s) = - \frac{\partial}{\partial x} (\rho_s u_s) \quad (2)$$

$$\frac{\partial}{\partial t} (\rho_f u_f) = - \frac{\partial}{\partial x} (\rho_f u_f u_f) - D (u_f - u_s) - \nu_f \frac{\partial}{\partial x} (P_f) \quad (3)$$

$$\begin{aligned} \frac{\partial}{\partial t} (\rho_s u_s) = & - \frac{\partial}{\partial x} (\rho_s u_s u_s) + D (u_f - u_s) - \nu_s \frac{\partial}{\partial x} (P_f) \\ & - \frac{\partial}{\partial x} (P_s) + \frac{\partial}{\partial x} (S_x) \end{aligned} \quad (4)$$

where ρ is the average (or bulk) density,
 u is the velocity,
 D is the local drag force coefficient,
 P_f is the pore-fluid pressure,
 P_s is the effective mean normal stress (pressure) of the solid phase,
 S_x is the effective stress deviator of the solid phase (negative for compression), and
 ν is the local area/volume fraction of each phase.

The total stress of the multiphase material is modeled in terms of the effective stress of the solid (soil lattice) and pore-fluid pressure. A constitutive model is used to describe the effective stress behavior of the solid soil lattice. Separate hydrodynamic equations of state (EOS) are used for the water and/or air to describe the pore-fluid pressures. In the case of partially saturated soils, a pressure equilibrium model is used for the water/air mixture EOS in the pores. Thus, a fully 3-phase model involving water-air-solid is used.

The following equations summarize the multiphase equations of state for the fluid phase (pore pressure) and solid phase (effective stress):

$$\frac{dP_f}{dt} = \frac{K_f}{\hat{\rho}_f} \frac{d\hat{\rho}_f}{dt} = \frac{K_f}{\rho_f} \left[\frac{d\rho_f}{dt} + \frac{1}{\rho_{sg}} \frac{\rho_f}{\nu_f} \frac{d\rho_s}{dt} \right] \quad (5)$$

$$\frac{dP_s}{dt} = -K_s \left[\frac{\partial u_s^k}{\partial x^k} \right] = \frac{K_s}{\rho_s} \frac{d\rho_s}{dt} \quad (6)$$

$$\begin{aligned} \frac{dS_x}{dt} &= 2G_s \left[\frac{\partial u_s}{\partial x} - \frac{1}{3} \left[\frac{\partial u_s^k}{\partial x^k} \right] \right] \\ &= 2G_s \frac{\partial u_s}{\partial x} + \frac{2}{3} \frac{G_s}{\rho_s} \frac{d\rho_s}{dt} \end{aligned} \quad (7)$$

where $\left[\frac{\partial u_s^k}{\partial x^k} \right] \equiv -\frac{1}{\rho_s} \frac{d\rho_s}{dt}$ is the velocity divergence,

$$\frac{d}{dt} \equiv \frac{\partial}{\partial t} + u^i \frac{\partial}{\partial x^i}$$

$\hat{\rho}_f \equiv \rho_f/\nu_f$ is the local pore-fluid density,

$\nu_f \equiv 1 - \nu_s \equiv 1 - \rho_s/\rho_{sg}$ is the porosity, and

ρ_{sg} is the average density of the individual soil grains (assumed constant).

The solid phase EOS (or material model) describes the effective stress behavior of the solid soil lattice. In general the bulk modulus, K_s , and shear modulus, G_s , are local functions of position and time, and depend on the nature of the transient loading/unloading behavior of the soil material. Some of the numerical examples presented in this study assume constant values for these moduli. Also used in this study is the cap-type constitutive model of Baladi and Barnes (Reference 1). This model relates incremental changes in strain (both plastic and elastic) to incremental changes in stress.

The fluid bulk modulus, K_f , is also considered to vary with position and time. For a dry soil, an adiabatic ideal gas equation of state is used to describe the pore air, such that

$$K_f = K_a = \gamma P_a \frac{\hat{\rho}_{a0}}{\hat{\rho}_a} \quad (8a)$$

The subscript o denotes initial values. For a saturated soil, a hydro-elastic equation of state is used to describe the water, such that

$$K_f = K_w = P_w \frac{\hat{\rho}_{w0}}{\hat{\rho}_w - \hat{\rho}_{w0}} \quad (8b)$$

For a partially saturated soil, a mixture equation of state assuming pressure equilibrium ($P_a=P_w$) is used, such that

$$\frac{\nu_f}{K_f} = \frac{\nu_a}{K_a} + \frac{\nu_w}{K_w} \quad (8c)$$

The drag force is primarily a function of the relative velocity, $u_r = u_f - u_s$, which results from the differential gradients in pore-fluid pressure and effective stress. The relative flow of the fluid with respect to the solid is also influenced by the physical properties of each material, i.e.,

solid phase permeability, porosity and particle size, as well as the viscosity of the pore-fluid. In this study a modified Darcy's law is used, relating the apparent volumetric fluid flow rate, $\nu_f u_r$, to the fluid pressure gradient, i.e.,

$$\frac{\partial P_f}{\partial x} = - \frac{\mu}{k} \left(\nu_f u_r \right) \quad (9)$$

where μ is the fluid viscosity [g/cm/s] and k is the local soil permeability [cm²].* If we assume a locally steady state and spatially uniform fluid momentum flux in Equation 3, substitution of Equation 9 into Equation 3 yields the following local drag coefficient:

$$D = \frac{\mu}{k} \left(\nu_f^2 \right) \quad (10)$$

The permeability is assumed to vary as a function of the local porosity (Reference 6), i.e.,

$$k = k_o \left(\frac{\nu_f}{\nu_{fo}} \right)^3 \left(\frac{\nu_{so}}{\nu_s} \right)^2 = k_o \frac{(1+e_o)}{(1+e)} \left(\frac{e}{e_o} \right)^3 \quad (11)$$

where $e \equiv \nu_f / \nu_s$ is the void ratio. Figure 2.1 shows the behavior of the permeability as a function of porosity for various initial porosities.

2.2 APPROACH

The finite-difference analogs of the time-dependent governing equations (1) to (7) describe the complete multiphase behavior at each grid location. In an explicit formulation the terms of the right hand side (r.h.s.) are known "time n" quantities and are used to obtain the left hand side (l.h.s.) "time n+1" quantities for a given time step. The resulting time n+1 densities and velocities are then used to get the final time

* Permeability units: 1 Darcy = 9.87×10^{-9} cm²
= 9.66×10^{-4} cm²/s (for water)

n+1 stresses (pressures and stress deviators), thus completing the integration over one time cycle.

In general, a numerical finite difference formulation of a time-dependent set of equations is considered "stable" if errors (truncation/round-off errors, etc.) do not amplify during the time integration calculation. Stability is usually assured by imposing restrictions on the size of the time step, i.e., they are "conditionally stable." For typical explicit formulations, the Courant-Friedrichs-Lewy (CFL) stability criterion requires the time step (Δt) to be less than the ratio of the grid spacing (Δx) to the stress wave speed (c), i.e.,

$$\Delta t_{\text{CFL}} \leq \Delta x / c \quad (12)$$

Note that for typical cratering and ground motion calculations, the stress wave speeds are determined by the local stress moduli. These wave speeds are usually much larger during the early times (characterized by megabar pressures) compared to the later times, thus allowing for increasing time steps during the course of the calculation.

Implicit finite difference formulations have unknown time n+1 values on the r.h.s. of the time-dependent equations in addition to the l.h.s. Usually one must solve a set of simultaneous equations to obtain the updated time n+1 quantities (Reference 7). The advantage of such formulations is to improve the stability of the calculation in a numerical sense, thus allowing for time steps much larger than those derived from the CFL criterion. The disadvantage of such schemes is the additional amount of computations often needed each time cycle to solve the set of simultaneous equations. A practical implicit formulation yields a significant net savings in computational time compared to an explicit formulation, i.e., the decrease in the number of integration cycles realized by increasing the time step outweighs the increase in computations per time step.

Our minimum program objective is the development of a "practical" implicit formulation, i.e., allowing time steps at least 1000 times greater than allowed by an explicit formulation. The scheme should be "conditionally stable," with time steps restricted only by the material particle velocities, u , rather than the stress wave speeds, i.e.,

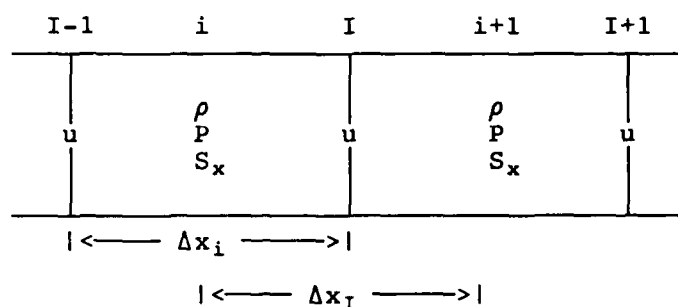
$$\Delta t_u \leq \Delta x / u \quad (13)$$

Thus, in a manner analogous to the CFL wave speed restriction, the allowable time step increases as the particle velocities decrease. For late time ground motions in saturated soils, typical stress wave speeds are at least 1500 m/s, while particle velocities might be on the order of 1-2 cm/s. A comparison of the particle velocity stability requirement (Equation 13) and the CFL condition (Equation 12) shows an increase in allowable time step by a factor of 100,000! This is well above our stated objective of at least 1000.

In general, the choice of time step and grid size for a given calculation is governed by the desired resolution, or accuracy of the solution. For example, in order to resolve the propagation of stress waves for a given grid size, the time step should be chosen to at least satisfy the CFL criterion. Larger time steps will tend to diffuse the wave fronts over time, similar to the diffusion which occurs for coarser grids.

2.3 FINITE DIFFERENCING

The implicit finite-differencing scheme of the time-dependent governing equations (1) to (7) is presented in this section. The following sketch summarizes the primary location of the physical variables in the 1-D x-direction:



The mass (or density) cells are centered at i (lower case), and the momentum cells centered at I (upper case).

The fluid and solid mass conservation Equations (1) and (2) are written:

$$(\rho_f)_i^{n+1} - (\rho_f)_i^n = (k_{f0})_i^n - \theta \frac{\Delta t}{\Delta x_i} \left[(\rho_f u_f)_I^{n+1} - (\rho_f u_f)_{I-1}^{n+1} \right] \quad (14)$$

$$(\rho_s)_i^{n+1} - (\rho_s)_i^n = (k_{s0})_i^n - \theta \frac{\Delta t}{\Delta x_i} \left[(\rho_s u_s)_I^{n+1} - (\rho_s u_s)_{I-1}^{n+1} \right] \quad (15)$$

where

$$(k_{f0})_i^n \equiv - (1 - \theta) \frac{\Delta t}{\Delta x_i} \left[(\rho_f u_f)_I^n - (\rho_f u_f)_{I-1}^n \right] \quad (16)$$

$$(k_{s0})_i^n \equiv - (1 - \theta) \frac{\Delta t}{\Delta x_i} \left[(\rho_s u_s)_I^n - (\rho_s u_s)_{I-1}^n \right] \quad (17)$$

The time centering of Equations (14) and (15) is controlled by the variable θ . A value of $\theta = 0$ implies a purely explicit

finite differencing, while a value of $\theta = 1$ implies purely implicit finite differencing.

The fluid and solid momentum Equations (3) and (4) are written:

$$\begin{aligned} (\rho_f u_f)_I^{n+1} &= (k_{f1})_I^n - \lambda \Delta t D_I^{n+1} \left[(u_f)_I^{n+1} - (u_s)_I^{n+1} \right] \\ &\quad - \phi \frac{\Delta t}{\Delta x_I} \left\{ (\nu_f)_I^n \left[(P_f)_{i+1}^{n+1} - (P_f)_i^{n+1} \right] \right\} \end{aligned} \quad (18)$$

$$\begin{aligned} (\rho_s u_s)_I^{n+1} &= (k_{s1})_I^n + \lambda \Delta t D_I^{n+1} \left[(u_f)_I^{n+1} - (u_s)_I^{n+1} \right] \\ &\quad - \phi \frac{\Delta t}{\Delta x_I} \left\{ (\nu_s)_I^n \left[(P_f)_{i+1}^{n+1} - (P_f)_i^{n+1} \right] \right. \\ &\quad \quad \quad \left. + \left[(P_s)_{i+1}^{n+1} - (P_s)_i^{n+1} \right] \right. \\ &\quad \quad \quad \left. - \left[(S_x)_{i+1}^{n+1} - (S_x)_i^{n+1} \right] \right\} \end{aligned} \quad (19)$$

where

$$\begin{aligned} (k_{f1})_I^n &\equiv (\rho_f u_f)_I^n - \frac{\Delta t}{\Delta x_I} \left[(\rho_f u_f u_f)_{i+1}^n - (\rho_f u_f u_f)_i^n \right] \\ &\quad - (1-\lambda) \Delta t D_I^n \left[(u_f)_I^n - (u_s)_I^n \right] \\ &\quad - (1-\phi) \frac{\Delta t}{\Delta x_I} \left\{ (\nu_f)_I^n \left[(P_f)_{i+1}^n - (P_f)_i^n \right] \right\} \end{aligned} \quad (20)$$

$$(k_{s1})_I^n \equiv (\rho_s u_s)_I^n - \frac{\Delta t}{\Delta x_I} \left[(\rho_s u_s u_s)_{i+1}^n - (\rho_s u_s u_s)_i^n \right]$$

$$\begin{aligned}
& + (1-\lambda)\Delta t D_I^n \left[\left(u_f \right)_I^n - \left(u_s \right)_I^n \right] \\
& - (1-\phi) \frac{\Delta t}{\Delta x_I} \left\{ \left(v_s \right)_I^n \left[\left(P_f \right)_{i+1}^n - \left(P_f \right)_i^n \right] \right. \\
& \quad \left. + \left[\left(P_s \right)_{i+1}^n - \left(P_s \right)_i^n \right] \right. \\
& \quad \left. - \left[\left(S_x \right)_{i+1}^n - \left(S_x \right)_i^n \right] \right\} \quad (21)
\end{aligned}$$

and $\rho_I \equiv \frac{(\Delta x_i \rho_i + \Delta x_{i+1} \rho_{i+1})}{(\Delta x_i + \Delta x_{i+1})}$ is the momentum cell density.

The time centering of Equations (18) and (19) is controlled by the variables λ and ϕ in a manner analogous to θ .

The pore-fluid pressure Equation (5) and effective stress Equations (6) and (7) are written:

$$\begin{aligned}
\left(P_f \right)_i^{n+1} - \left(P_f \right)_i^n & = \left(Ek_{f2} \right)_i^n + \left(\frac{K_f}{\rho_f} \right)_i^n \left[\left(\rho_f \right)_i^{n+1} - \left(\rho_f \right)_i^n \right] \\
& \quad + \left(\frac{K_f}{v_f \rho_{sg}} \right)_i^n \left[\left(\rho_s \right)_i^{n+1} - \left(\rho_s \right)_i^n \right] \quad (22)
\end{aligned}$$

$$\left(P_s \right)_i^{n+1} - \left(P_s \right)_i^n = \left(Ek_{s2} \right)_i^n + \left(\frac{K_s}{\rho_s} \right)_i^n \left[\left(\rho_s \right)_i^{n+1} - \left(\rho_s \right)_i^n \right] \quad (23)$$

$$\begin{aligned}
\left(S_x \right)_i^{n+1} - \left(S_x \right)_i^n & = \left(Ek_{s3} \right)_i^n + \frac{2}{3} \left(\frac{G_s}{\rho_s} \right)_i^n \left[\left(\rho_s \right)_i^{n+1} - \left(\rho_s \right)_i^n \right] \\
& \quad + \alpha 2 \left(G_s \right)_i^n \frac{\Delta t}{\Delta x_i} \left[\left(u_s \right)_I^{n+1} - \left(u_s \right)_{I-1}^{n+1} \right] \quad (24)
\end{aligned}$$

where

$$\left(Ek_{f2} \right)_i^n \equiv - \Delta t \left[u_f \left(\frac{\partial P_f}{\partial x} - \frac{K_f}{\rho_f} \frac{\partial \rho_f}{\partial x} \right) \right]_i^n + \Delta t \left[u_s \left(\frac{K_f}{\nu_f \rho_{sg}} \frac{\partial \rho_s}{\partial x} \right) \right]_i^n \quad (25)$$

$$\left(Ek_{s2} \right)_i^n \equiv - \Delta t \left[u_s \left(\frac{\partial P_s}{\partial x} - \frac{K_s}{\rho_s} \frac{\partial P_s}{\partial x} \right) \right]_i^n \quad (26)$$

$$\begin{aligned} \left(Ek_{s3} \right)_i^n &\equiv - \Delta t \left[u_s \left(\frac{\partial S_x}{\partial x} - \frac{2}{3} \frac{G_s}{\rho_s} \frac{\partial \rho_s}{\partial x} \right) \right]_i^n \\ &+ 2 \left(G_s \right)_i^n (1-\alpha) \frac{\Delta t}{\Delta x_i} \left[\left(u_s \right)_I^n - \left(u_s \right)_{I-1}^n \right] \end{aligned} \quad (27)$$

In order to more readily solve the finite difference equations for the fluid and solid phase momentums at each grid location, the time n+1 drag and solid phase stress deviator terms are approximated as follows:

$$D_I^{n+1} \left[\left(u_f \right)_I^{n+1} - \left(u_s \right)_I^{n+1} \right] \doteq D_I^n \left[\frac{\left(\rho_f u_f \right)_I^{n+1}}{\left(\rho_f \right)_I^n} - \frac{\left(\rho_s u_s \right)_I^{n+1}}{\left(\rho_s \right)_I^n} \right] \quad (28)$$

$$G_s^n \frac{\Delta t}{\Delta x_i} \left[\left(u_s \right)_I^{n+1} - \left(u_s \right)_{I-1}^{n+1} \right] \doteq \frac{\Delta t}{\Delta x_i} \left(\frac{G_s}{\rho_s} \right)_i^n \left[\left(\rho_s u_s \right)_I^{n+1} - \left(\rho_s u_s \right)_{I-1}^{n+1} \right] \quad (29)$$

Substituting Equations (14) and (15) into Equations (22), (23) and (24) eliminates the unknown time n+1 densities. Substituting the resulting equations along with Equations (28) and (29) into the momentum equations (18) and (19) eliminates the time n+1 pressures and stress deviators, yielding the following equations:

$$\left. \begin{aligned} & \left(k_{f5} \right)_I^n \left(\rho_f u_f \right)_I^{n+1} + \left(k_{f6} \right)_I^n \left(\rho_f u_f \right)_{I+1}^{n+1} + \left(k_{f7} \right)_I^n \left(\rho_f u_f \right)_{I-1}^{n+1} \\ & \left(k_{f11} \right)_I^n \left(\rho_s u_s \right)_I^{n+1} + \left(k_{f12} \right)_I^n \left(\rho_s u_s \right)_{I+1}^{n+1} + \left(k_{f13} \right)_I^n \left(\rho_s u_s \right)_{I-1}^{n+1} = \left(k_{f10} \right)_I^n \end{aligned} \right\} (30)$$

$$\left. \begin{aligned} & \left(k_{s5} \right)_I^n \left(\rho_s u_s \right)_I^{n+1} + \left(k_{s6} \right)_I^n \left(\rho_s u_s \right)_{I+1}^{n+1} + \left(k_{s7} \right)_I^n \left(\rho_s u_s \right)_{I-1}^{n+1} \\ & \left(k_{s11} \right)_I^n \left(\rho_f u_f \right)_I^{n+1} + \left(k_{s12} \right)_I^n \left(\rho_f u_f \right)_{I+1}^{n+1} + \left(k_{s13} \right)_I^n \left(\rho_f u_f \right)_{I-1}^{n+1} = \left(k_{s10} \right)_I^n \end{aligned} \right\} (31)$$

where the time n quantities k_{f5} to k_{f13} and k_{s5} to k_{s13} are described in Tables 2.1 and 2.2. $(\rho_f u_f)_I^{n+1}$ and $(\rho_s u_s)_I^{n+1}$ are the two unknowns at each grid point, governed by two equations [(30) and (31)] at each grid point. The two unknowns are implicitly coupled to each other and to the unknown values at adjacent grid points. Solutions to the resulting set of coupled algebraic equations over the entire grid are obtained directly once boundary conditions are specified.

Table 2.1. Definition of coefficients evaluated at time n in fluid momentum equation (30)

$$\left[k_{f5} \right]_I^n \equiv 1 + \lambda \Delta t \left(\frac{D}{\rho_f} \right)_I^n + \frac{\phi \Delta t}{\Delta x_I} \left(\nu_f \right)_I^n \left[\frac{\theta \Delta t}{\Delta x_{i+1}} \left(\frac{K_f}{\rho_f} \right)_{i+1}^n + \frac{\theta \Delta t}{\Delta x_i} \left(\frac{K_f}{\rho_f} \right)_i^n \right]$$

$$\left[k_{f6} \right]_I^n \equiv - \frac{\phi \Delta t}{\Delta x_I} \left(\nu_f \right)_I^n \left[\frac{\theta \Delta t}{\Delta x_{i+1}} \left(\frac{K_f}{\rho_f} \right)_{i+1}^n \right]$$

$$\left[k_{f7} \right]_I^n \equiv - \frac{\phi \Delta t}{\Delta x_I} \left(\nu_f \right)_I^n \left[\frac{\theta \Delta t}{\Delta x_i} \left(\frac{K_f}{\rho_f} \right)_i^n \right]$$

$$\left[k_{f11} \right]_I^n \equiv - \lambda \Delta t \left(\frac{D}{\rho_B} \right)_I^n + \frac{\phi \Delta t}{\Delta x_I} \left(\nu_f \right)_I^n \left[\frac{\theta \Delta t}{\Delta x_{i+1}} \left(\frac{K_f}{\nu_f \rho_{Bg}} \right)_{i+1}^n + \frac{\theta \Delta t}{\Delta x_i} \left(\frac{K_f}{\nu_f \rho_{Bg}} \right)_i^n \right]$$

$$\left[k_{f12} \right]_I^n \equiv - \frac{\phi \Delta t}{\Delta x_I} \left(\nu_f \right)_I^n \left[\frac{\theta \Delta t}{\Delta x_{i+1}} \left(\frac{K_f}{\nu_f \rho_{Bg}} \right)_{i+1}^n \right]$$

$$\left[k_{f13} \right]_I^n \equiv - \frac{\phi \Delta t}{\Delta x_I} \left(\nu_f \right)_I^n \left[\frac{\theta \Delta t}{\Delta x_i} \left(\frac{K_f}{\nu_f \rho_{Bg}} \right)_i^n \right]$$

$$\left[k_{f10} \right]_I^n \equiv \left[k_{f1} \right]_I^n - \frac{\phi \Delta t}{\Delta x_I} \left(\nu_f \right)_I^n \left[\left[Ek_{f2}^* \right]_{i+1}^n - \left[Ek_{f2}^* \right]_i^n \right]$$

where

$$\left[Ek_{f2}^* \right]_i^n \equiv \left[Ek_{f2} \right]_i^n + \left[P_f \right]_i^n + \left(\frac{K_f}{\rho_f} \right)_i^n \left[k_{f0} \right]_i^n + \left(\frac{K_f}{\nu_f \rho_{Bg}} \right)_i^n \left[k_{s0} \right]_i^n$$

Table 2.2. Definition of coefficients evaluated at time n in solid momentum equation (31)

$$\begin{aligned} \left(k_{s5} \right)_I^n &\equiv 1 + \lambda \Delta t \left(\frac{D}{\rho_s} \right)_I^n + \frac{\phi \Delta t}{\Delta x_I} \left(\nu_s \right)_I^n \left[\frac{\theta \Delta t}{\Delta x_{i+1}} \left(\frac{K_f}{\nu_f \rho_{sg}} \right)_{i+1}^n + \frac{\theta \Delta t}{\Delta x_i} \left(\frac{K_f}{\nu_f \rho_{sg}} \right)_i^n \right] \\ &+ \frac{\phi \Delta t}{\Delta x_I} \left[\frac{\theta \Delta t}{\Delta x_{i+1}} \left(\frac{K_s}{\rho_s} \right)_{i+1}^n + \frac{\theta \Delta t}{\Delta x_i} \left(\frac{K_s}{\rho_s} \right)_i^n \right] \\ &+ \frac{\phi \Delta t}{\Delta x_I} \left(2\alpha - \frac{2\theta}{3} \right) \left[\frac{\Delta t}{\Delta x_{i+1}} \left(\frac{G_s}{\rho_s} \right)_{i+1}^n + \frac{\Delta t}{\Delta x_i} \left(\frac{G_s}{\rho_s} \right)_i^n \right] \end{aligned}$$

$$\begin{aligned} \left(k_{s6} \right)_I^n &\equiv - \frac{\phi \Delta t}{\Delta x_I} \left\{ \left(\nu_s \right)_I^n \left[\frac{\theta \Delta t}{\Delta x_{i+1}} \left(\frac{K_f}{\nu_f \rho_{sg}} \right)_{i+1}^n \right] \right. \\ &+ \left. \left[\frac{\theta \Delta t}{\Delta x_{i+1}} \left(\frac{K_s}{\rho_s} \right)_{i+1}^n \right] + \left(2\alpha - \frac{2\theta}{3} \right) \left[\frac{\Delta t}{\Delta x_{i+1}} \left(\frac{G_s}{\rho_s} \right)_{i+1}^n \right] \right\} \end{aligned}$$

$$\begin{aligned} \left(k_{s7} \right)_I^n &\equiv - \frac{\phi \Delta t}{\Delta x_I} \left\{ \left(\nu_s \right)_I^n \left[\frac{\theta \Delta t}{\Delta x_i} \left(\frac{K_f}{\nu_f \rho_{sg}} \right)_i^n \right] \right. \\ &+ \left. \left[\frac{\theta \Delta t}{\Delta x_i} \left(\frac{K_s}{\rho_s} \right)_i^n \right] + \left(2\alpha - \frac{2\theta}{3} \right) \left[\frac{\Delta t}{\Delta x_i} \left(\frac{G_s}{\rho_s} \right)_i^n \right] \right\} \end{aligned}$$

$$\left(k_{s11} \right)_I^n \equiv - \lambda \Delta t \left(\frac{D}{\rho_f} \right)_I^n + \frac{\phi \Delta t}{\Delta x_I} \left(\nu_s \right)_I^n \left[\frac{\theta \Delta t}{\Delta x_{i+1}} \left(\frac{K_f}{\rho_f} \right)_{i+1}^n + \frac{\theta \Delta t}{\Delta x_i} \left(\frac{K_f}{\rho_f} \right)_i^n \right]$$

$$\left(k_{s12} \right)_I^n \equiv - \frac{\phi \Delta t}{\Delta x_I} \left(\nu_s \right)_I^n \left[\frac{\theta \Delta t}{\Delta x_{i+1}} \left(\frac{K_f}{\rho_f} \right)_{i+1}^n \right]$$

$$\left(k_{s13} \right)_I^n \equiv - \frac{\phi \Delta t}{\Delta x_I} \left(\nu_s \right)_I^n \left[\frac{\theta \Delta t}{\Delta x_i} \left(\frac{K_f}{\rho_f} \right)_i^n \right]$$

Table 2.2 (continued)

$$\begin{aligned} \left(k_{s10} \right)_I^n &\equiv \left(k_{s1} \right)_I^n - \frac{\phi \Delta t}{\Delta x_I} \left\{ \left(\nu_s \right)_I^n \left[\left(Ek_{f2}^* \right)_{i+1}^n - \left(Ek_{f2}^* \right)_i^n \right] \right. \\ &\quad + \left[\left(Ek_{s2}^* \right)_{i+1}^n - \left(Ek_{s2}^* \right)_i^n \right] \\ &\quad \left. - \left[\left(Ek_{s3}^* \right)_{i+1}^n - \left(Ek_{s3}^* \right)_i^n \right] \right\} \end{aligned}$$

where

$$\left(Ek_{f2}^* \right)_i^n \equiv \left(Ek_{f2} \right)_i^n + \left(P_f \right)_i^n + \left(\frac{K_f}{\rho_f} \right)_i^n \left(k_{f0} \right)_i^n + \left(\frac{K_f}{\nu_f \rho_{sg}} \right)_i^n \left(k_{s0} \right)_i^n$$

$$\left(Ek_{s2}^* \right)_i^n \equiv \left(Ek_{s2} \right)_i^n + \left(P_s \right)_i^n + \left(\frac{K_s}{\rho_s} \right)_i^n \left(k_{s0} \right)_i^n$$

$$\left(Ek_{s3}^* \right)_i^n \equiv \left(Ek_{s3} \right)_i^n + \left(S_x \right)_i^n - \frac{2}{3} \left(\frac{G_s}{\rho_s} \right)_i^n \left(k_{s0} \right)_i^n$$

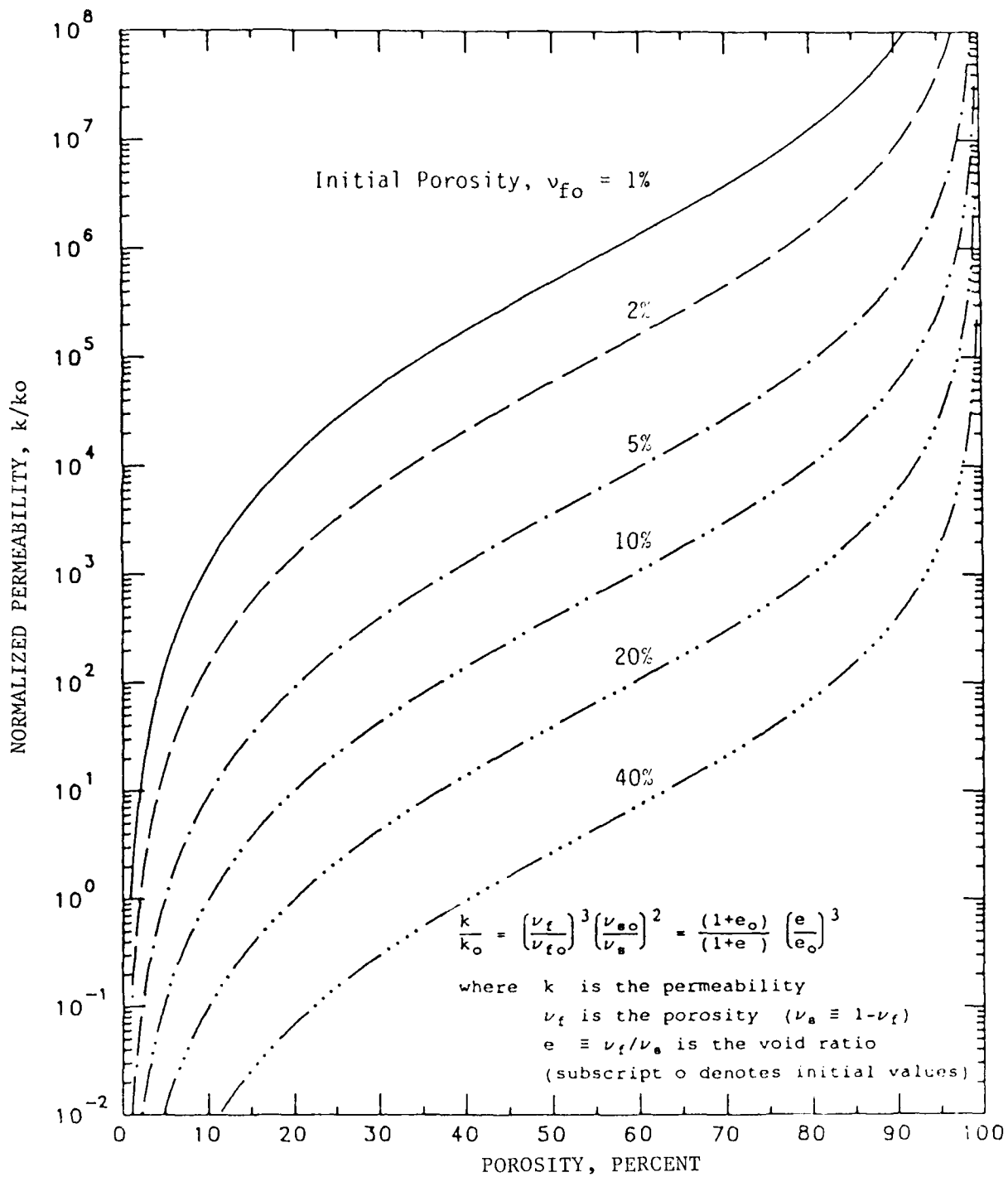


Figure 2.1. Normalized permeability, k/k_0 , versus porosity for various initial porosities.

CHAPTER 3

NUMERICAL RESULTS

Several different 1-D (planar geometry) calculations were performed to demonstrate the ability of CRIME to implicitly treat various aspects of the multiphase physics. The results of these test cases are presented in four subsections emphasizing the following:

- a) Effective stress deviators for solid phase constitutive models (velocity and/or strain dependent, e.g., cap-type),
- b) Relative flow and late-time stress redistribution (consolidation) in a fluid-filled porous soil,
- c) Comparison with an independent calculation, and
- d) Layered geology including dry, partially and fully saturated soils.

3.1. EFFECTIVE STRESS DEVIATORS

Table 3.1 summarizes the 1-D calculations which demonstrate the ability of CRIME to implicitly treat effective stress deviators. A constant loading pressure of 50 bars is applied to one end of a porous soil lattice 50 m long, which is divided into 50 uniform cells ($\Delta x = 1$ m). A rigid (no-flow) boundary condition is imposed at the other end.

The cap-type constitutive model given in Reference 1 is used to describe the effective stress behavior of the solid soil lattice. Figure 3.1 shows the uniaxial strain (UX) load-unload stress-strain behavior for vertical strains* up to 12% and Figure 3.2 shows the corresponding effective UX stress path and the effective triaxial shear (TX) failure surface. The initial

* Strains are engineering, i.e., $\epsilon_{v01} \equiv (v_0 - v)/v_0 \equiv (\rho - \rho_0)/\rho$

loading bulk modulus, $K_s = 1.0$ kbar, and shear modulus, $G_s = 0.75$ kbar, yield a seismic velocity of 340 m/s for an initial soil density $\rho_{so} = 1.75$ gm/cc. The (explicit) CFL condition would require that the time step be less than $\Delta t_{CFL} = 2.9$ msec. The signal from the initial loading will reach the rigid boundary by 0.15 sec.

Four calculations were performed, with time steps varying from 0.5 msec (0.17 times Δt_{CFL}) to 0.5 sec (170 times Δt_{CFL}). The implicit capability of CRIME is exercised by setting the numerical parameters controlling the time centering of the finite difference equations $\theta = \phi = \lambda = 1$ for all four cases. The results are presented in the form of stress and velocity profiles at various times.

Figure 3.3 shows the total effective axial stress* and velocity profiles for Case E220, which used a time step $\Delta t = 0.5$ msec. A constant 50 bar stress wave is seen to propagate at ~ 340 m/s, with an associated particle velocity of 8.4 m/s. The shock front is spread over ~ 5 zones, the midpoint of which is at 33 m by 50 msec. Figure 3.4 shows that the effective pressure and axial stress deviator components are 31 bar and 19 bar, respectively.

Figures 3.5 and 3.6 show the stress and velocity profiles for Case E223, which used a time step of $\Delta t = 5$ msec. This is a ten-fold increase over the previous case, and is 1.7 times Δt_{CFL} . Although the calculation needs only ten time steps to reach 50 msec, the time step is too small to resolve a sharp shock front; the larger time step results in an increased smearing of the shock front. Note, however, that the general characteristics of the solution are maintained, as the midpoint of the shock front has reached ~ 33 m at 50 msec.

* Stresses/pressures are plotted positive for compression

Figures 3.7 and 3.8 show the stress and velocity profiles for Case E224, which used a time step of $\Delta t = 50$ msec. This is an additional ten-fold increase over the previous case, and is 17 times Δt_{CFL} . In this case, the initial stress wave will propagate through 17 zones in one time step. After five time steps (0.250 sec), the wave will have already reflected off the left boundary and propagated 2/3 of the way back to the source. Although the larger time step has resulted in a further smearing of the shock front, the general characteristics of the solution are still maintained for each of the five integration cycles, and the solution has remained stable in a numerical sense.

An additional calculation was performed with five time steps of $\Delta t = 0.5$ sec (Case E225, Figures 3.9 and 3.10). By $t = 1.5$ sec, the calculation is essentially complete, as the entire soil lattice has reached zero velocity and 50 bars of stress.

3.2. RELATIVE FLOW AND LATE TIME STRESS REDISTRIBUTION

Table 3.2 summarizes the 1-D calculations which demonstrate the ability of CRIME to implicitly treat relative flow and late-time stress redistribution (consolidation) in a saturated porous soil. A 50-m-long water-filled soil lattice is divided into 50 uniform cells ($\Delta x = 1$ m), with rigid boundaries at each end. From $x = 0$ to 25 m the initial water pressure is 1 bar and the effective stress is 2 bars; from 25 m to 50 m the water pressure is 2 bars and the effective stress is 1 bar. Thus the initial total stress load of the system is 3 bars everywhere.

A simple linear-elastic equation of state is used to describe the effective stress behavior of the soil lattice, with bulk modulus $K_s = 5$ kbar and shear modulus $G_s = 3.75$ kbar. A simple hydro-elastic equation of state is used to describe the water pressure behavior, with bulk modulus $K_w = 20$ kbar.

The rate at which the individual stress imbalances reach equilibrium (consolidation) is determined by the soil permeability. Two calculations were performed to examine this effect: Case E129 assumed an initial permeability of 100 cm/s, while Case E130 used 0.01 cm/s. Each calculation started with a time step $\Delta t = 0.1$ msec, and increased by a factor of 10 each subsequent integration cycle. (Note that $\Delta t_{CFL} = 0.5$ msec for this material.) The numerical parameters controlling the time centering of the finite difference equations were set to $\theta = \phi = \lambda = 1$ for each case. The results are presented in the form of stress and velocity profiles at various times.

Figure 3.11 shows the fluid pressure profiles at each time (top figure) and the effective vertical stress profiles (lower figure) for Case E129 ($k = 100$ cm/s); Figure 3.12 shows the associated fluid and solid phase velocity profiles. During the consolidation process, peak velocities of -7.4 cm/s for the water and $+2.2$ cm/s for the solid phase occur after three integration cycles ($t = 11.1$ msec). These peak values occur at the point marking the position of the original stress discontinuities ($x = 25$ m), and thus, the largest differential stress gradients. After five integration cycles ($t = 1.11$ sec), the calculation is essentially complete, as both the fluid pressure and effective stress have been uniformly redistributed to a value of 1.5 bar, and the particle velocities are zero.

When the permeability is reduced by a factor of 1000, the consolidation process takes longer, as demonstrated by Case E130 ($k = 0.01$ cm/s). Figures 3.13 and 3.14 are similar to Figures 3.11 and 3.12 for Case E129, showing the first five integration cycles to $t = 1.11$ sec. Peak particle velocities are nearly 30 times smaller and the consolidation process has only propagated to ~ 10 m on either side of $x = 25$ m. Figures 3.15 and 3.16 show the final three integration cycles to $t = 1111$ sec, at which time

the calculation is considered complete. Note that the time for completion of the consolidation process has increased by a factor of ~1000, consistent with the decrease in soil permeability.

3.3. COMPARISON CALCULATION

As a partial validation of the CRIME code a calculation was performed which can be compared directly to that performed by Prevost (Reference 8). Table 3.3 summarizes the initial and boundary conditions of the problem, which is essentially one of 1-D wave propagation in a fluid-saturated porous medium.

The calculation is initiated with a constant 10 bar loading pressure applied at the surface. 10 m of dry soil (the pores are void) overly a fluid-saturated soil lattice. The top 70 m are divided into 70 uniform cells ($\Delta y = 1$ m); subsequent cells increase by 10% downward to over 1100 m depth. The rigid bottom boundary is chosen far enough away as to not influence the calculation over the integration time frame (1.7 sec). At the 10 m water table depth a partially reflected stress wave will propagate back to the surface, where computational "absorbing dampers" will allow it to pass without further reflections.

The permeability of the the soil lattice is assumed to be $k = 50$ cm/s, which corresponds to a drag coefficient $D = 5$ g/cc/s. The effective stress behavior is described by a simple linear-elastic equation of state, with bulk modulus $K_s = 33.3$ bar and shear modulus $G_s = 50$ bar. The pore-fluid pressure is described by a simple hydro-elastic EOS, with bulk modulus $K_f = 5$ kbar, and is much stiffer than the soil lattice.

Both CRIME Case E444 and the calculation of Prevost used a constant time step $\Delta t = 8.5$ msec. Pore-fluid pressures and effective stresses are compared in Figures 3.17 and 3.18 which show time histories at various depths in the saturated region.

Figures 3.19 and 3.20 show comparisons of the fluid and solid phase particle velocities. The results are quite similar.* The more diffusive nature of Case E444 is due to implementing the fully implicit finite differencing of CRIME by setting the numerical parameters $\theta = \phi = \lambda = 1$. Prevost implemented a "split operator method", whereby the solid phase equations were treated explicitly, while the fluid was treated implicitly. The exact duplication of Prevost's results was not the focus of this study, and thus this comparison is felt to be adequate.

3.4. LAYERED GEOLOGY WITH VARYING SATURATION

A primary objective in the development of the CRIME code was the capability of treating realistic geologies. Table 3.4 summarizes a 1-D calculation of the loading and subsequent consolidation of a layered geology with varying saturation.

The site profile is an idealized representation of the top three layers of the MISERS BLUFF II-1 site (Reference 1). The initial porosity for each layer is assumed to be 27.4%: Material A consists of dry sand with air-filled porosity (0 to 5 m depth), Material B is partially saturated (S=90% water-filled porosity, 5 to 13 m depth), and Material C is fully saturated (13 to 34 m depth). The permeability is assumed to be $k = 0.01$ cm/s.

The effective stress behavior described by the cap-type model of Baladi and Barnes (Reference 1) is assumed the same for each material. Their total stress behavior differs according to the degree of saturation, as demonstrated in Figure 3.21 which shows the UX stress-strain response of Materials A, B and C in terms of total stress. Note that the difference between the

* Note that the sign convention of Prevost is followed, such that compressive stresses are negative, compressive pressures are positive, and positive velocities are downward.

Material C and Material A stresses represents the pore-water pressure contribution in Material C.

The computational domain consisted of 1-m cells in each layer. A constant 50 bar loading pressure is applied to the surface, and the bottom boundary is assumed rigid. The initial pore pressures in each material is one atmosphere (1.0132 bar). Material C has the largest seismic velocity (1900 m/s), and as such, the (explicit) CFL condition would require that the time step be less than $\Delta t_{CFL} = 0.5$ msec.

Two calculations were performed. Case E605 used a constant time step of $\Delta t = \Delta t_{CFL} = 0.5$ msec to a maximum simulation time of 0.5 sec. Case E607 initially used a time step of $\Delta t = 5.0$ msec to a simulation time of 0.6 sec. Subsequent integration runs used larger time steps, with an eventual maximum of $\Delta t = 100$ sec from 750 to 1250 sec. The results from Case E605 are presented below, followed by Case E607.

Figure 3.22 shows the total vertical stress, and Figure 3.23 shows the corresponding pore-fluid pressure and effective vertical stress at times of 10, 20, 30, 40 and 50 msec for Case E605 ($\Delta t = 0.5$ msec). The stress wave generated by the 50 bar overpressure loading propagates downward, arriving at the Material A/B interface (5-m depth) after 10 msec. The total stress behavior between these two materials is very similar at these relatively low stress levels (Figure 3.21) such that there is very little reflection occurring at this interface. However, the partitioning of the total stress loading is different. Whereas virtually all of the 50-bar load is taken by the soil lattice in Material A, the water-air mixture in the pores of Material B accounts for ~4 bars of the total stress.

The Material B/C interface is reached after 30 msec. The differing total stress behavior (impedance) of these materials

causes a partially reflected stress of ~ 125 bar, which propagates in both directions. Most of the total stress transmitted down through Material C is now taken by the pore-water in the saturated soil. By 50 msec the bottom boundary has been reached, generating even larger reflected stresses.

Figure 3.24 shows the corresponding velocities of the soil lattice and relative velocity of the pore-fluid with respect to the soil lattice. During the loading phase, downward velocities reach ~ 8 m/s in Materials A and B, and ~ 3 m/s in Material C. Peak upward relative velocities of ~ 17 cm/s occur at the Material B/C interface. It is at this interface that the largest differential pore pressure/effective stress gradient occurs after the passage of the loading stress wave.

Figures 3.25 to 3.29 show the multiphase stress and velocity time histories (to $t = 0.5$ sec) at various depths for Case E605. The propagation of the initial stress loading signal and subsequent reflections and transmissions at the interfaces and boundaries are evident in the total vertical stress time histories (Figure 3.25). The maximum reflected stress at the bottom boundary of nearly 250 bars occurs at ~ 60 msec. The constant overpressure loading of 50 bars at the surface acts to damp out the incoming reflected stress waves, and the entire column oscillates around the 51-bar stress level, which will be the final stress state.

The effective stress and pore pressure behavior are shown in Figures 3.26 and 3.27. As expected, these time histories oscillate in phase with the total stress. The underlying distribution of the total stress load to the effective stress and pore pressure in each material is essentially unchanged during the initial 0.5 sec, as the effective stress carries most of the load in Material A and the pore-water does so in Material C.

The solid particle velocity and relative fluid velocity are shown in Figures 3.28 and 3.29. These time histories also oscillate in phase with the total stress. However, note that with respect to the (oscillating) soil lattice there are upward pore-fluid velocities, with maximum values of ~ 17 cm/s occurring at the original Material B/C interface at the 13-m depth. These relative velocities are indicative of the long-term consolidation process which will occur as the pore pressures in Materials B and C dissipate towards pressure equilibrium.

Case E607 demonstrates the ability of the CRIME code to calculate the late-time consolidation process. A constant time step of $\Delta t = 5$ msec (10 times Δt_{CFL}) is used for the first 0.6 sec of the calculation, the results of which can be compared directly to Case E605. Figures 3.30, 3.31, and 3.32 show the multiphase stress and velocity profiles at 10, 20, 30, 40 and 50 msec. Although there is a loss of temporal resolution, the general characteristics of the solution are maintained. In particular, the differential stress loading in each material and the relative fluid velocity at the Material B/C interface are reproduced.

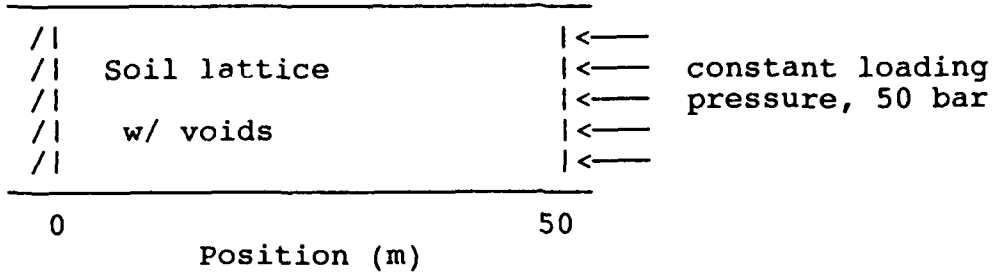
Figures 3.33 to 3.37 show the multiphase stress and velocity time histories to $t = 0.5$ sec. When comparing the total vertical stress to Case E605 it is evident that the larger time step of Case E607 has served to filter or damp out the oscillations associated with the propagation back and forth of the reflected stress wave. By $t = 0.5$ sec the solution is relatively quiescent, achieving stress and velocity values consistent with the mean values of Case E605.

Subsequent time integrations of Case E607 used even larger time steps (see Table 3.4), enabling the calculation to efficiently proceed to $t = 1250$ sec. The total CPU time used is

one third the amount used for Case E605, while simulating to 2500 times farther in time.

Figures 3.38 to 3.41 show the multiphase stress and velocity time histories to $t = 1250$ sec, during which time consolidation occurs. As the large pore pressures in Materials B and C dissipate slowly due to the relative upward flow of water, the soil lattice consolidates and the effective stresses increase to the 50-bar loading stress. Figures 3.42 summarize this process in the form of pore pressure and effective stress profiles at late times. Figure 3.43 shows the displacements of selected fluid and solid tracers during the calculation. There is a net upward displacement of the pore-fluid and a net downward displacement of the soil lattice as it compresses to carry the 50-bar loading stress.

Table 3.1. Summary of 1-D calculations emphasizing solid phase stress deviators



zoning $\Delta x = 1 \text{ m}$
 initial soil density $\rho_s = 1.75 \text{ g/cc}$
 soil porosity $\nu_f = 27.4 \%$
 seismic velocity $c = 340 \text{ m/s}$
 maximum explicit time step $\Delta t_{CFL} = 2.9 \text{ msec}$

Case	Time step (sec)	Simulation time (sec)	Integration cycles
E220	0.0005	0.05	100
E223	0.005	0.05	10
E224	0.05	0.25	5
E225	0.5	2.5	5

Table 3.2. Summary of 1-D calculations emphasizing relative flow and stress redistribution

Water-filled soil lattice

/		/
/	water pressure = 1 bar	water pressure = 2 bar
/		
/	solid stress = 2 bar	solid stress = 1 bar
/		
0	25	50
Position (m)		

zoning	$\Delta x = 1 \text{ m}$
elastic soil	$K_s = 5.0 \text{ kbar}$
	$G_s = 3.75 \text{ kbar}$
initial soil density	$\rho_s = 1.75 \text{ g/cc}$
soil porosity	$\nu_f = 27.4 \%$
multiphase wave speed	$c = 2027 \text{ m/s}$
maximum explicit time step	$\Delta t_{CFL} = 0.5 \text{ msec}$

Case	E129	E130
permeability, k	100 cm/s	.01 cm/s
Maximum time step in calculation*	1 sec	1000 sec
Simulation time	1.11 sec	1111 sec
Number of integration cycles	5	8

* The initial time step $\Delta t_0 = 0.1 \text{ msec}$.
For each integration cycle Δt increased by a factor of 10.

Table 3.4. Summary of 1-D calculations emphasizing layered geology with varying saturation

/					<—	
/	Material C		Material B		Material A	<— constant
/						<— loading
/	Saturated		Partially-			<— over-
/	soil		saturated		Dry soil	<— pressure,
/	S=100%		soil S=90%		S = 0%	<— 50 bar
/						<—
34		13		5		0
		Depth (m)				

Initial Material Properties

Material	wet density (g/cc)	dry density (g/cc)	water content S (%)	Air void content V_a (%)	Seismic velocity c (m/s)	permeability k (cm/s)
A	1.75	1.75	0	27.4	340	.01
B	2.00	1.75	90	2.74	340	.01
C	2.02	1.75	100	0	1900	.01

- o Geologic profile represents idealized MISERS BLUFF II-1 site
- o Initial porosity is assumed to be $\nu_f = 27.4\%$ for each layer
- o Effective stress behavior for each layer is described by the cap-type model of Baladi and Barnes (Reference 1)

Table 3.4 (continued)

Calculational Parameters

zoning (Δy)	1 m
multiphase wave speed (c)	1.9 km/s
Maximum explicit time step (CFL condition, $\Delta t_{CFL} < \Delta y/c$)	0.5 msec

Case	Time step (sec)	Integration cycle	Simulation time (sec)	Cumulative CPU time* (min)
E605	0.0005	0 - 1000	0. - 0.5	25.0
E607	0.005	0 - 120	0. - 0.6	3.5
	0.5	120 - 220	0.6 - 50.6	6.0
	5.	220 - 260	50.6 - 250.6	7.0
	50.	260 - 270	250.6 - 750.6	7.5
	100.	270 - 275	750.6 - 1250.6	7.8

* Computer used is ELXSI 6400

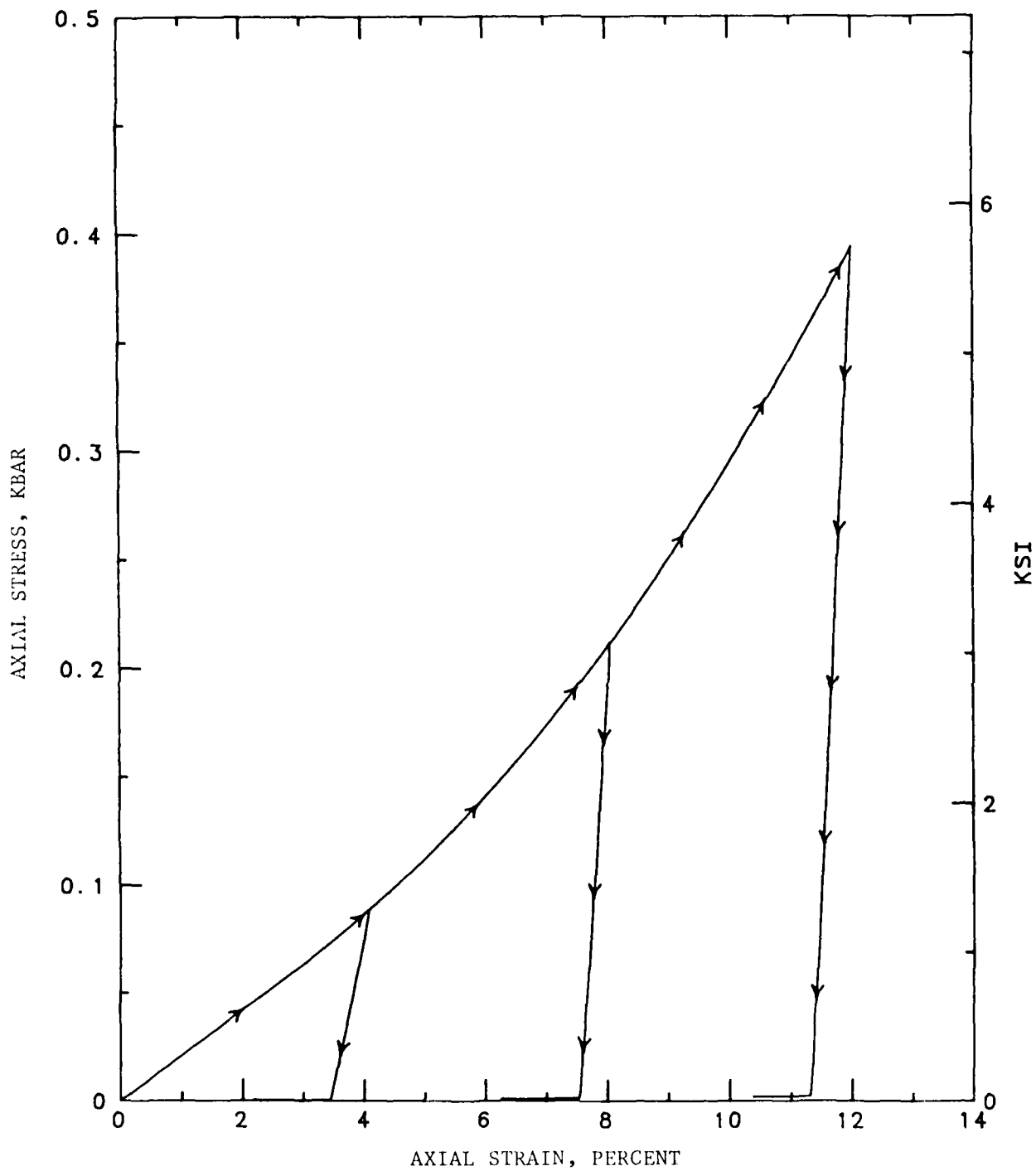


Figure 3.1. Cap model fit for MISERS BLUFF II-1 site Material A: UX compressibility relation to $\sigma_z = 0.4$ kbar.

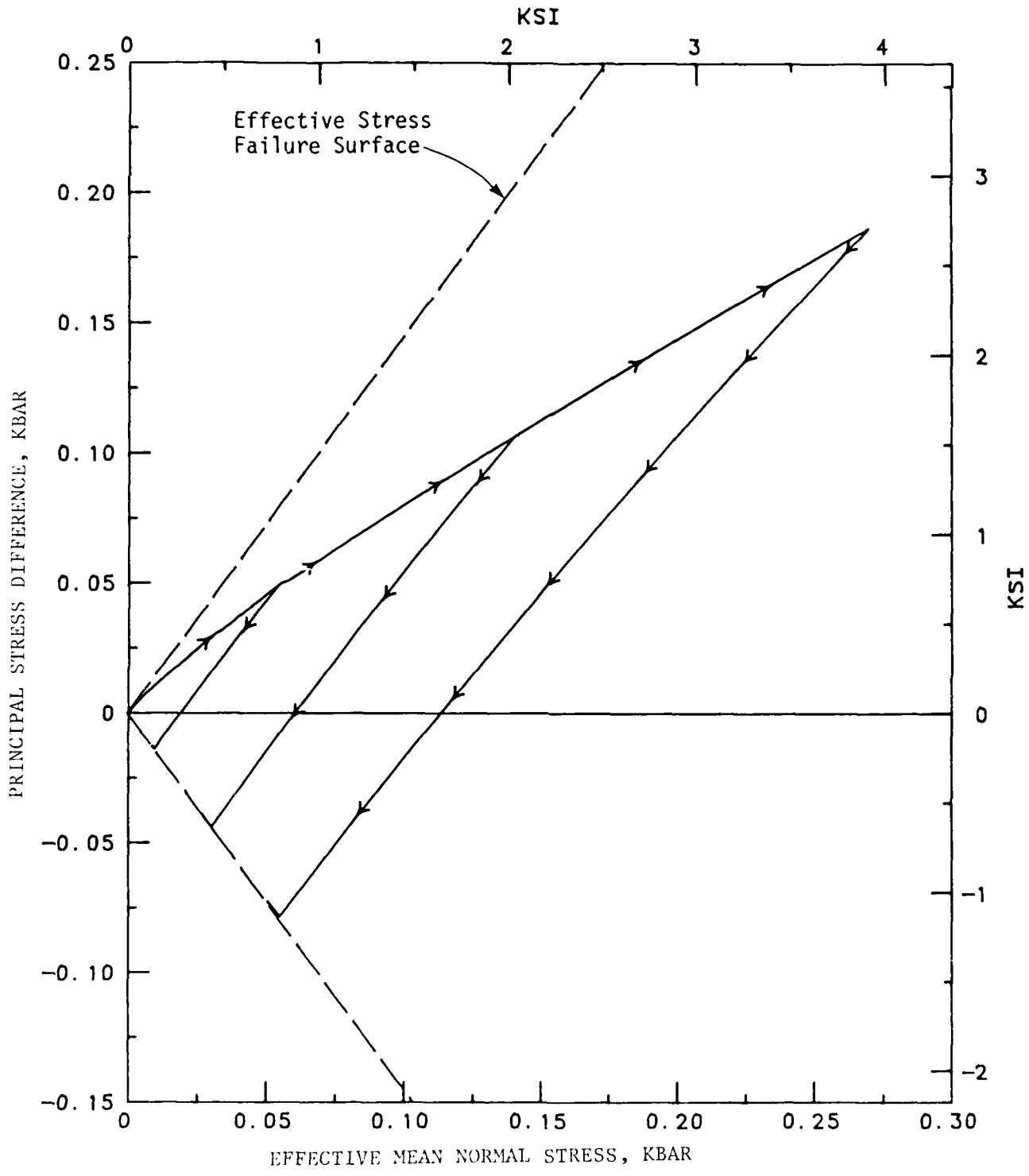


Figure 3.2. Cap model fit for MISERS BLUFF 11-1 site Material A: UX stress path to $\sigma_z = 0.4$ kbar and TX failure envelope.

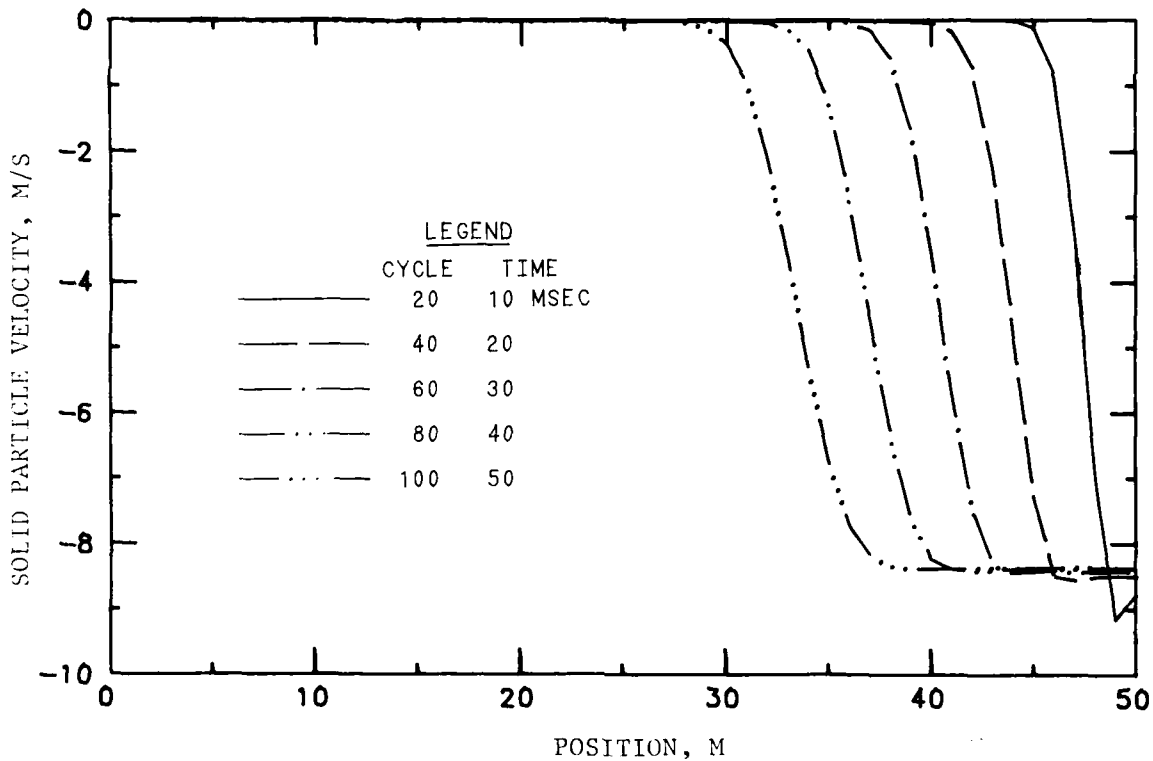
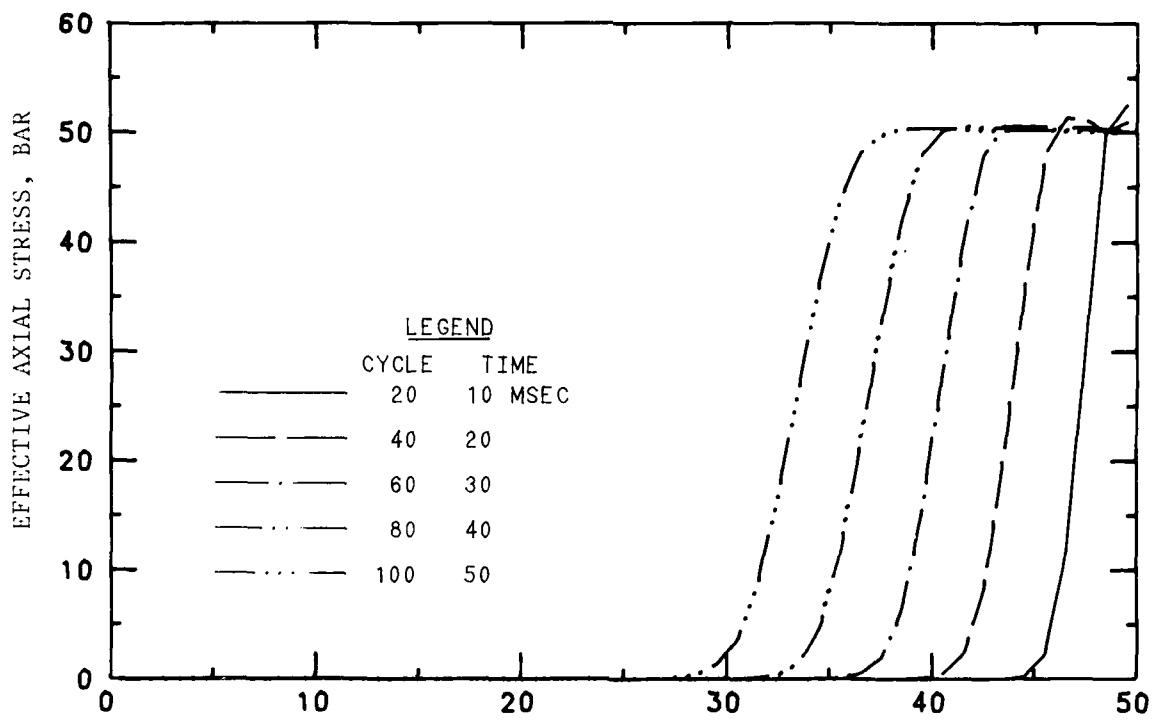


Figure 3.3. Effective axial stress and particle velocity versus position at various times for Case E220.

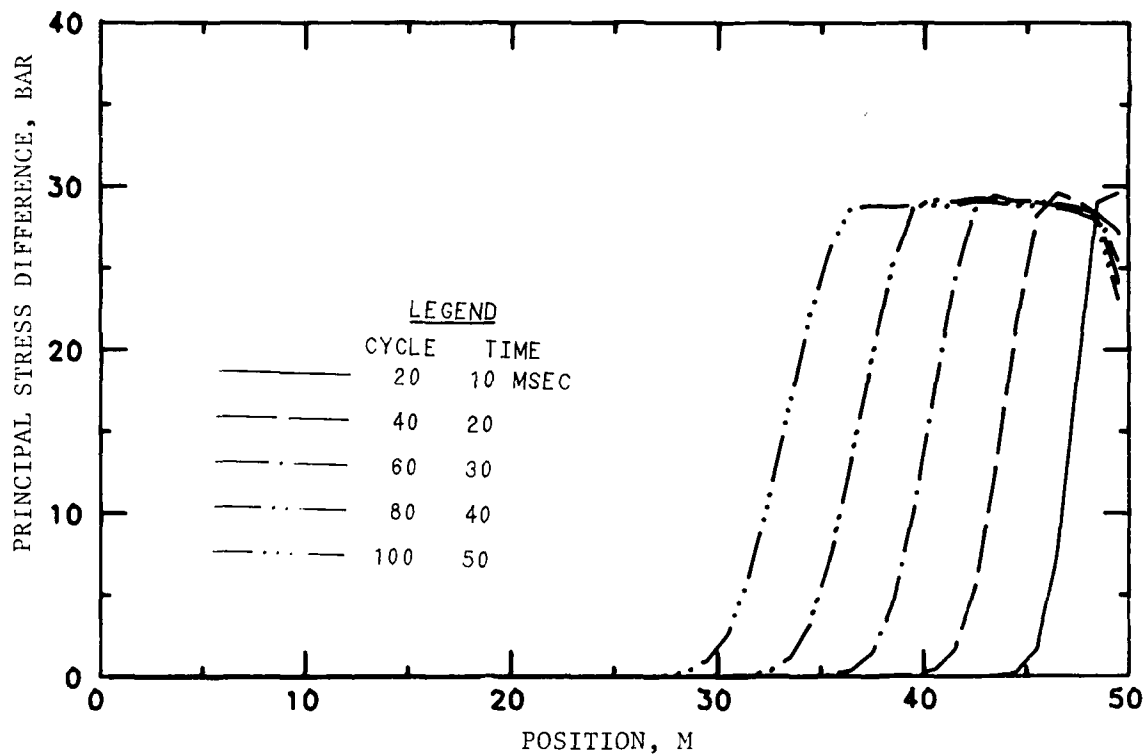
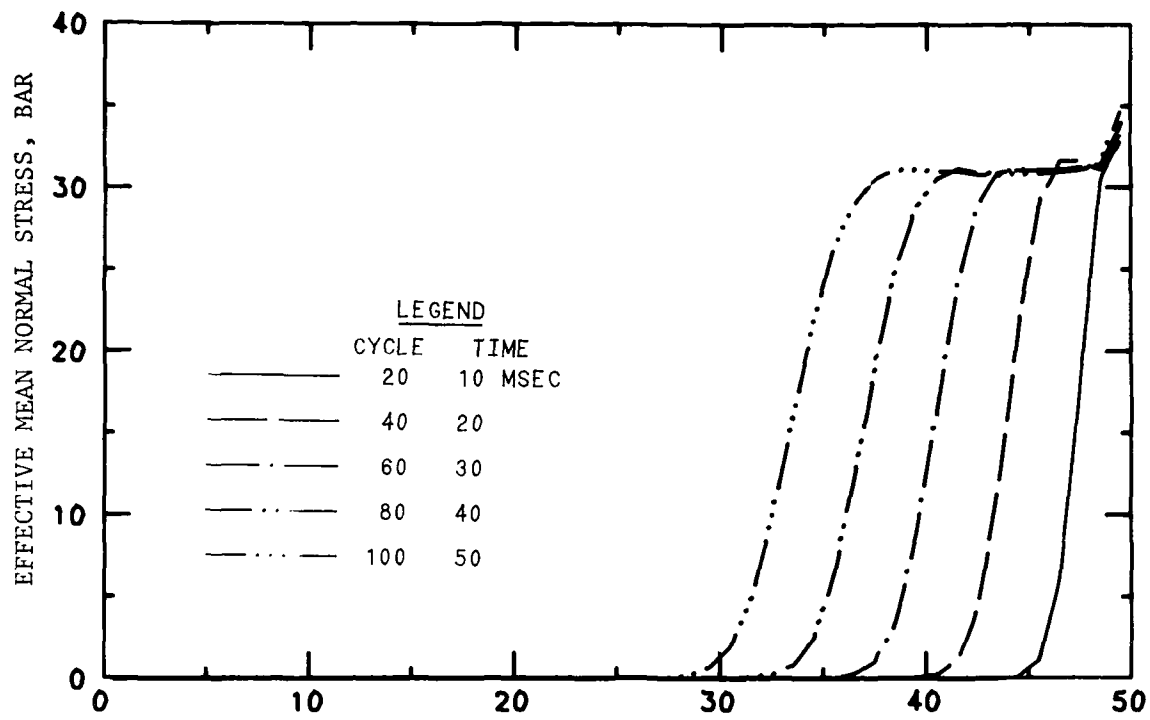


Figure 3.4. Effective mean normal stress and principal stress difference versus position at various times for Case E220.

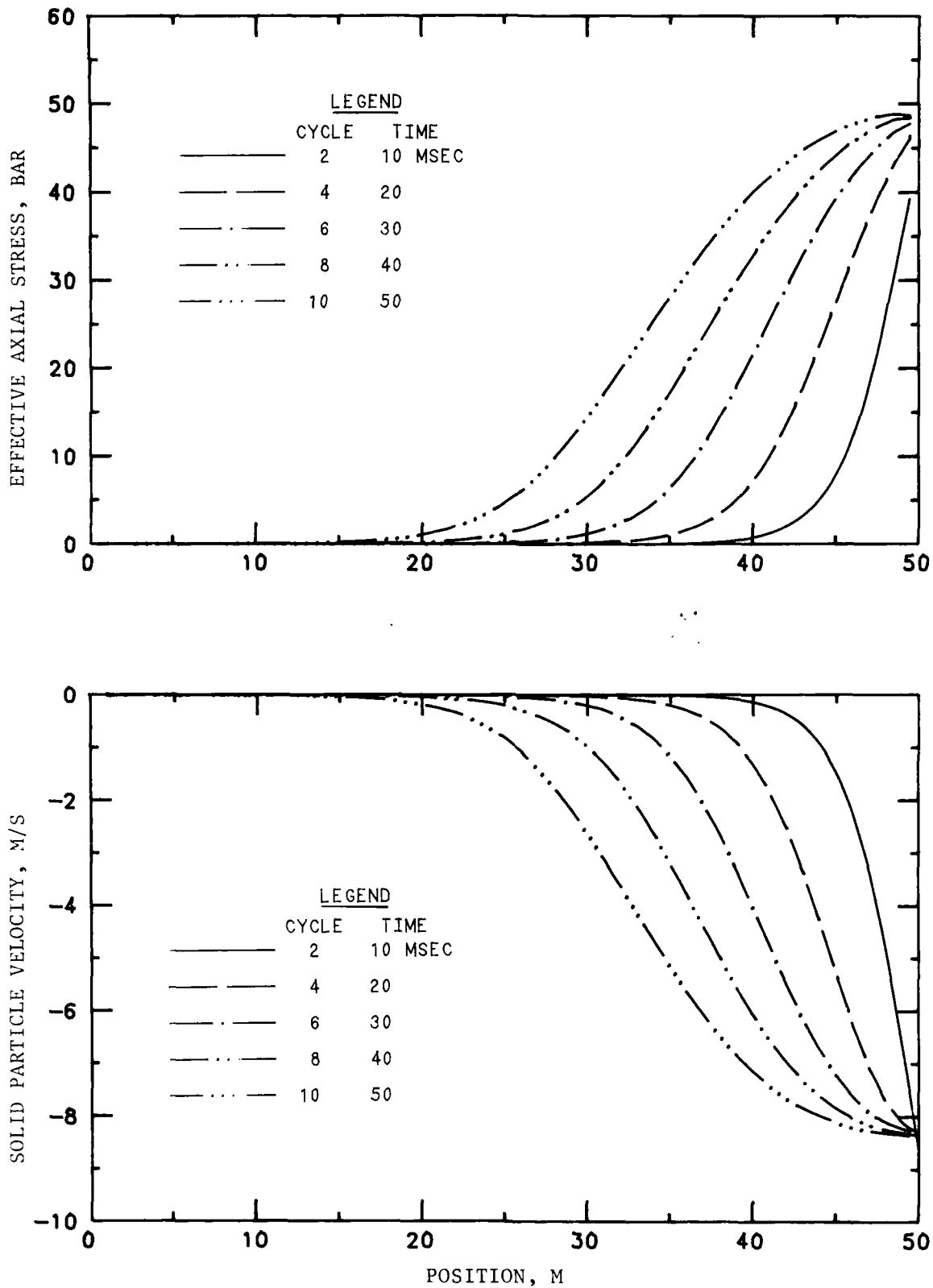


Figure 3.5. Effective axial stress and particle velocity versus position at various times for Case E223.

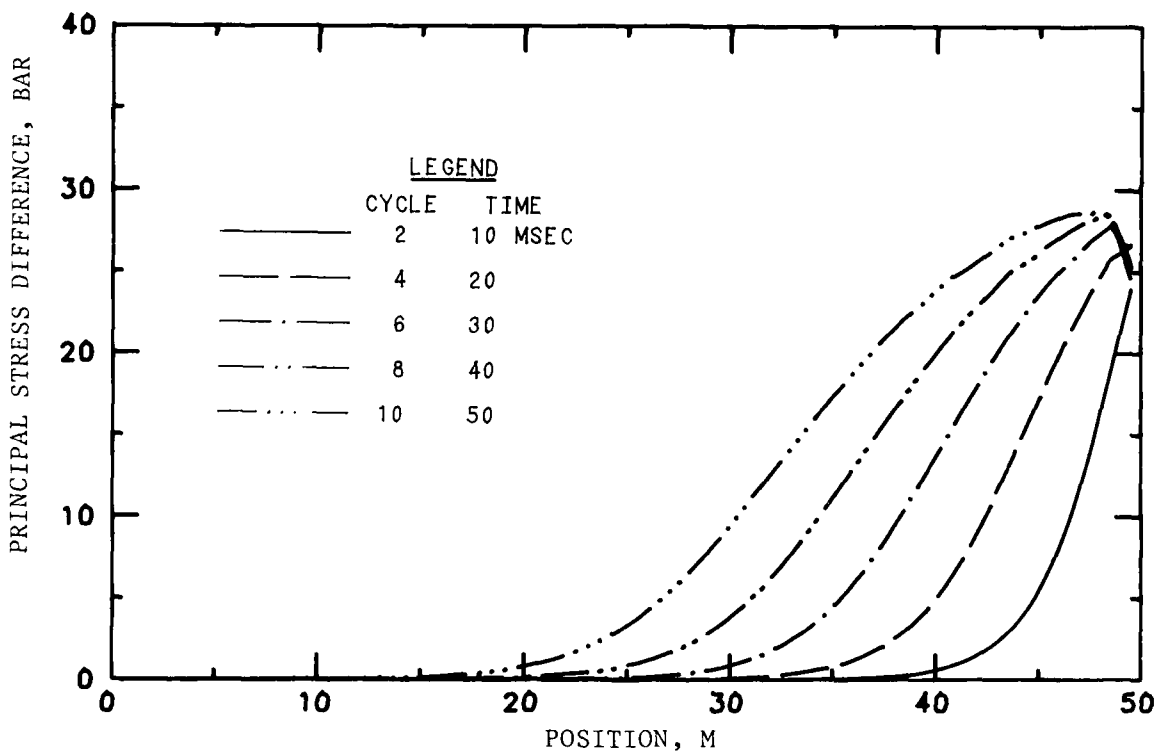
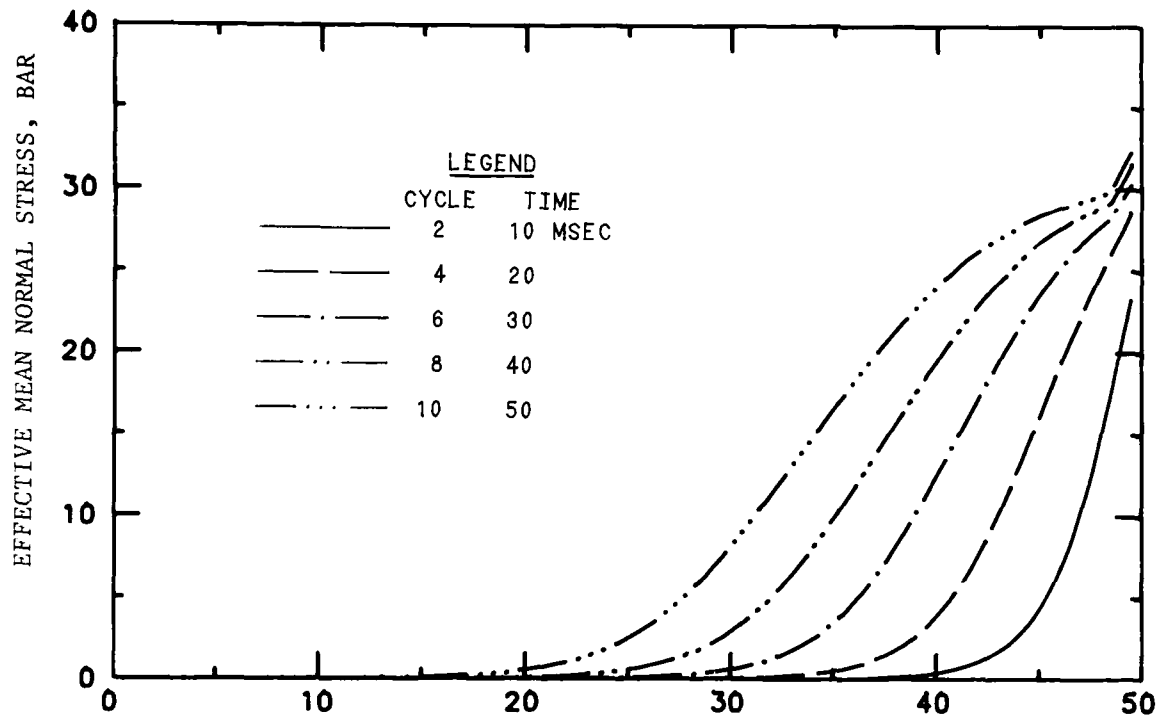


Figure 3.6. Effective mean normal stress and principal stress difference versus position at various times for Case E223.

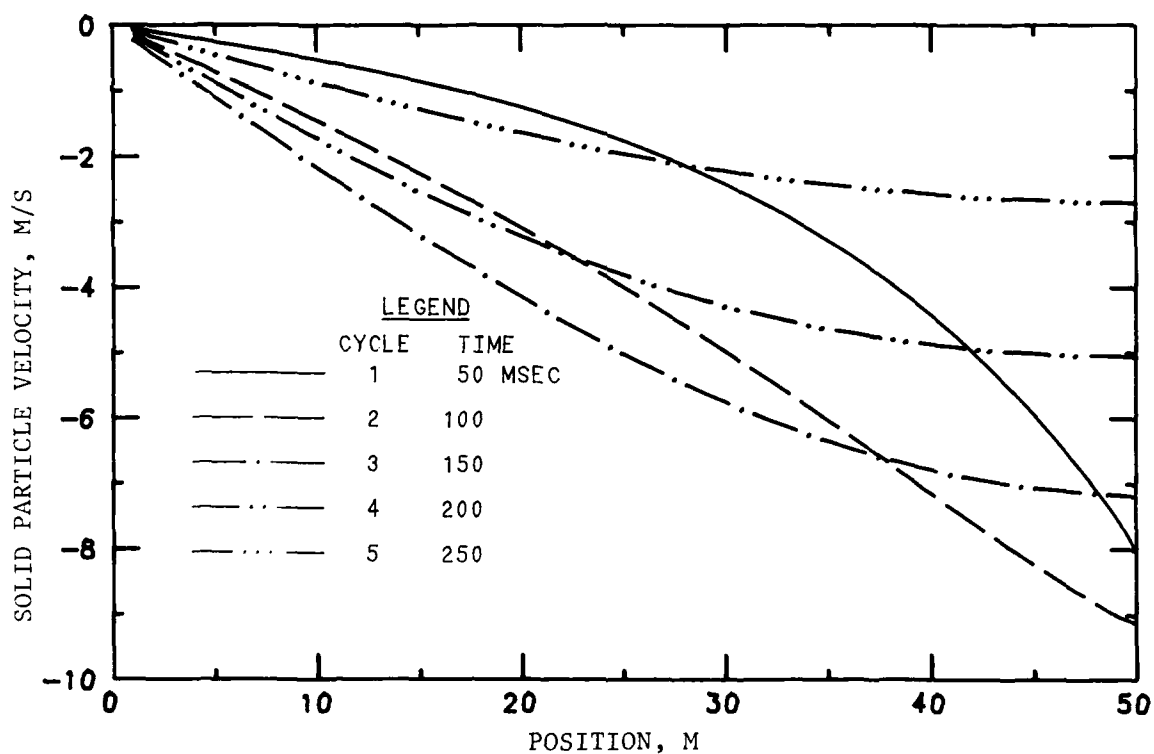
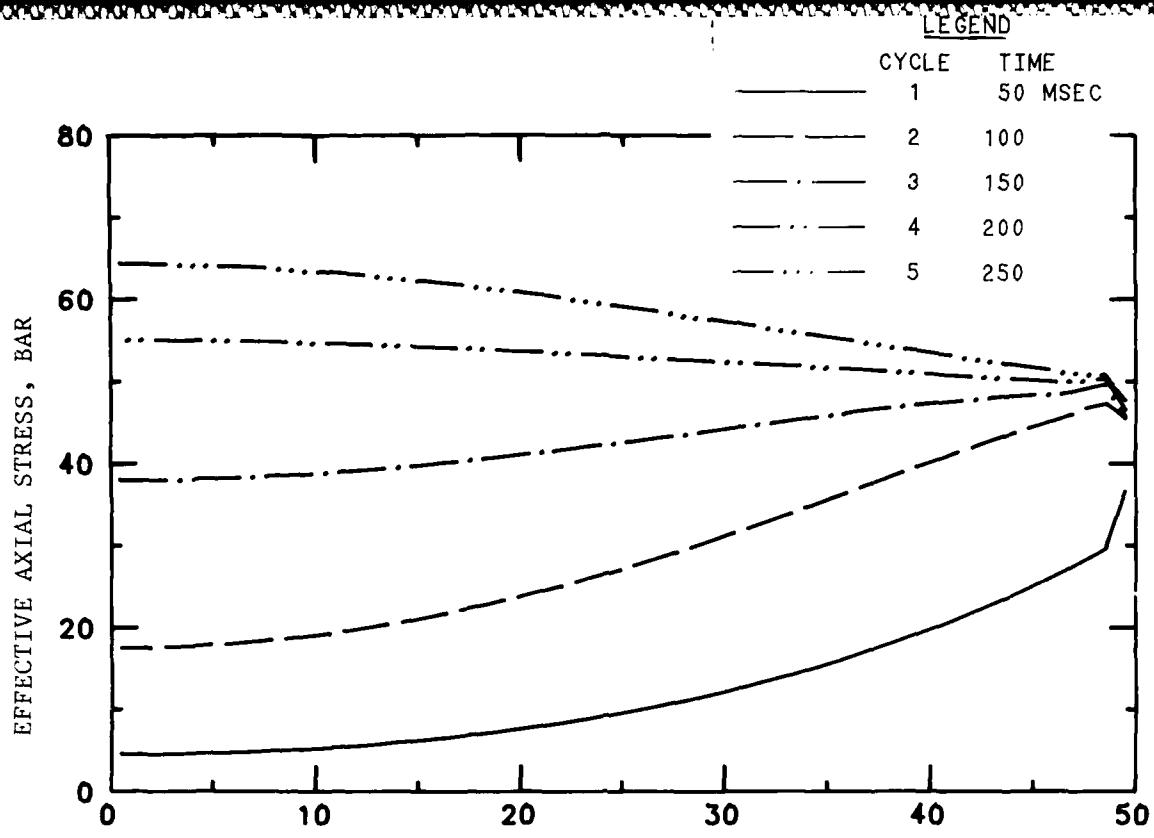


Figure 3.7. Effective axial stress and particle velocity versus position at various times for Case E224.

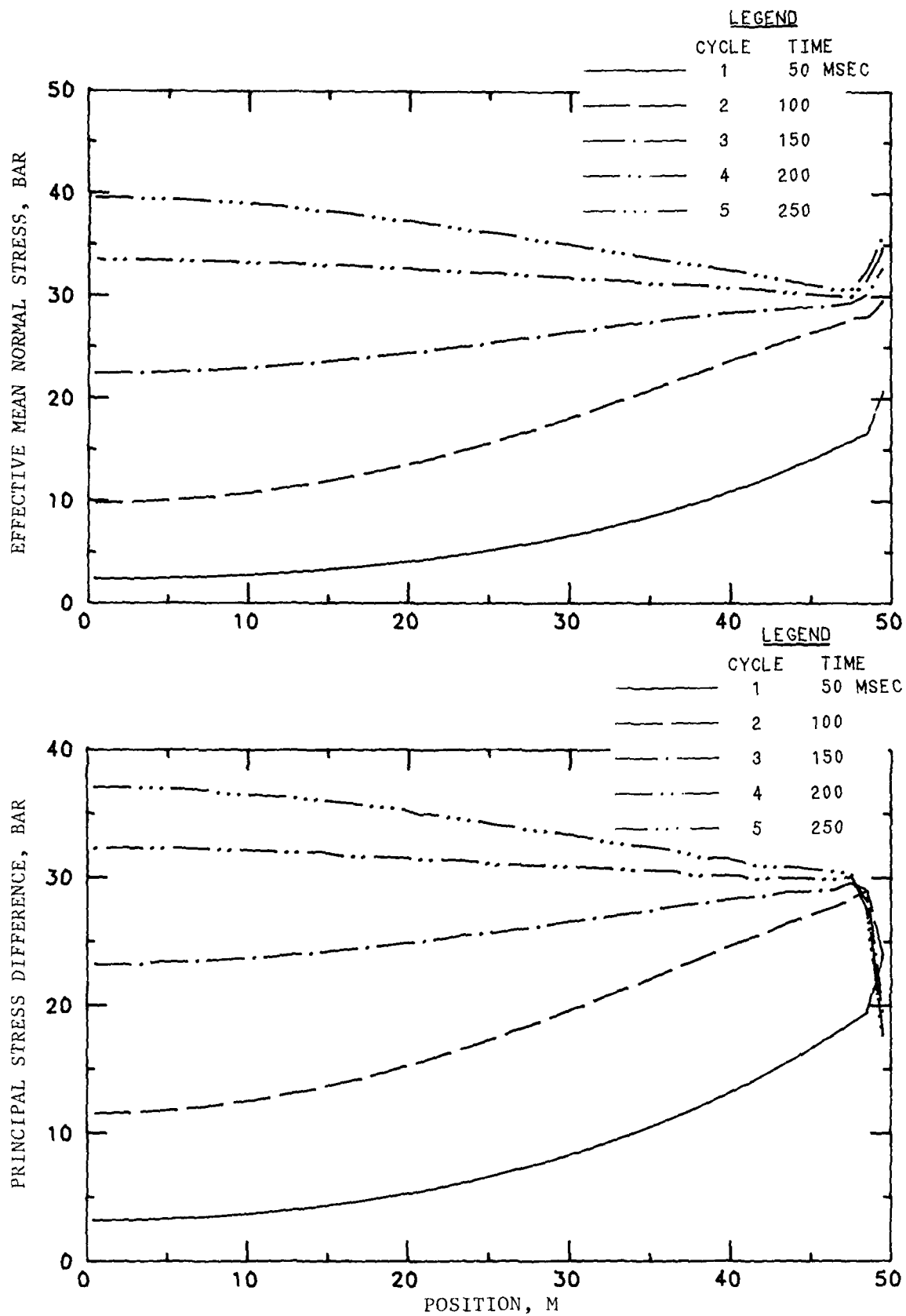


Figure 3.8. Effective mean normal stress and principal stress difference versus position at various times for Case E224.

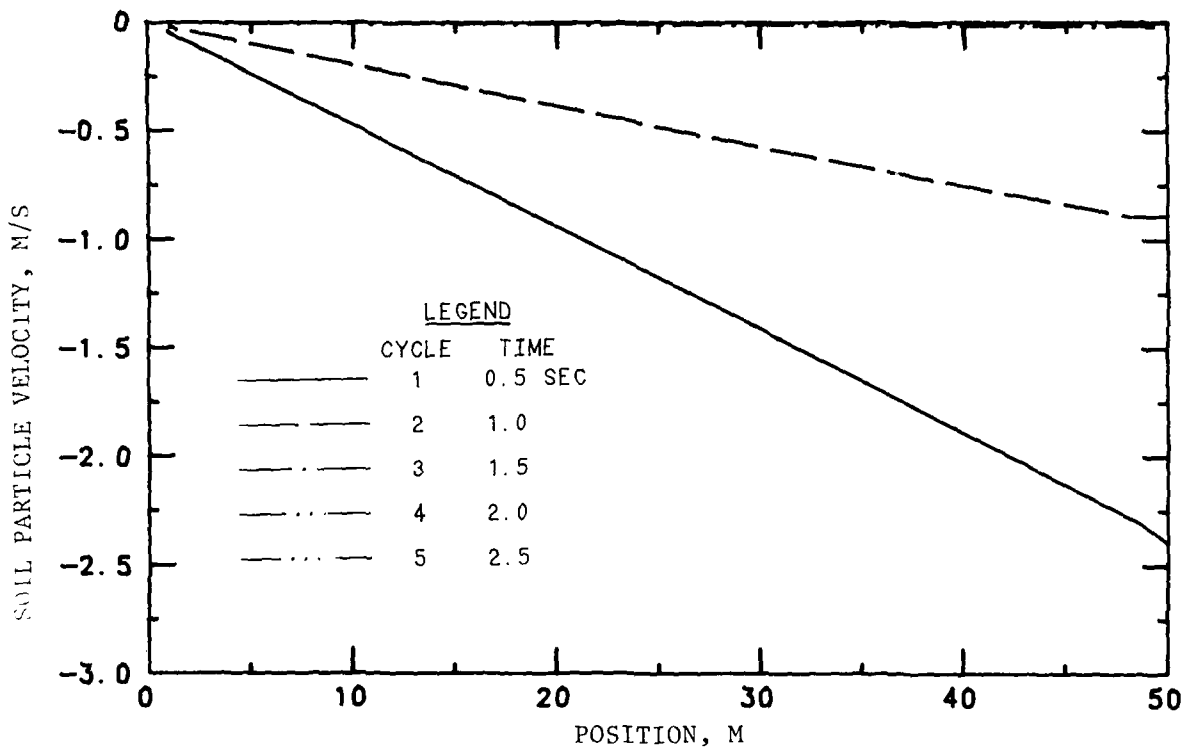
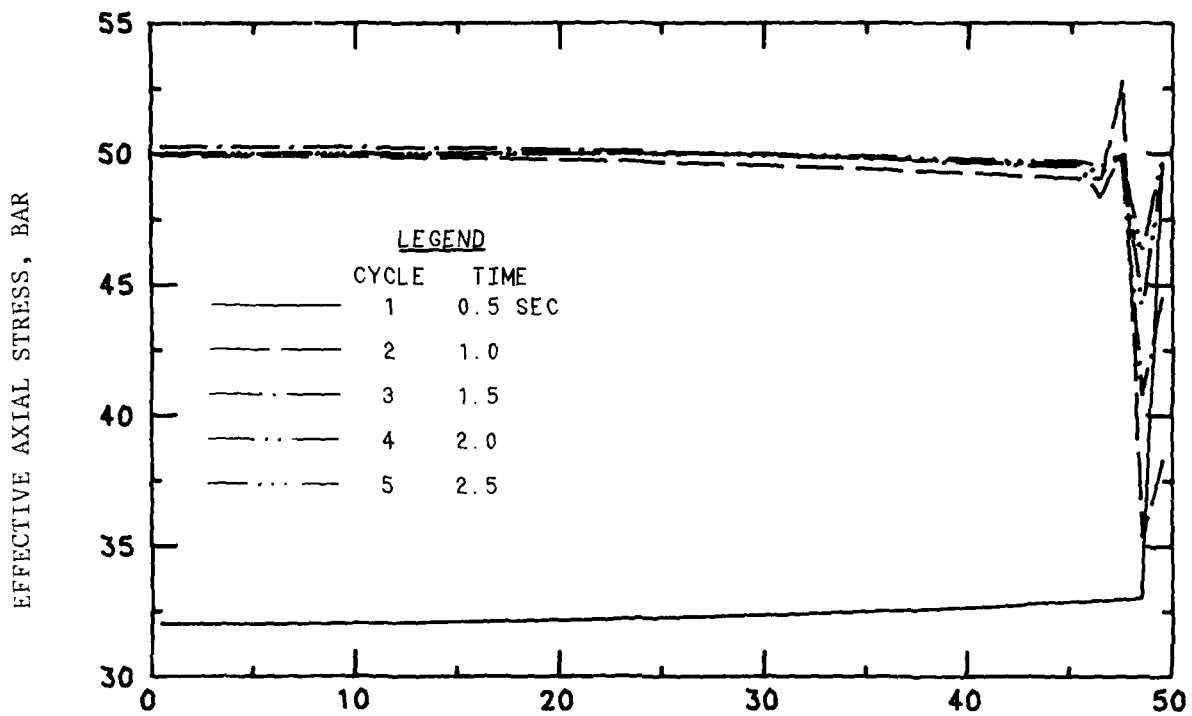


Figure 3.9. Effective axial stress and particle velocity versus position at various times for Case E225.

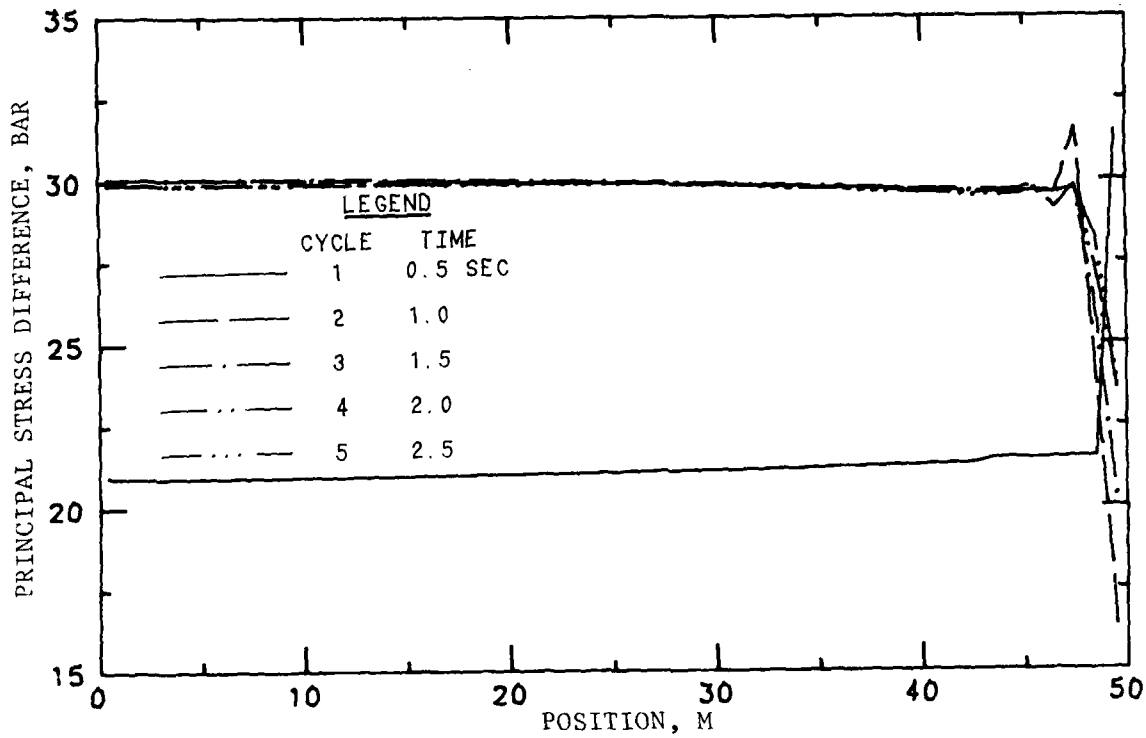
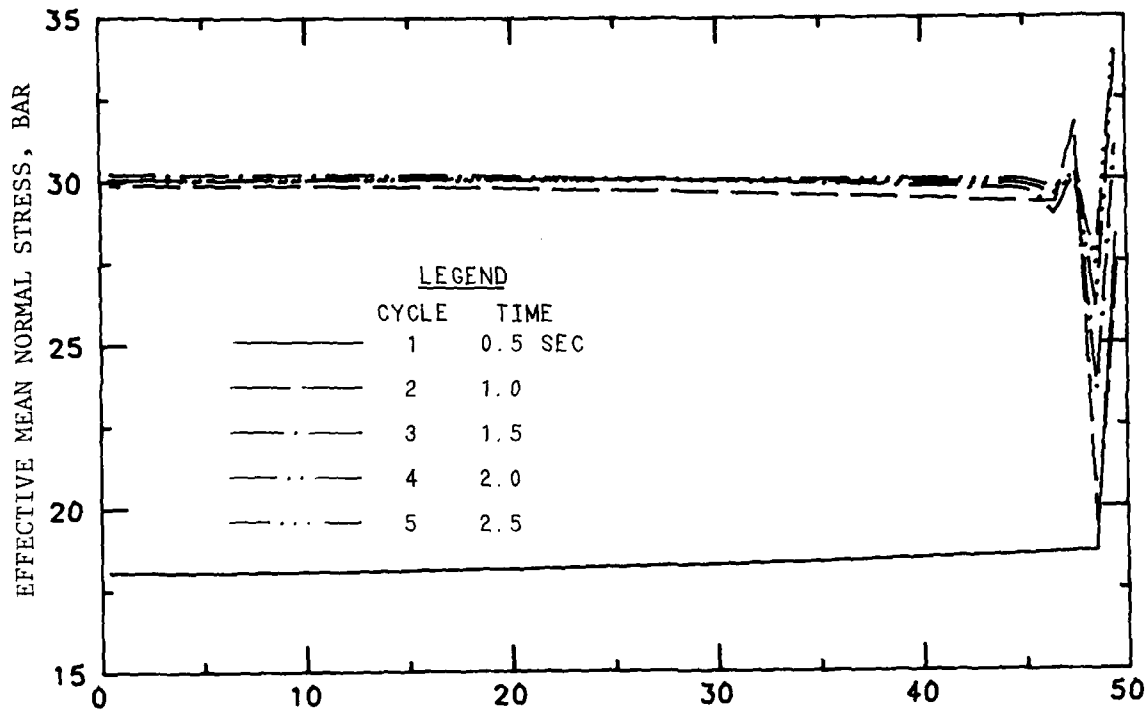


Figure 3.10. Effective mean normal stress and principal stress difference versus position at various times for Case E225.

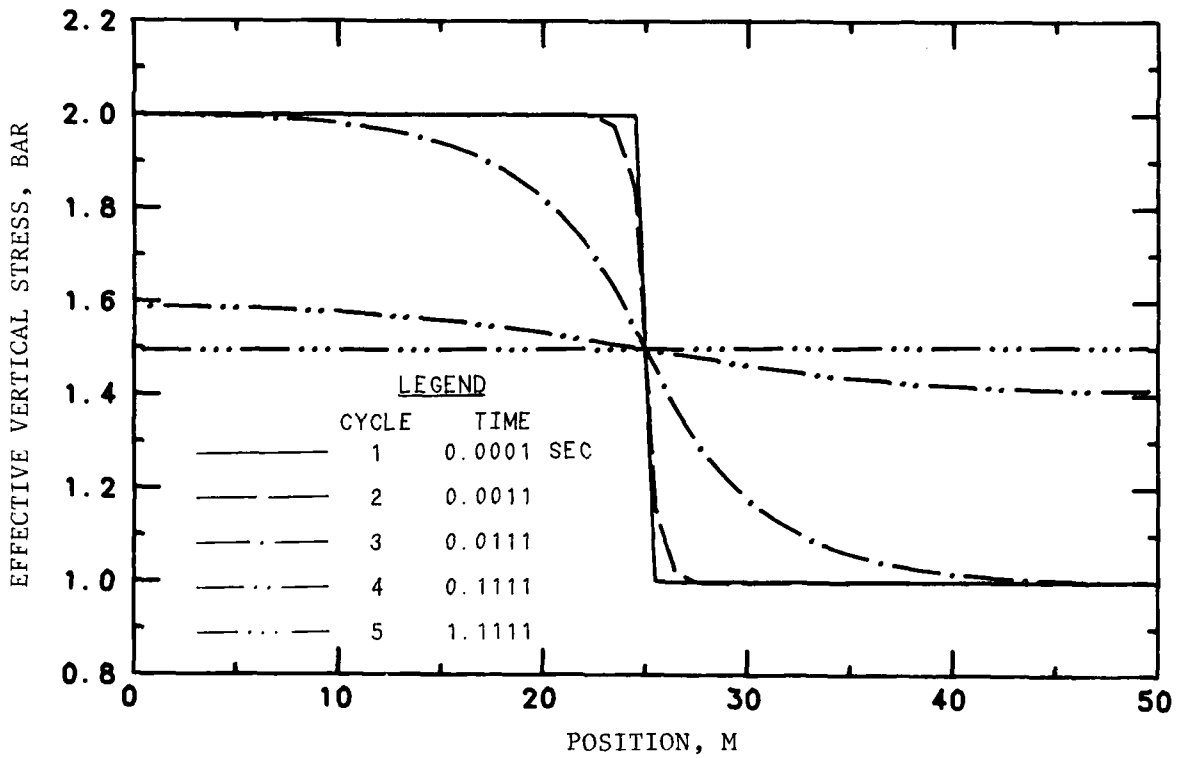
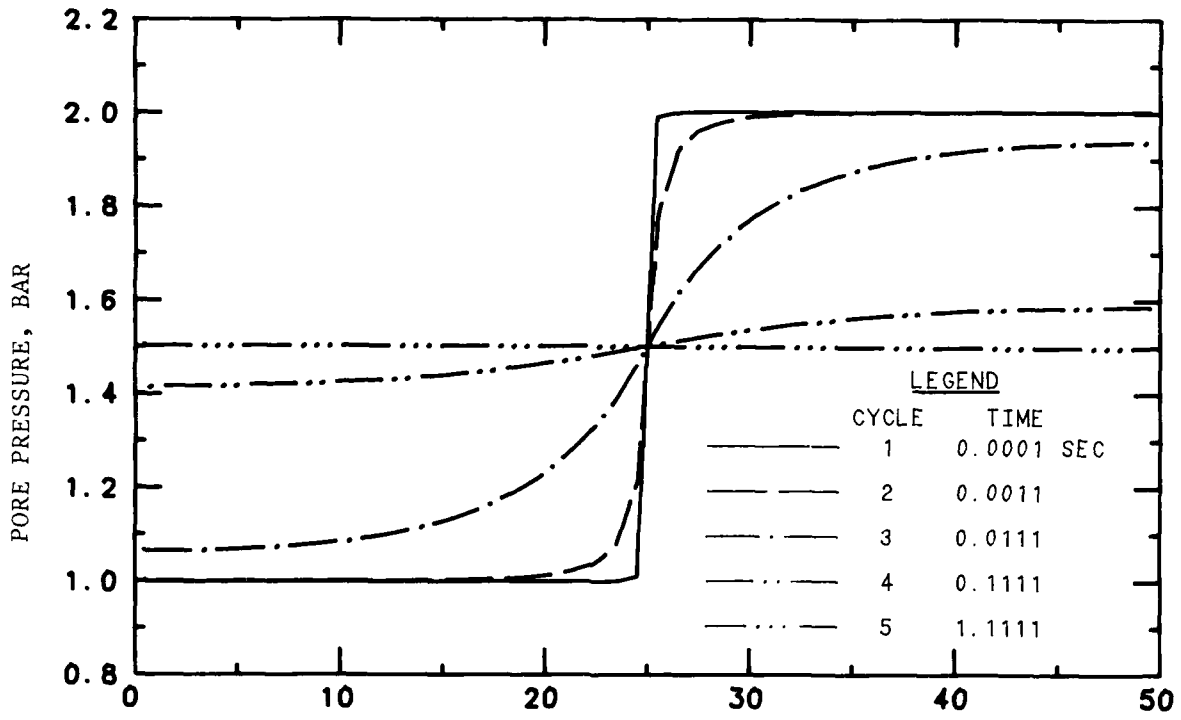


Figure 3.11. Pore-fluid pressure and effective vertical stress versus position at various times for Case E129.

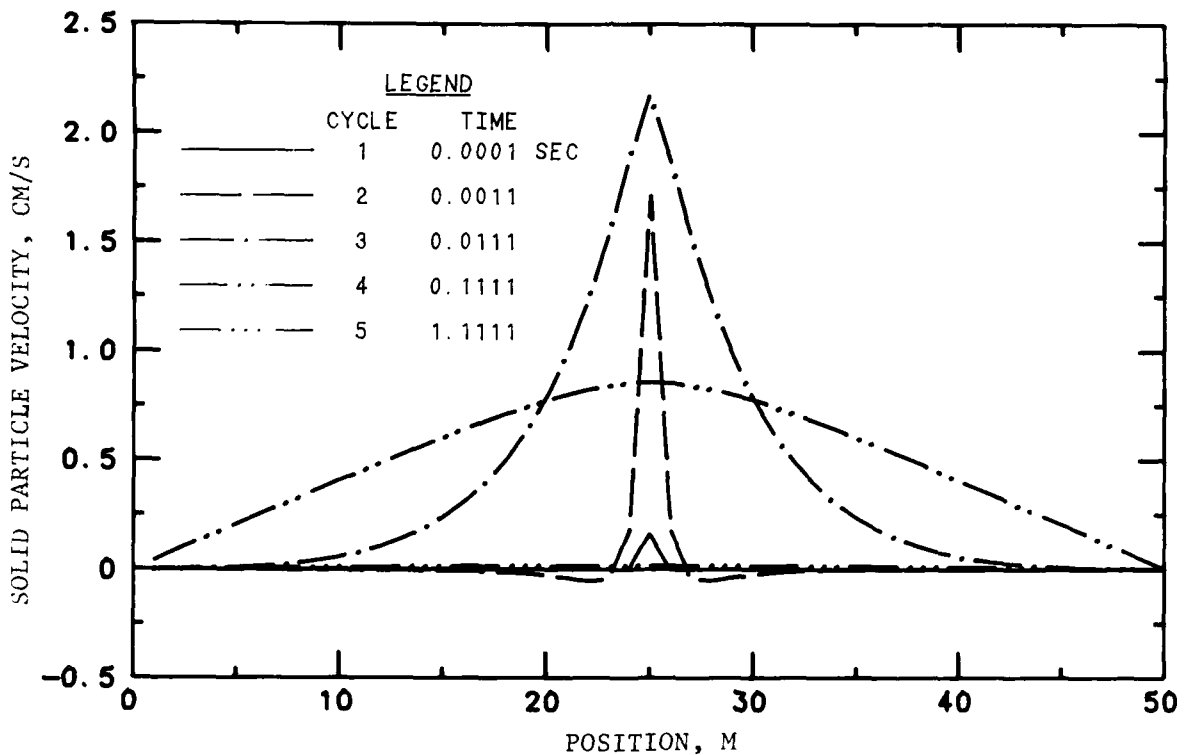
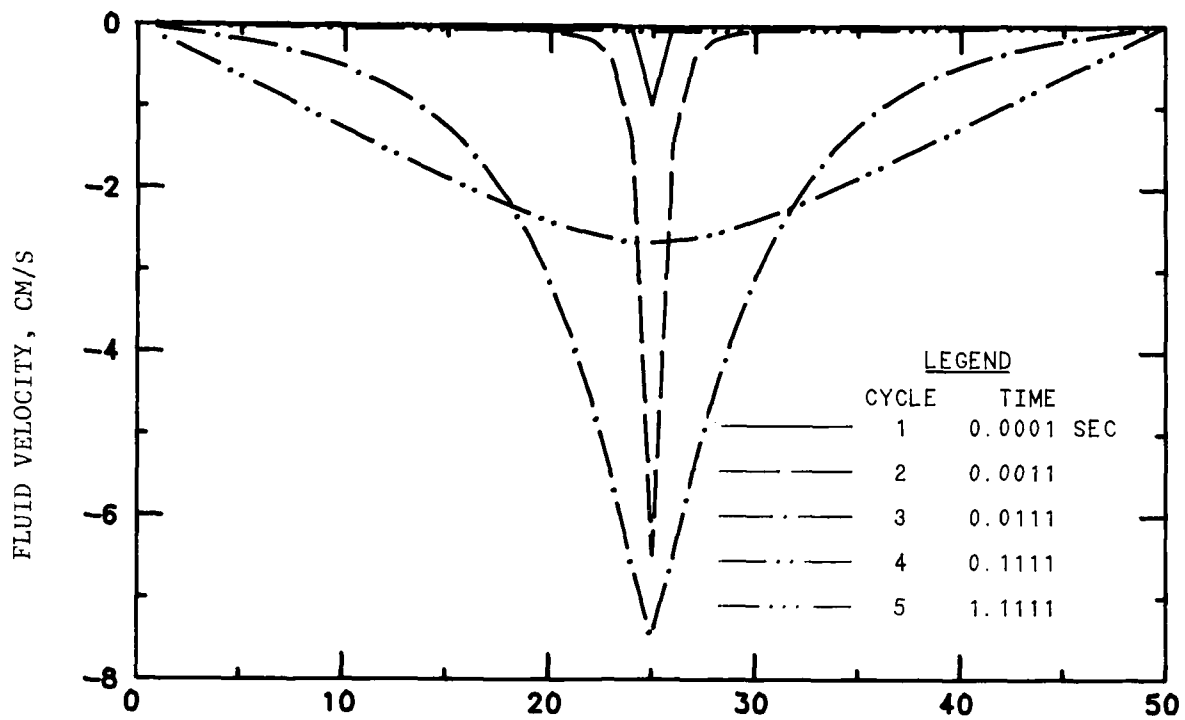


Figure 3.12. Fluid velocity and solid particle velocity versus position at various times for Case E129.

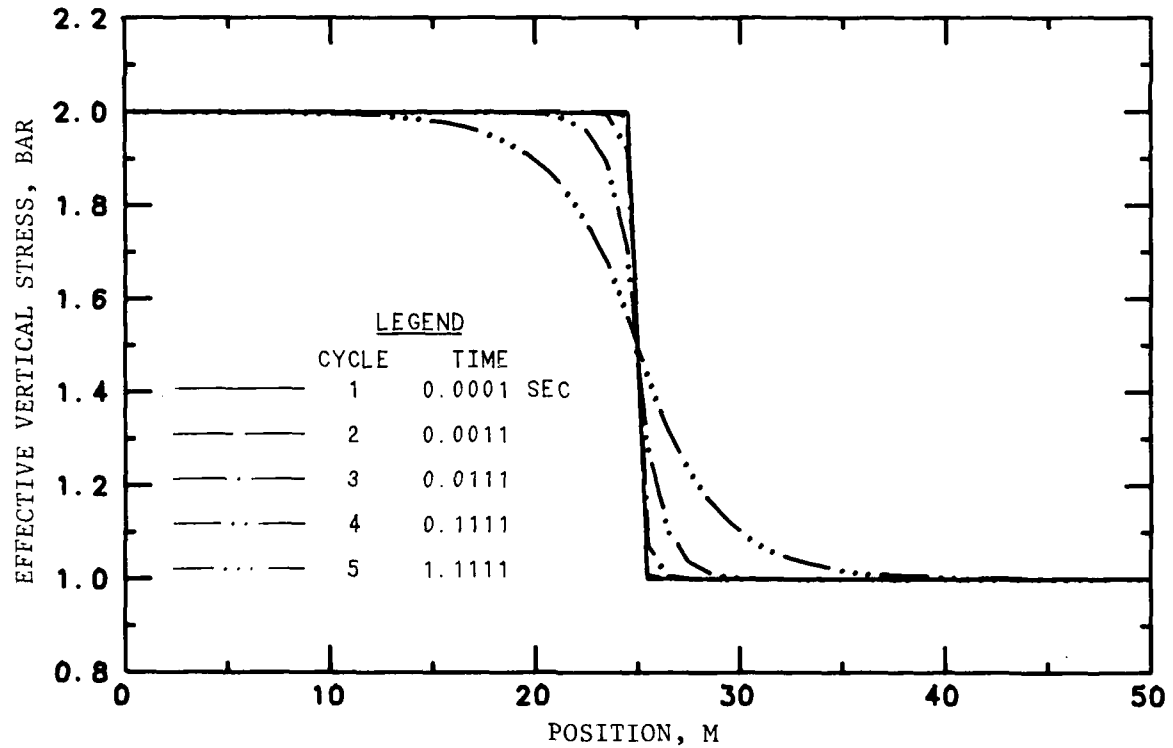
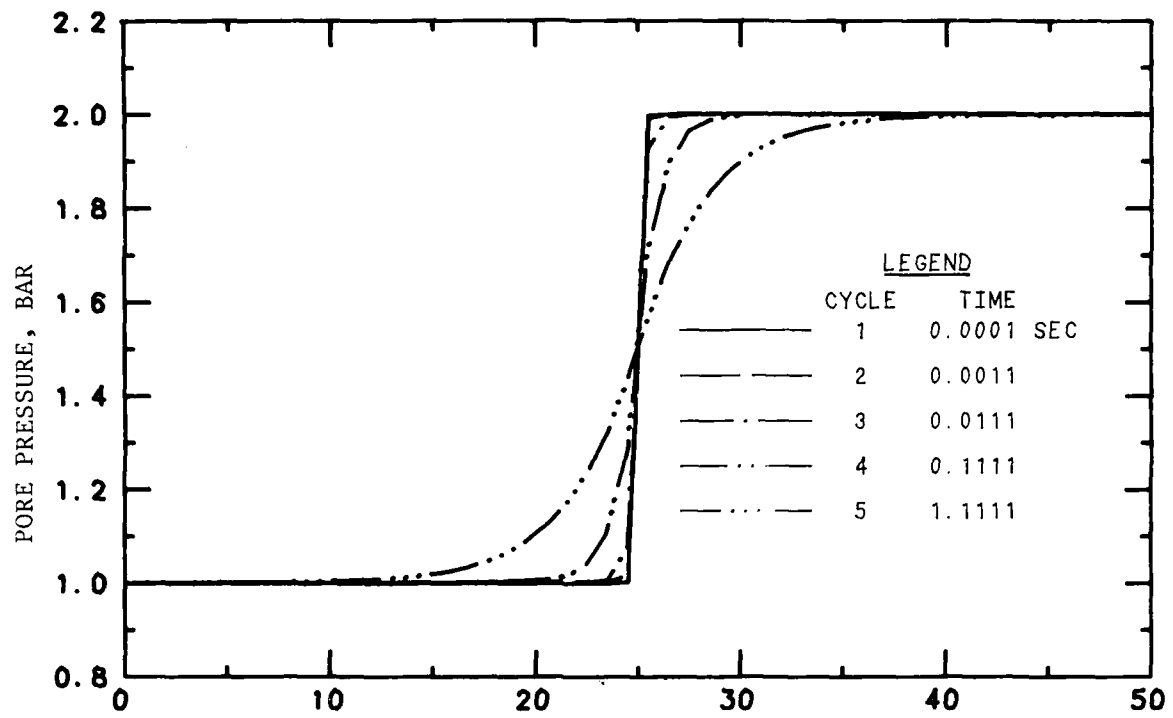


Figure 3.13. Pore-fluid pressure and effective vertical stress versus position at various times for Case E130.

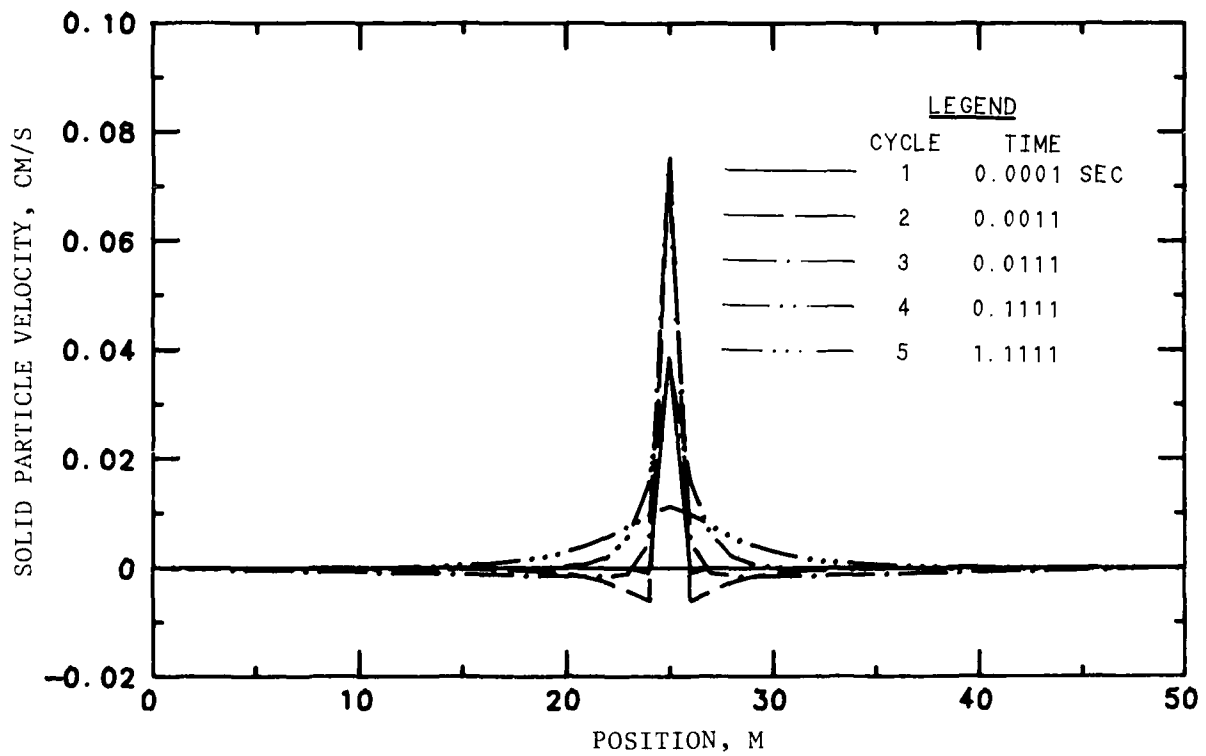
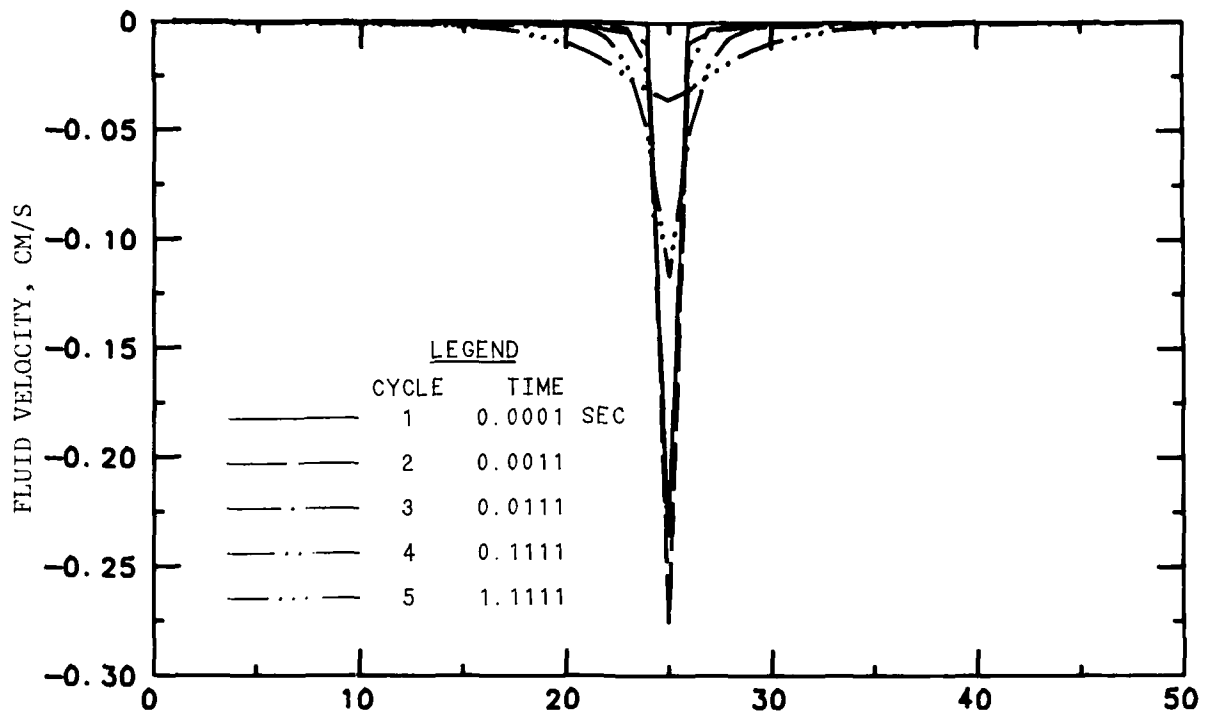


Figure 3.14. Fluid velocity and solid particle velocity versus position at various times for Case E130.

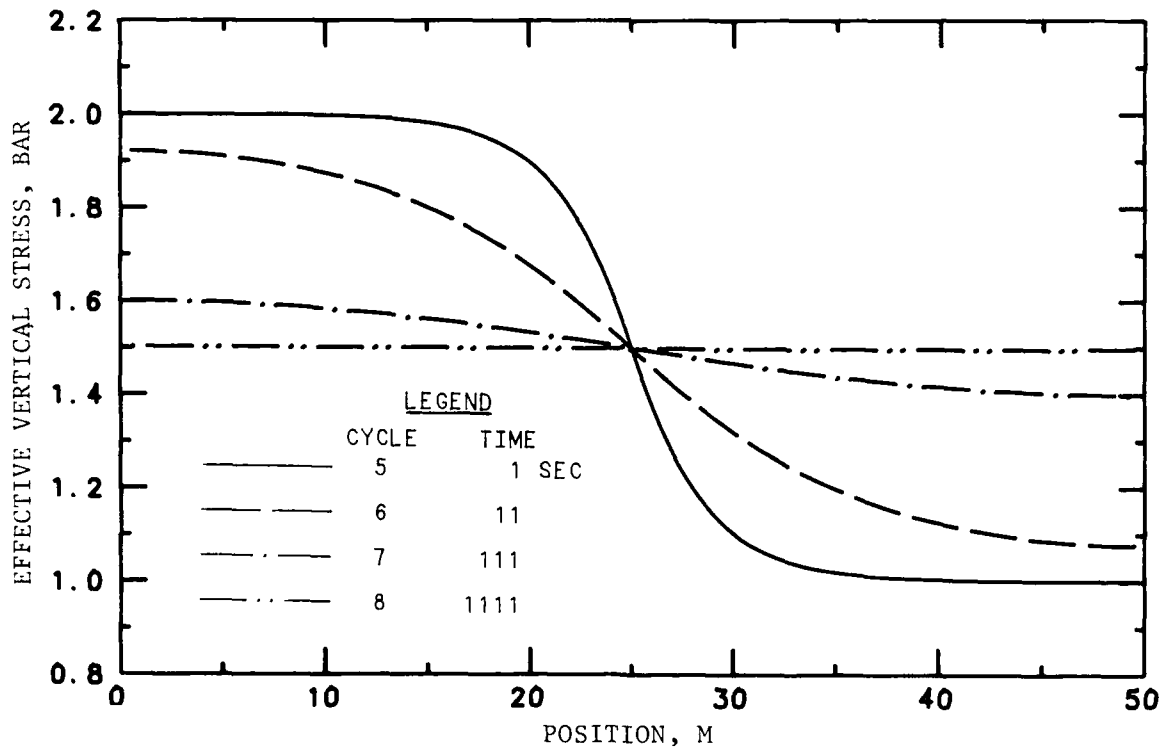
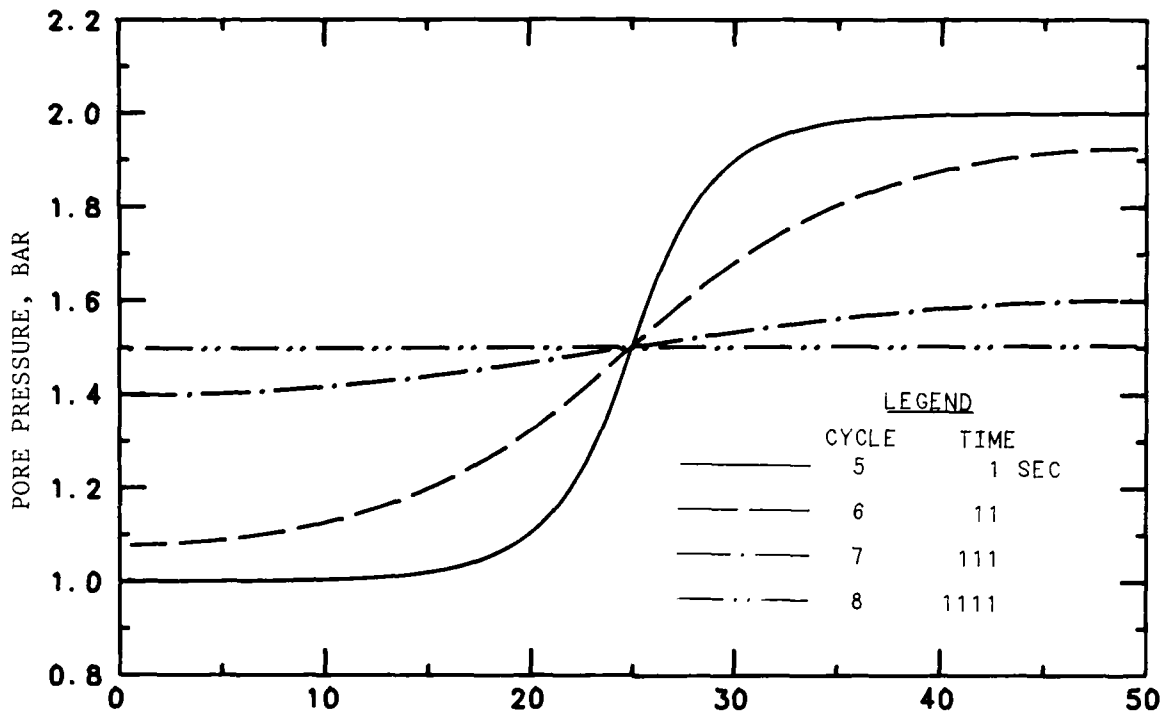


Figure 3.15. Pore-fluid pressure and effective vertical stress versus position at late times for Case E130.

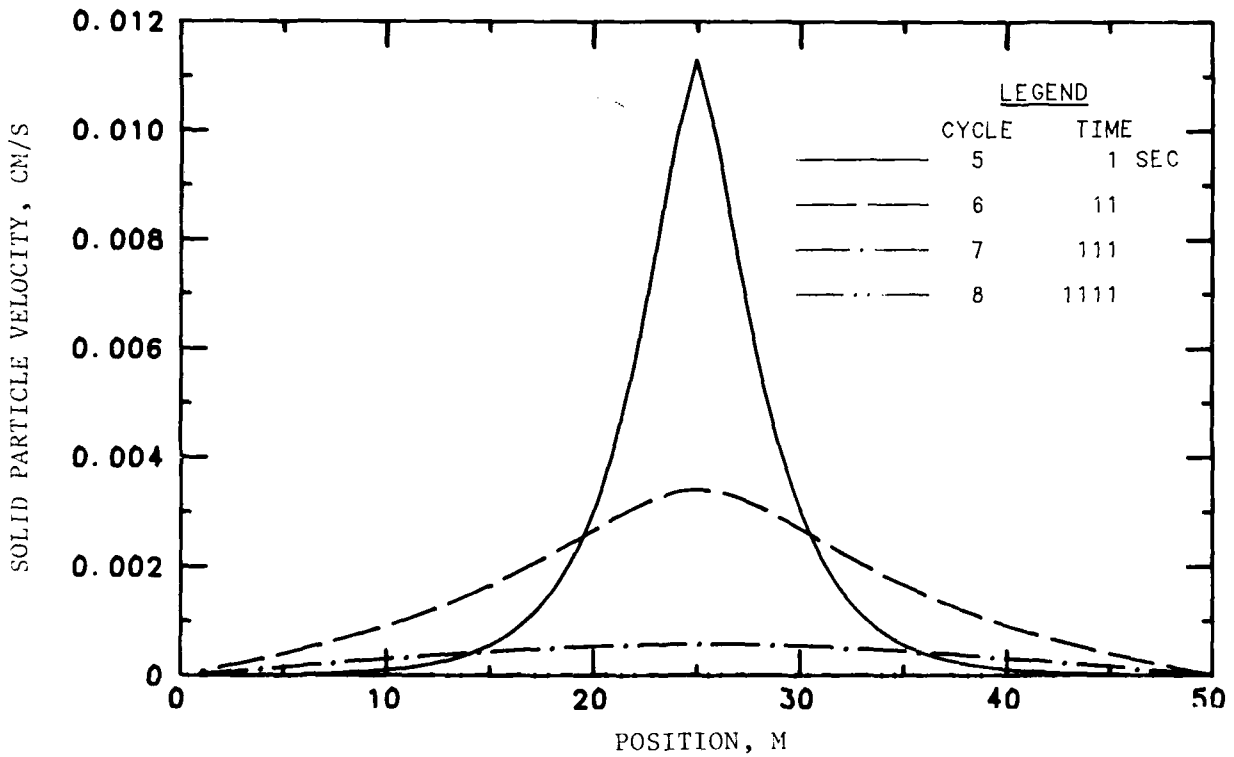
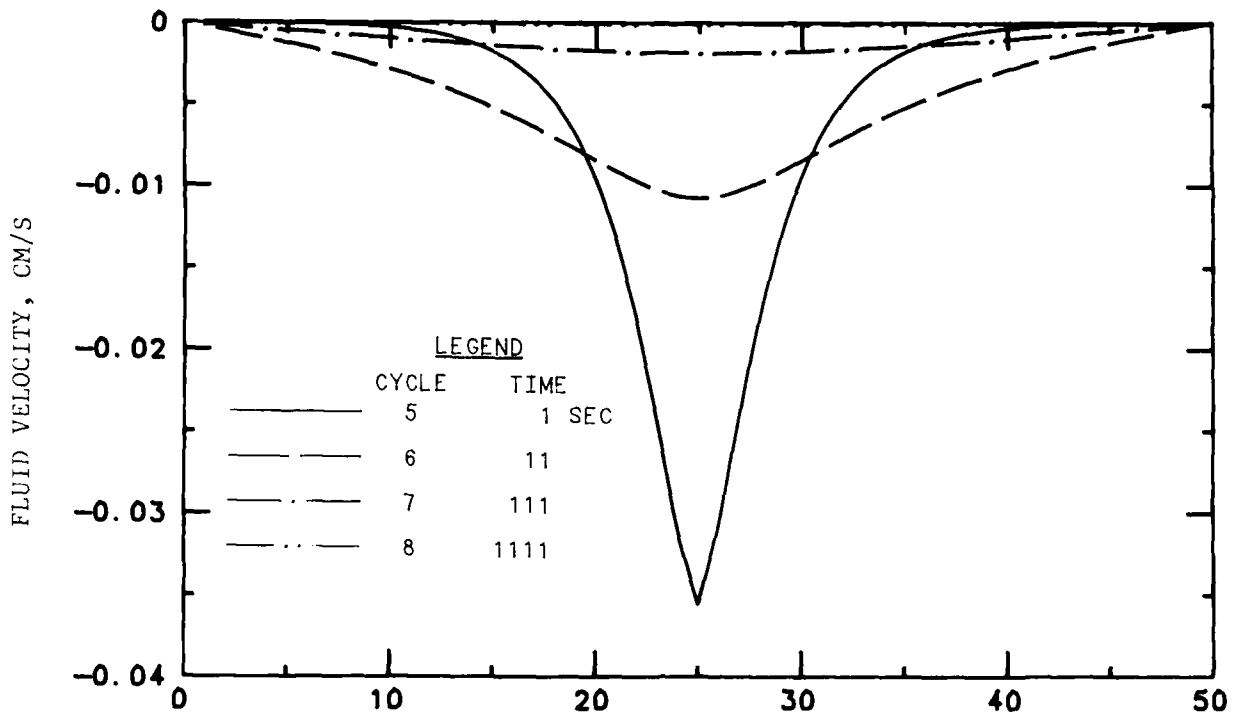
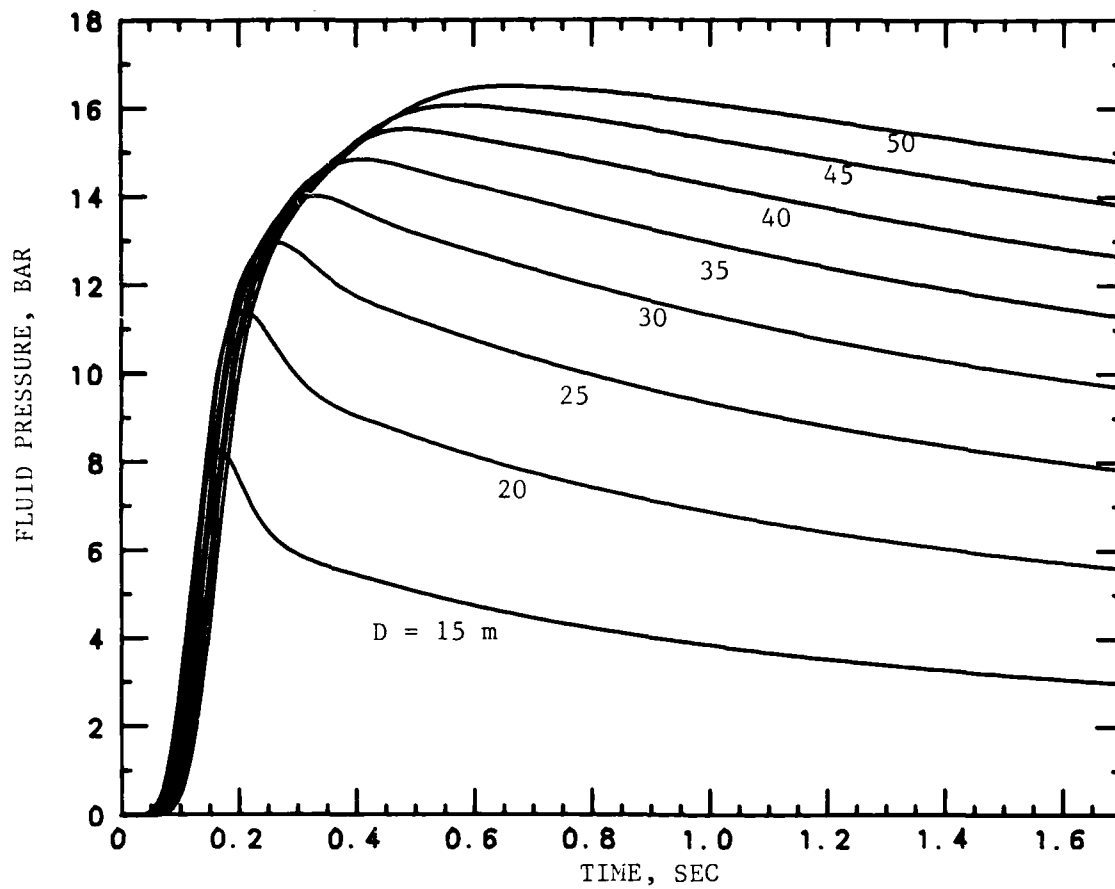
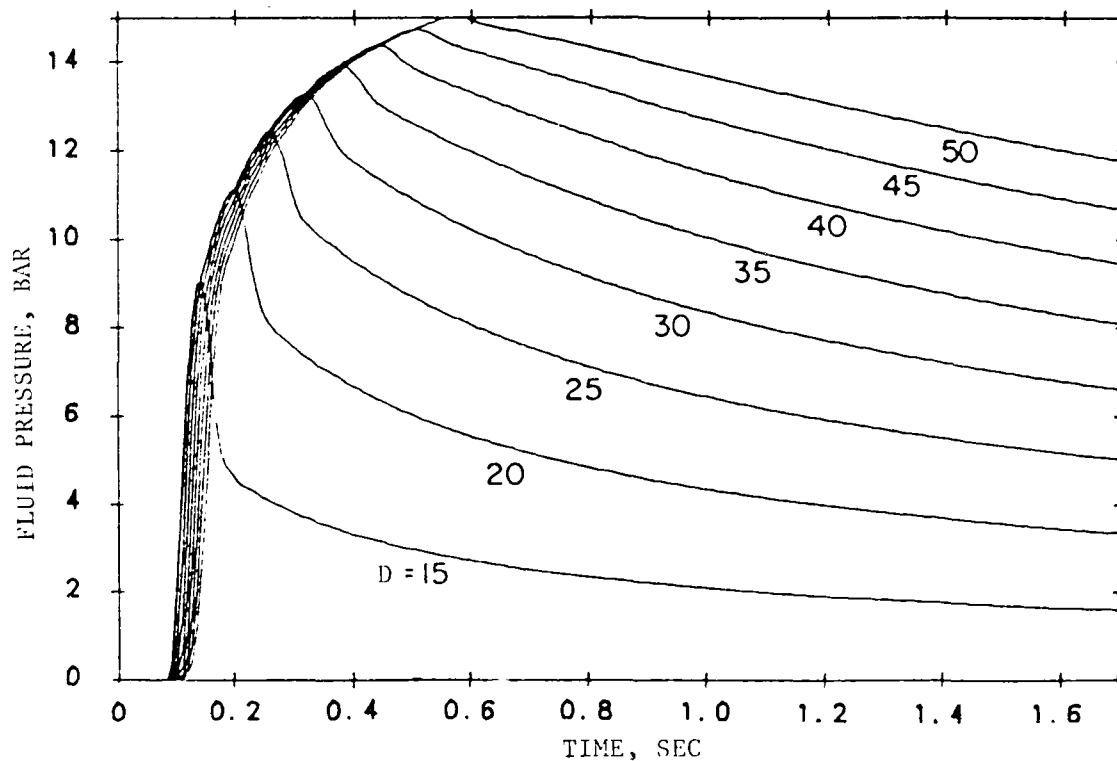


Figure 3.16. Fluid velocity and solid particle velocity versus position at late times for Case E130.



a) CRT Calculation



b) Prevost Calculation

Figure 3.17. Comparison of pore-fluid pressure time histories between Case E444 and Prevost calculation (Reference 8).

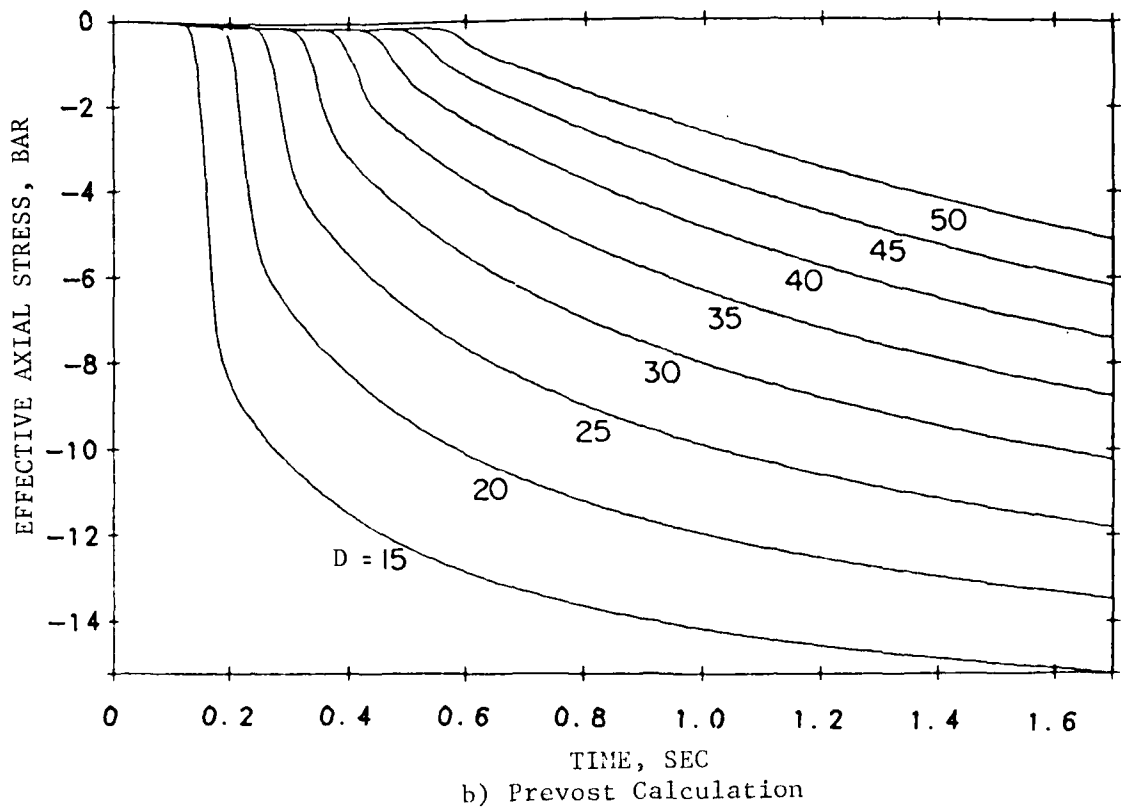
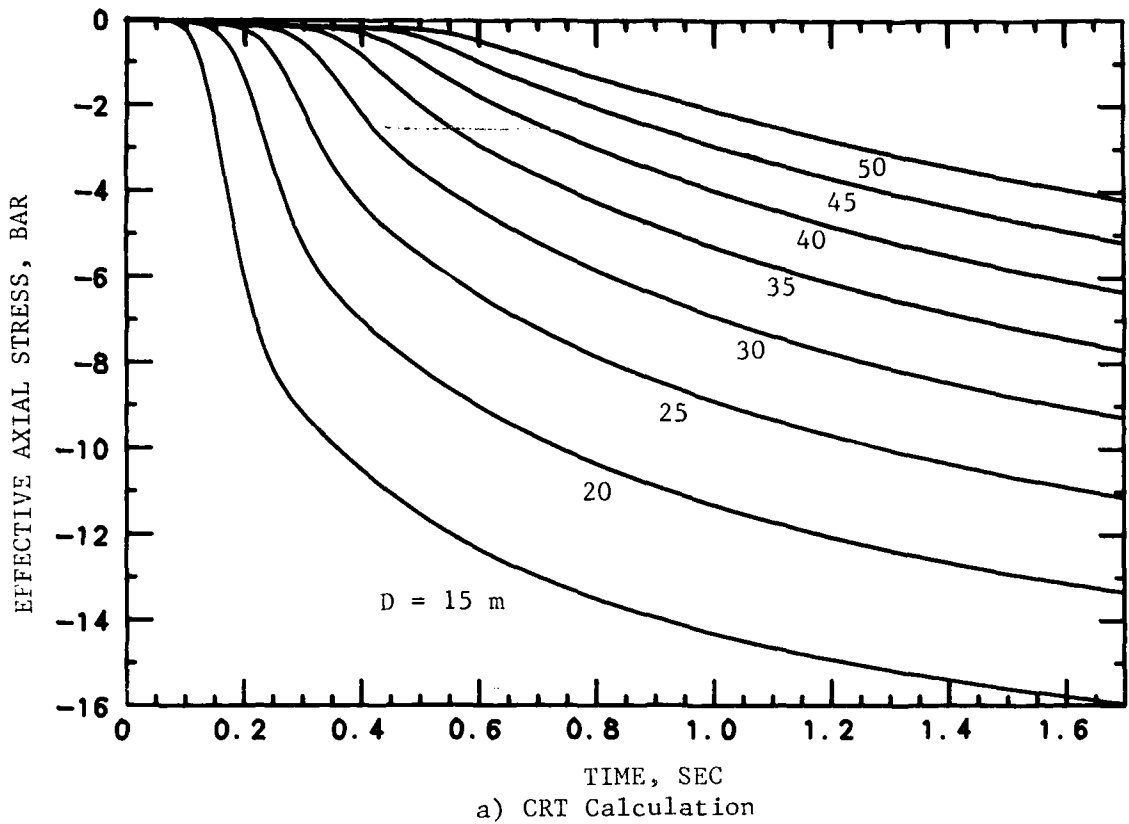


Figure 3.18. Comparison of effective stress time histories between Case E444 and Prevost calculation (Reference 8).

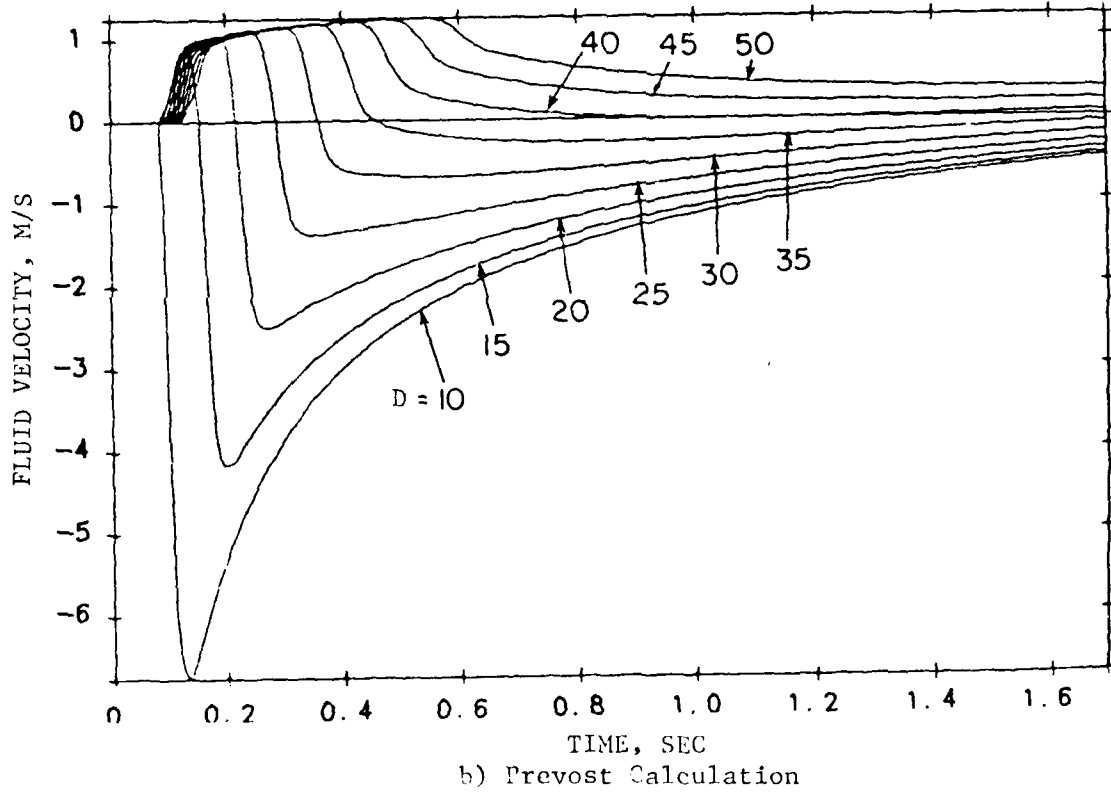
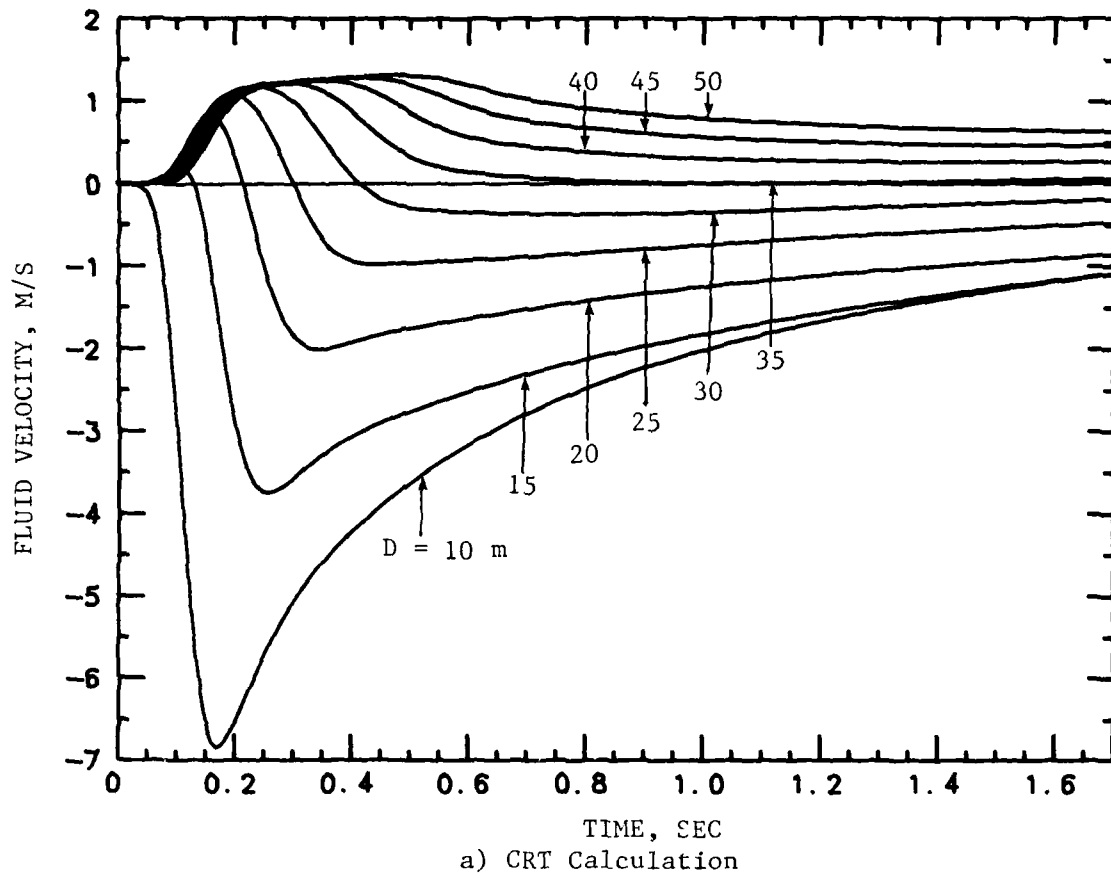
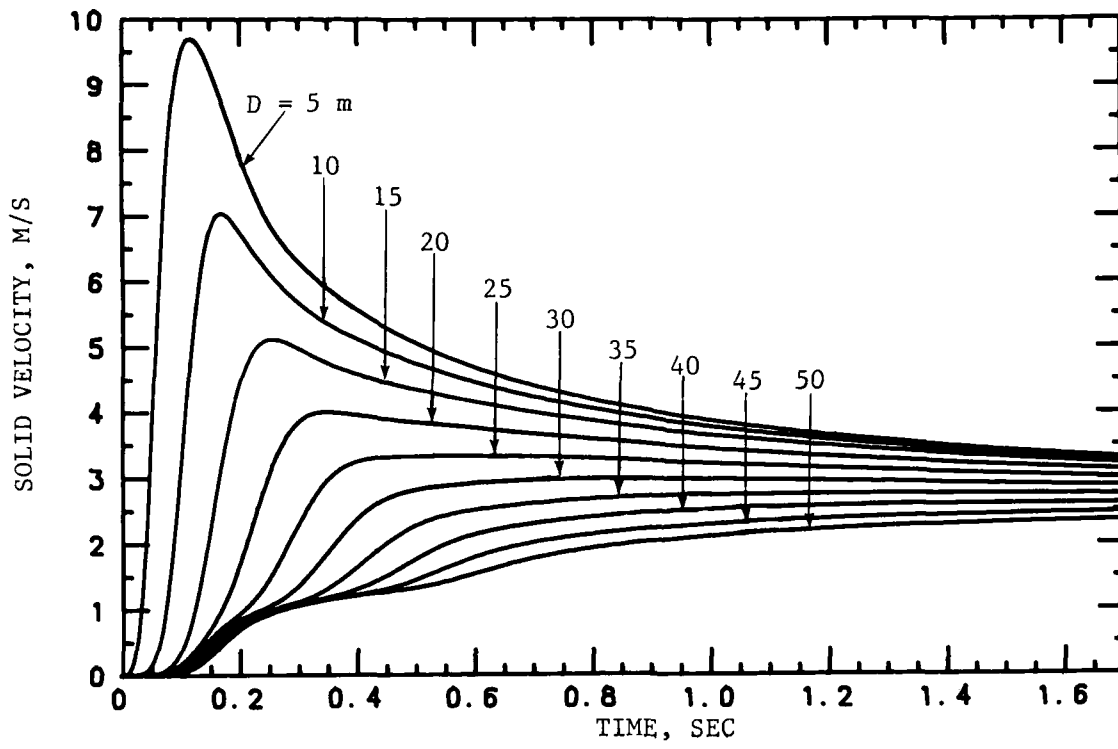
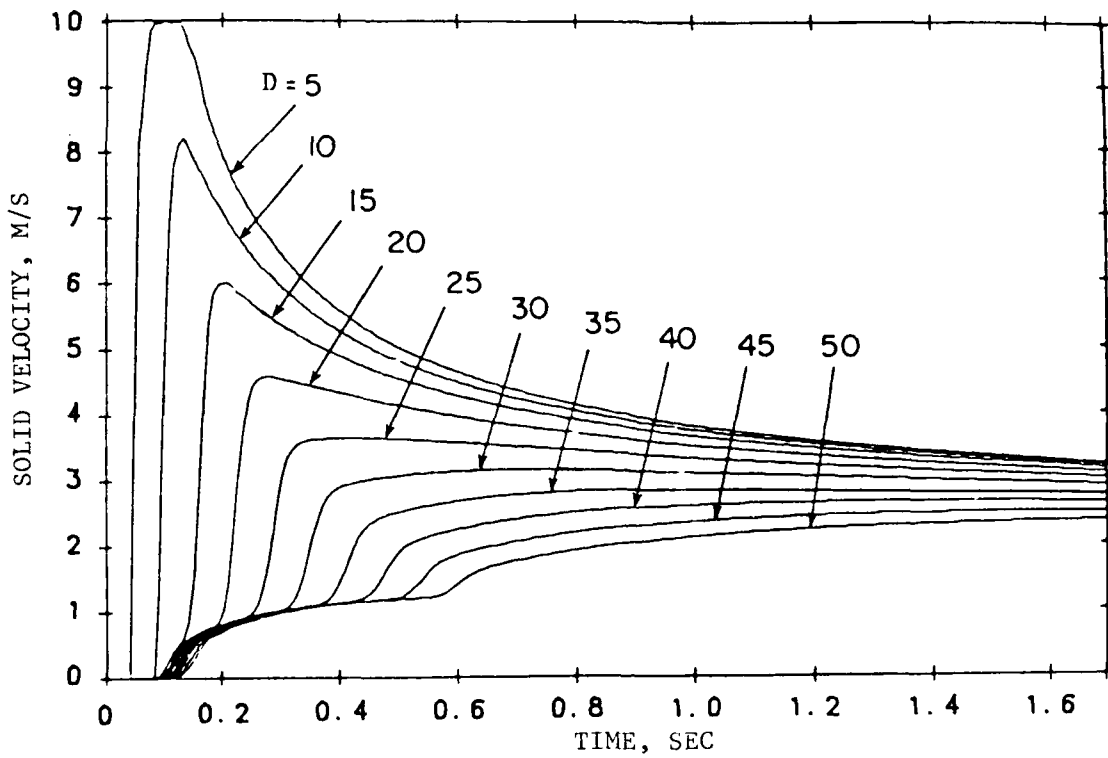


Figure 3.19. Comparison of fluid velocity time history between Case E444 and Prevost calculation (Reference 8).



a) CRT Calculation



b) Prevost Calculation

Figure 3.20. Comparison of solid particle velocity time histories between Case E444 and Prevost calculation (Reference 8).

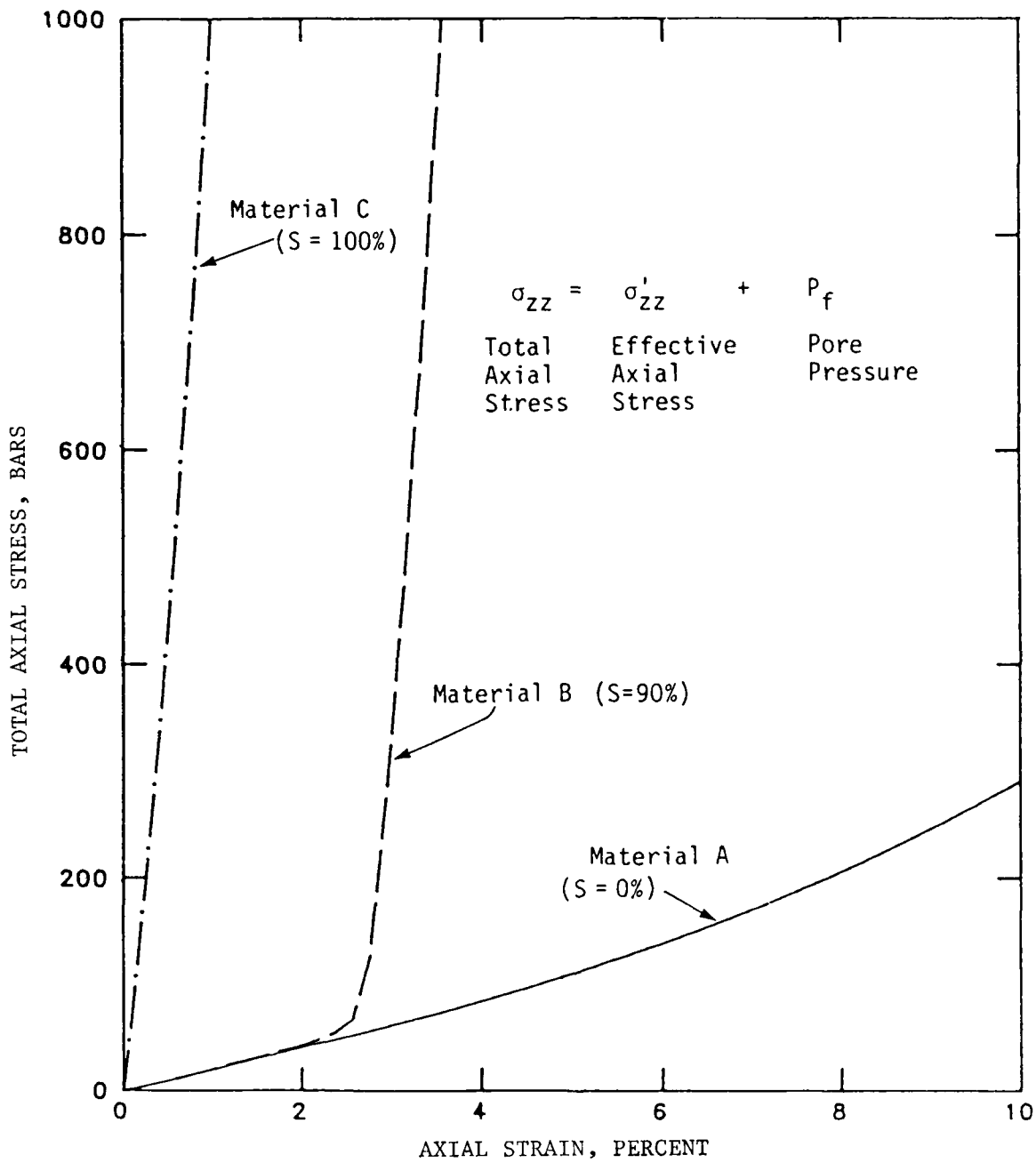


Figure 3.21. Uniaxial strain (UX) total stress-strain response for Materials A, B and C.

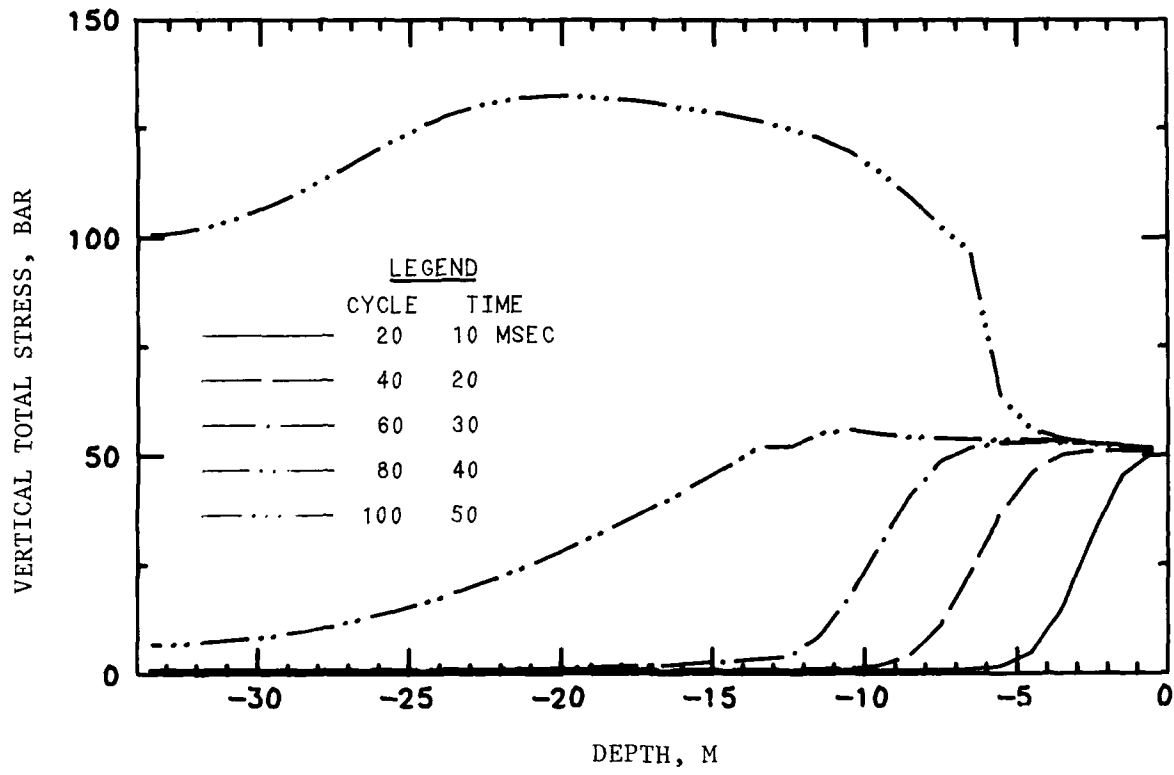


Figure 3.22. Total vertical stress versus depth at various times for Case E605.

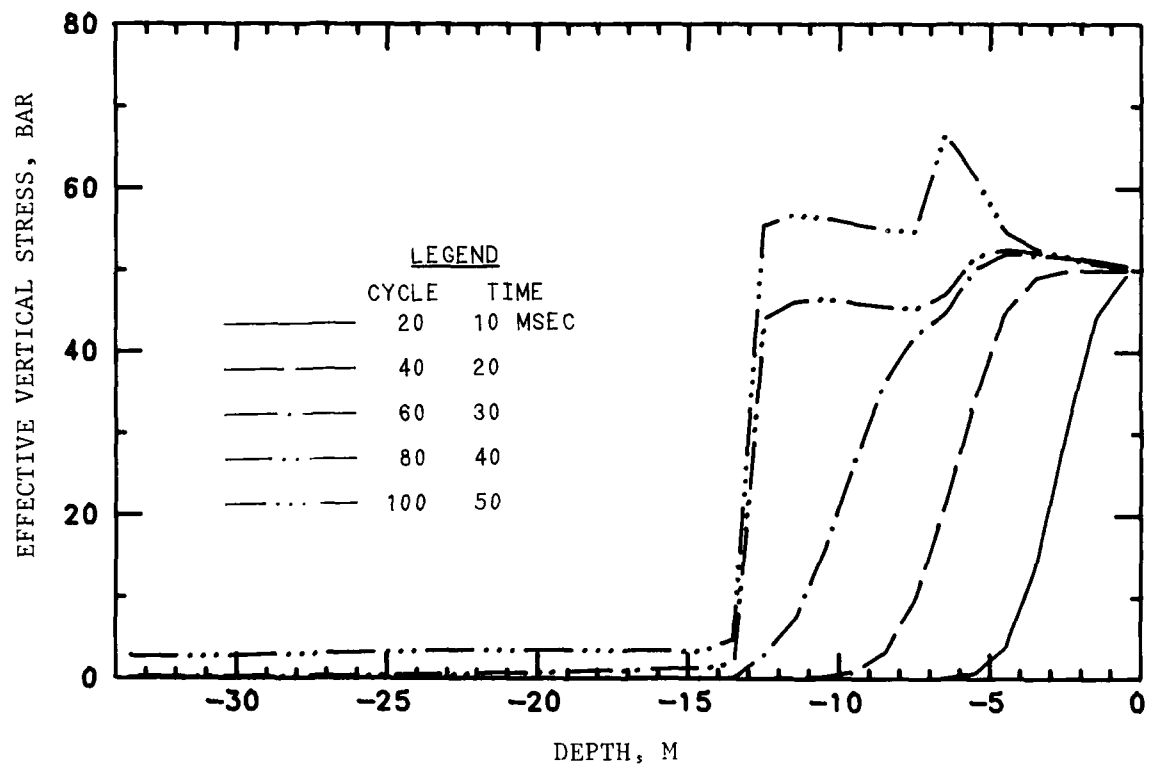
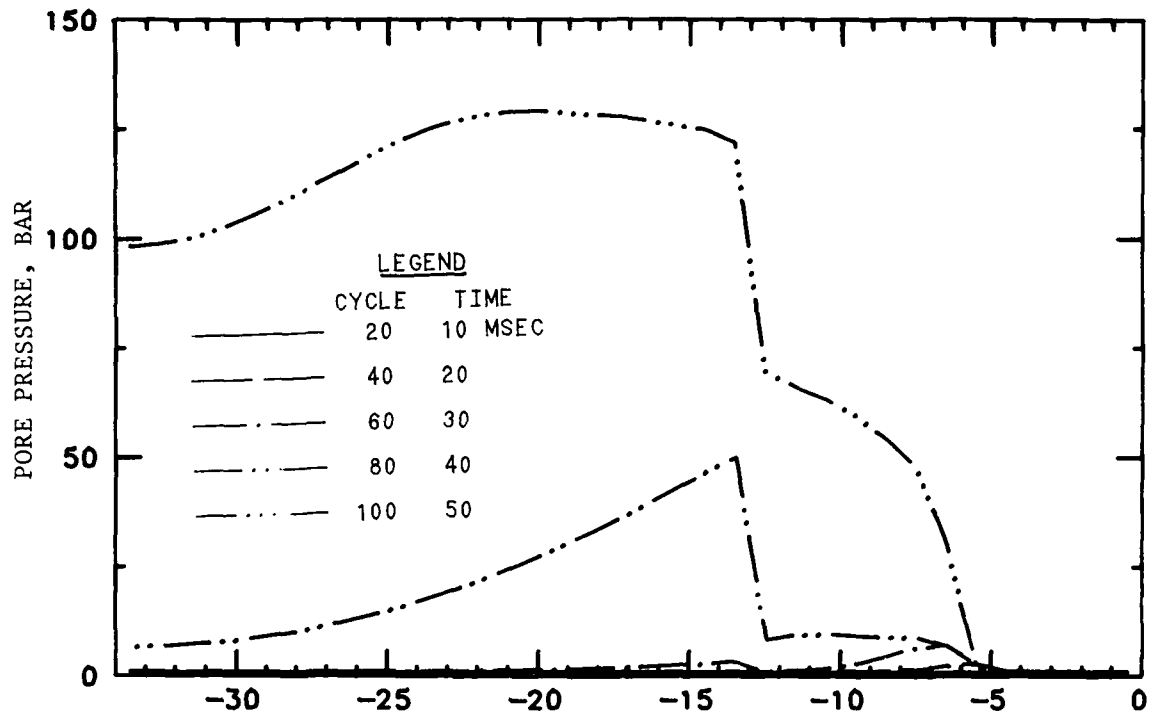


Figure 3.23. Pore-fluid pressure and effective vertical stress versus depth at various times for Case E605.

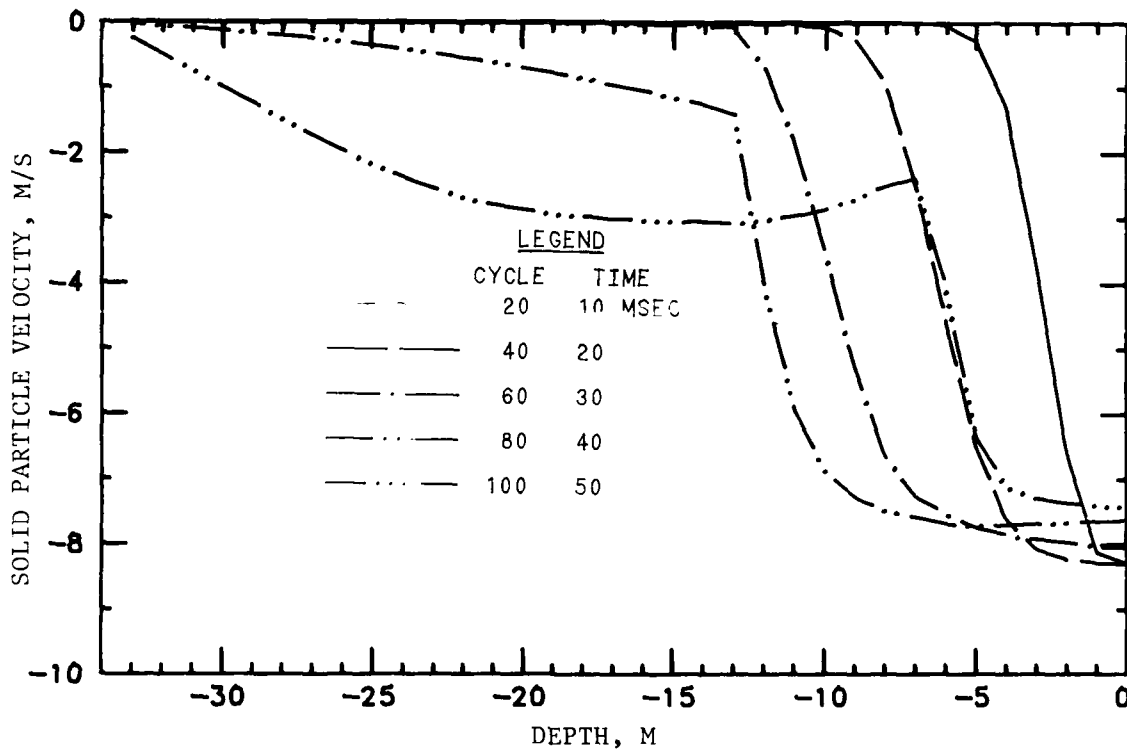
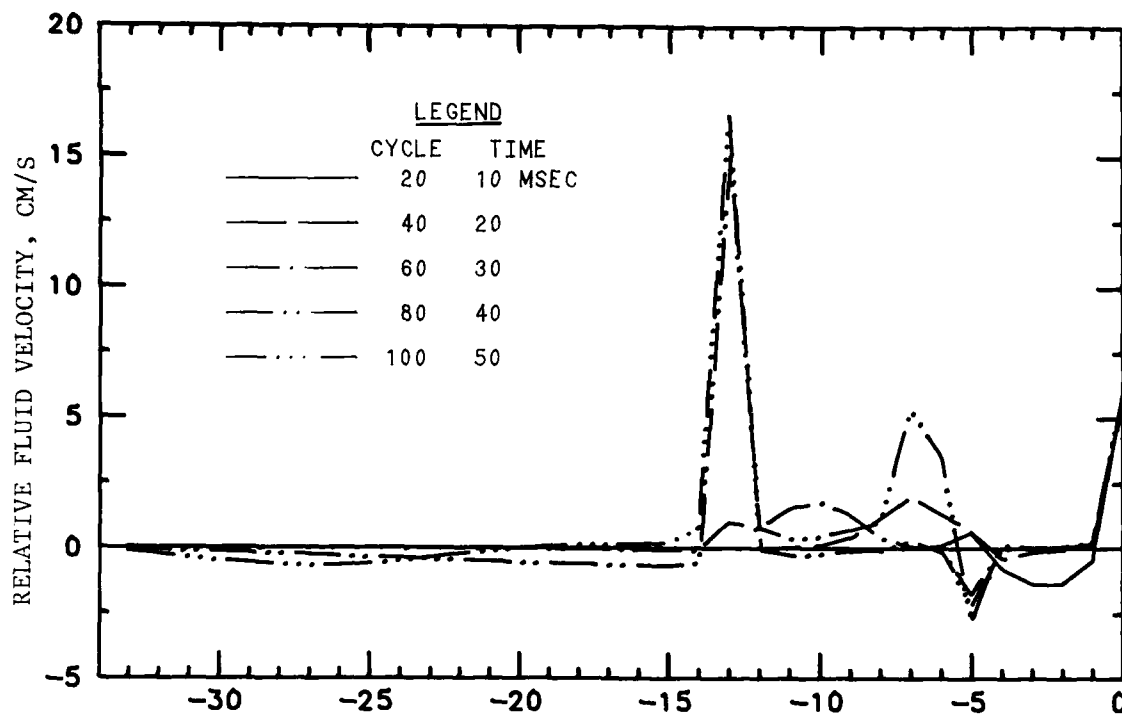


Figure 3.24. Relative fluid velocity and solid particle velocity versus depth at various times for Case E605.

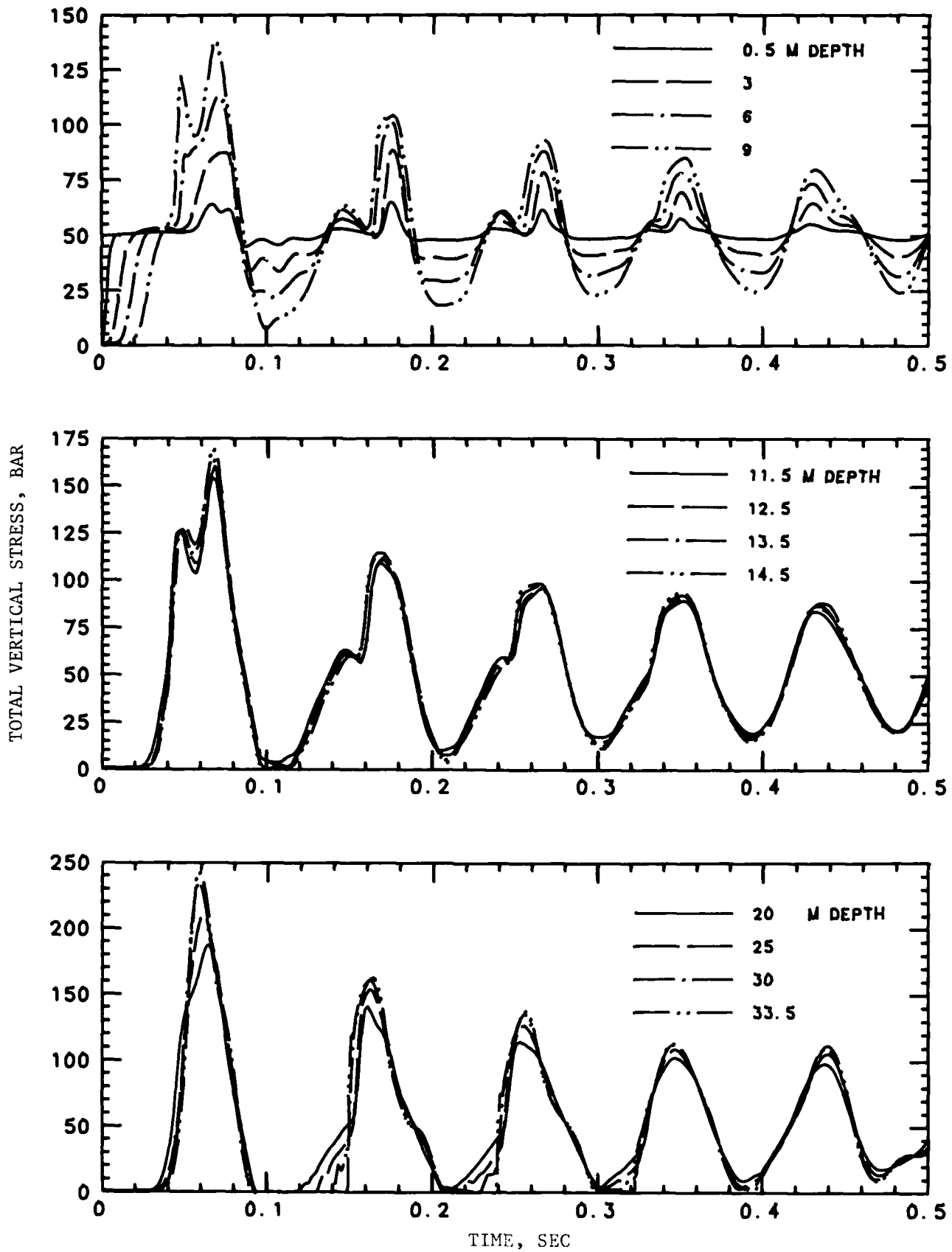


Figure 3.25. Total vertical stress versus time ($0 < t < 0.5$ sec) at various depths for Case E605.

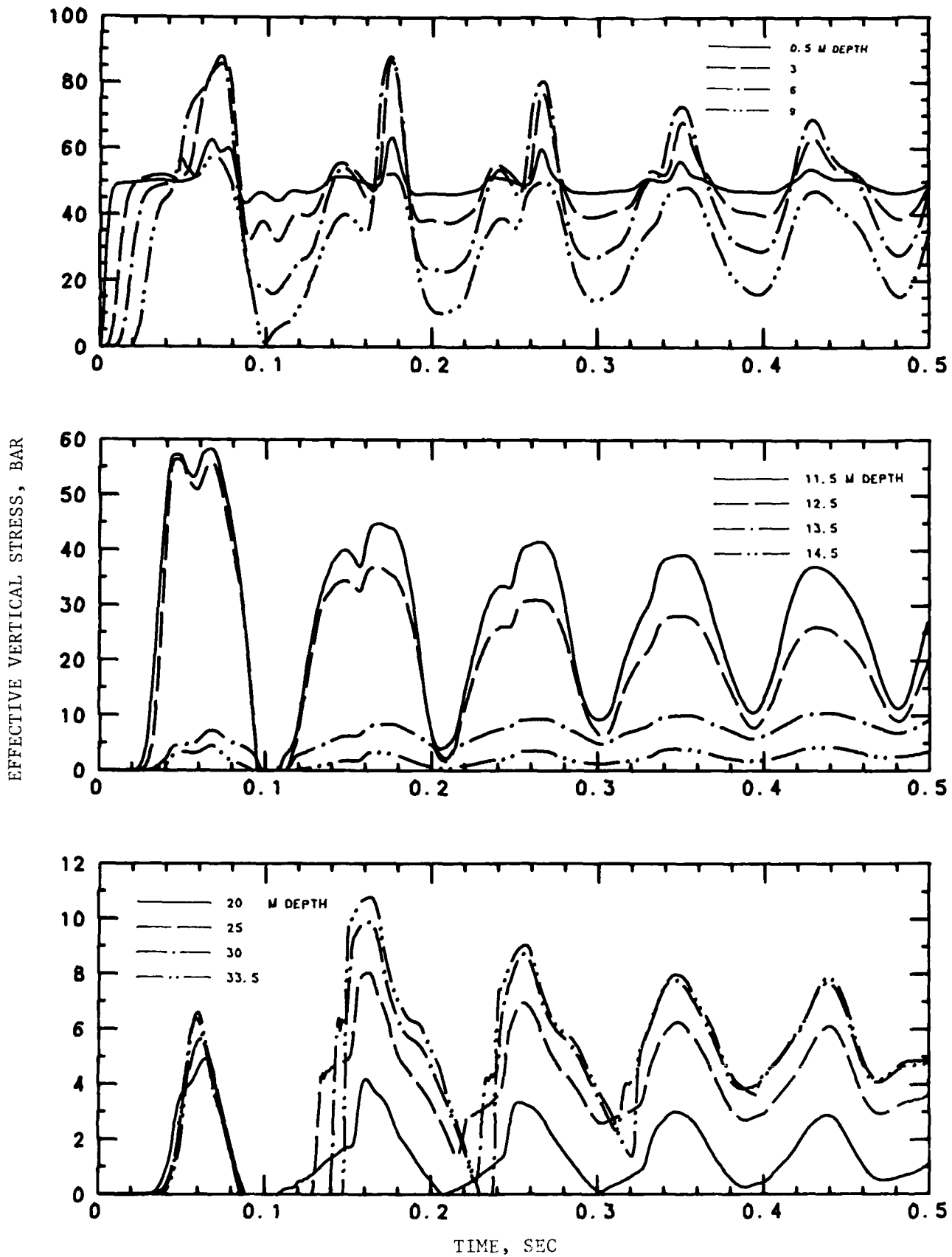


Figure 3.26. Effective vertical stress versus time ($0 < t < 0.5$ sec) at various depths for Case E605.

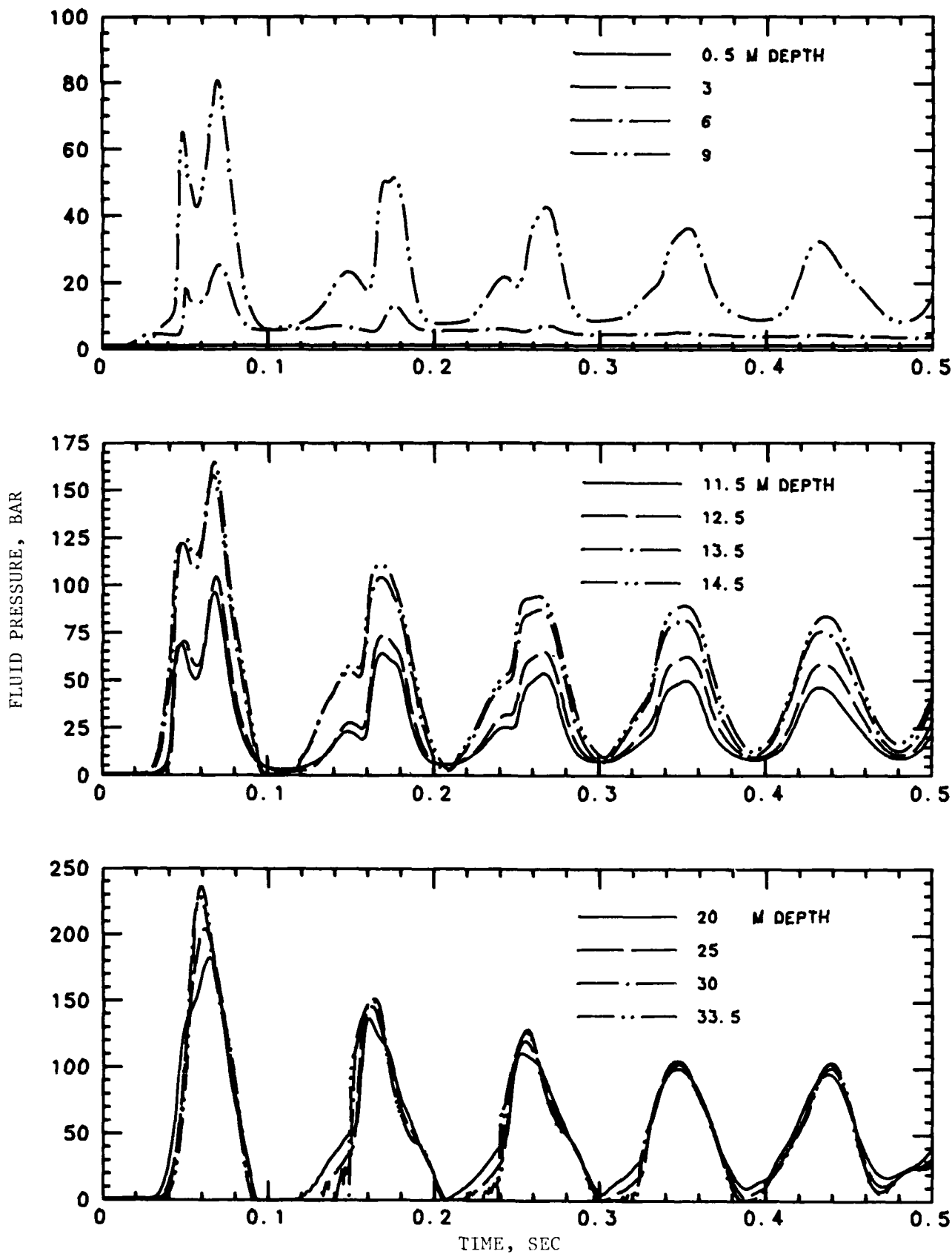


Figure 3.27. Pore-fluid pressure versus time ($0 < t < 0.5$ sec) at various depths for Case E605.

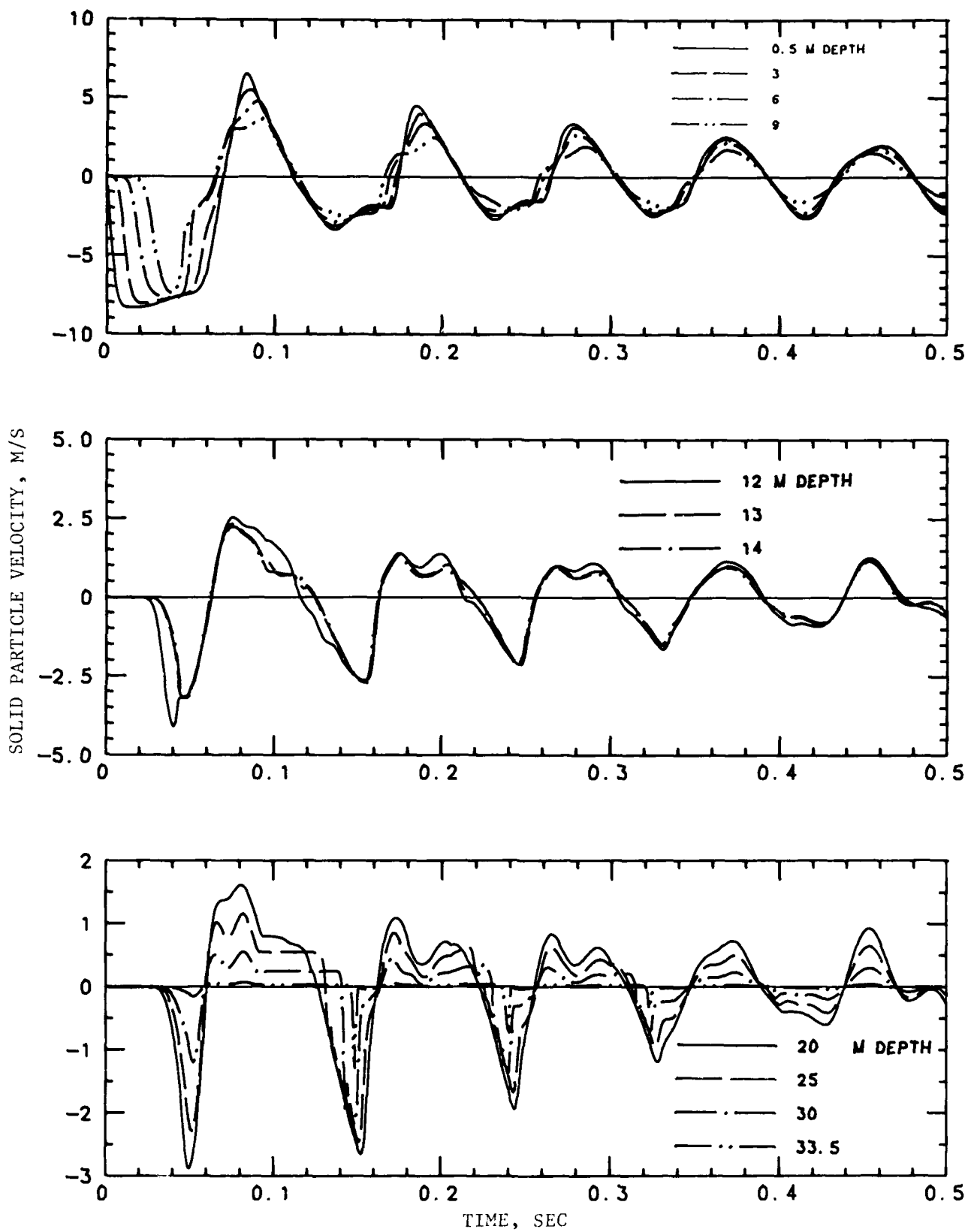


Figure 3.28. Solid particle velocity versus time ($0 < t < 0.5$ sec) at various depths for Case E605.

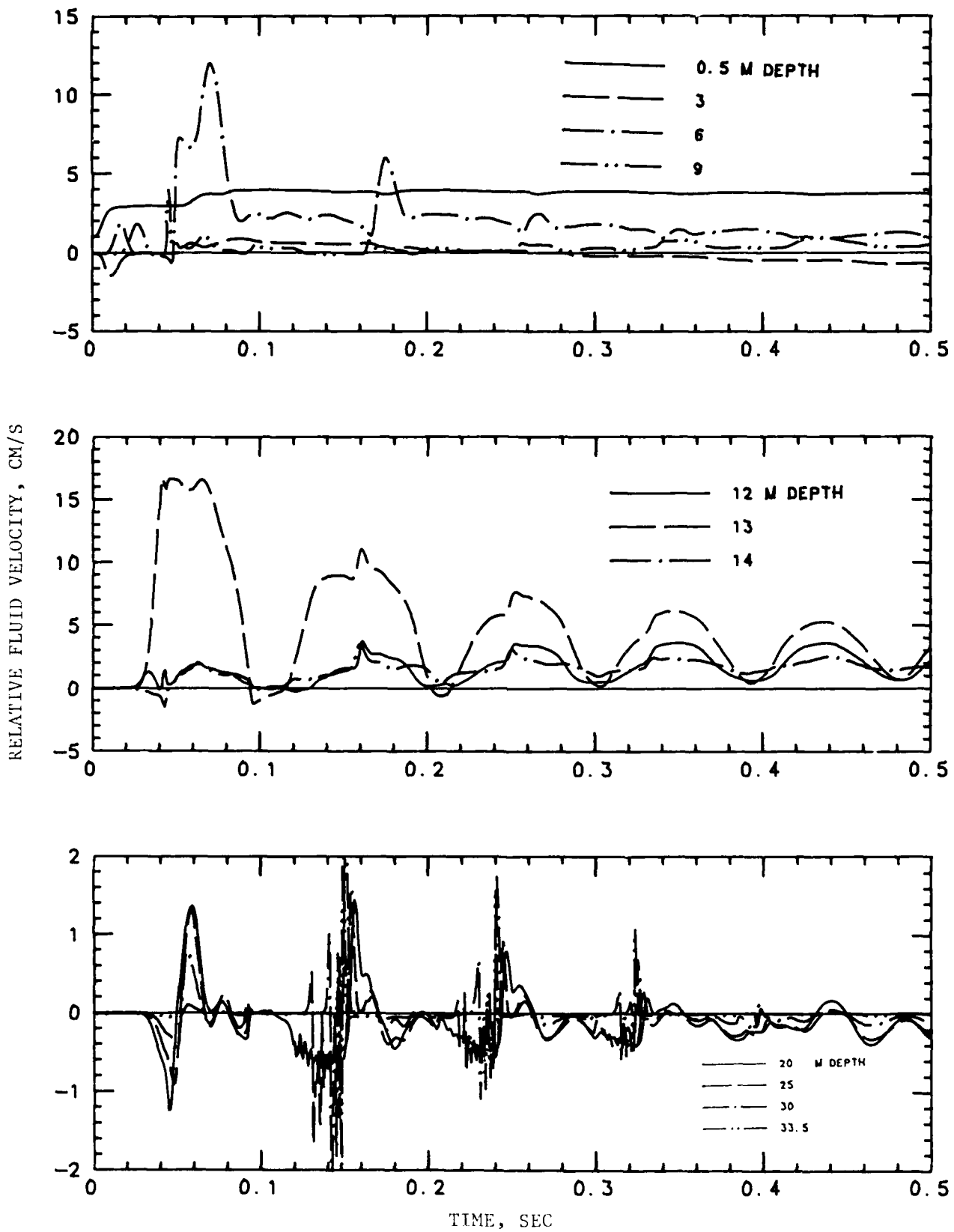


Figure 3.29. Relative fluid velocity versus time ($0 < t < 0.5$ sec) at various depths for Case E605.

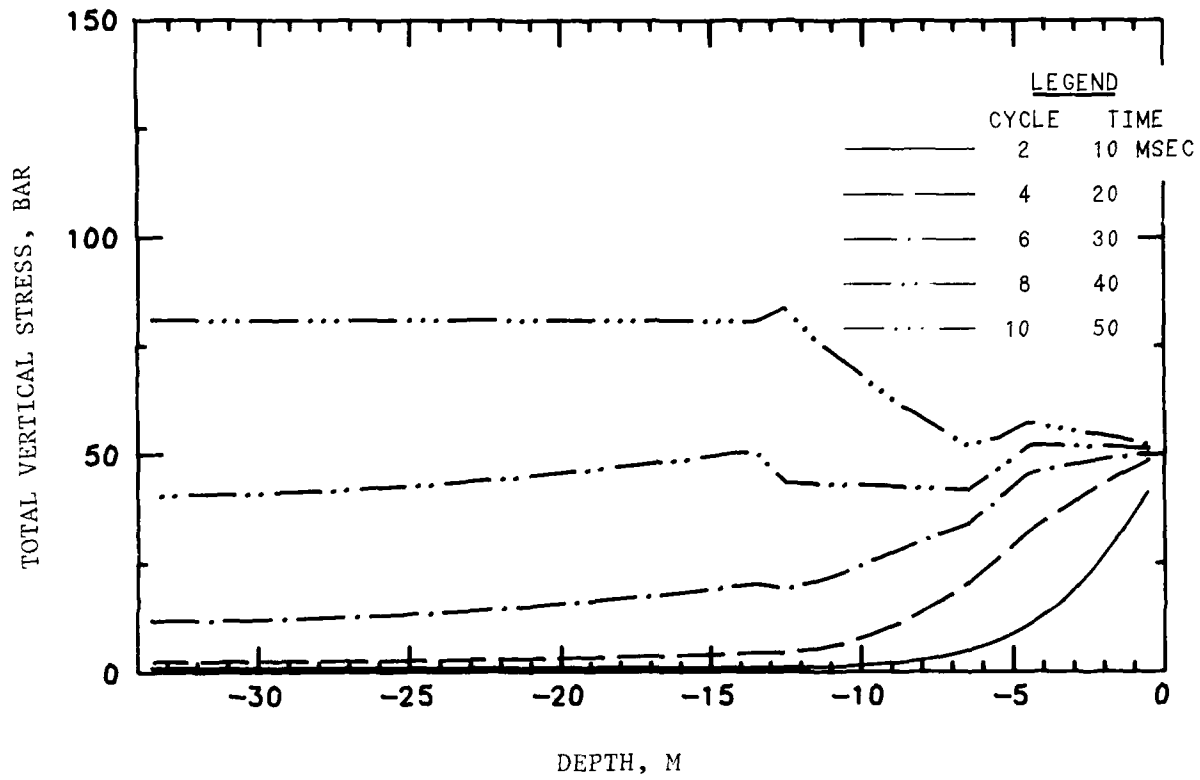


Figure 3.30. Total vertical stress versus depth at various times for Case E607.

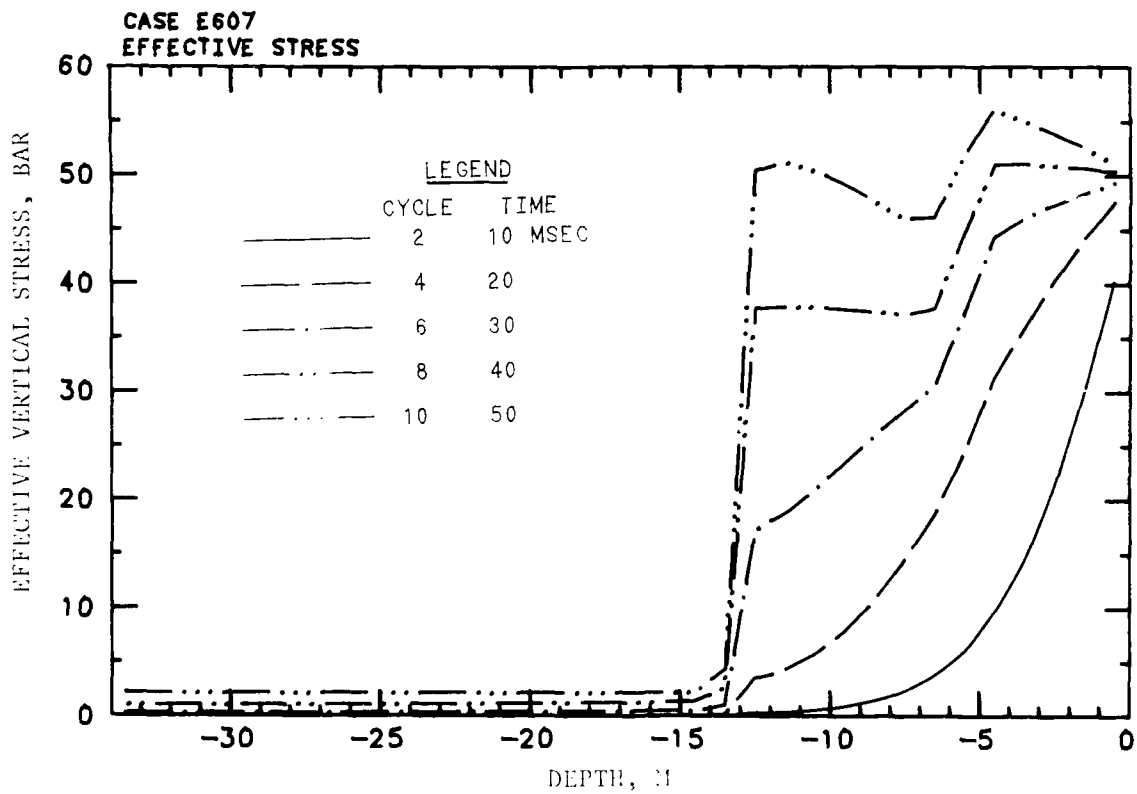
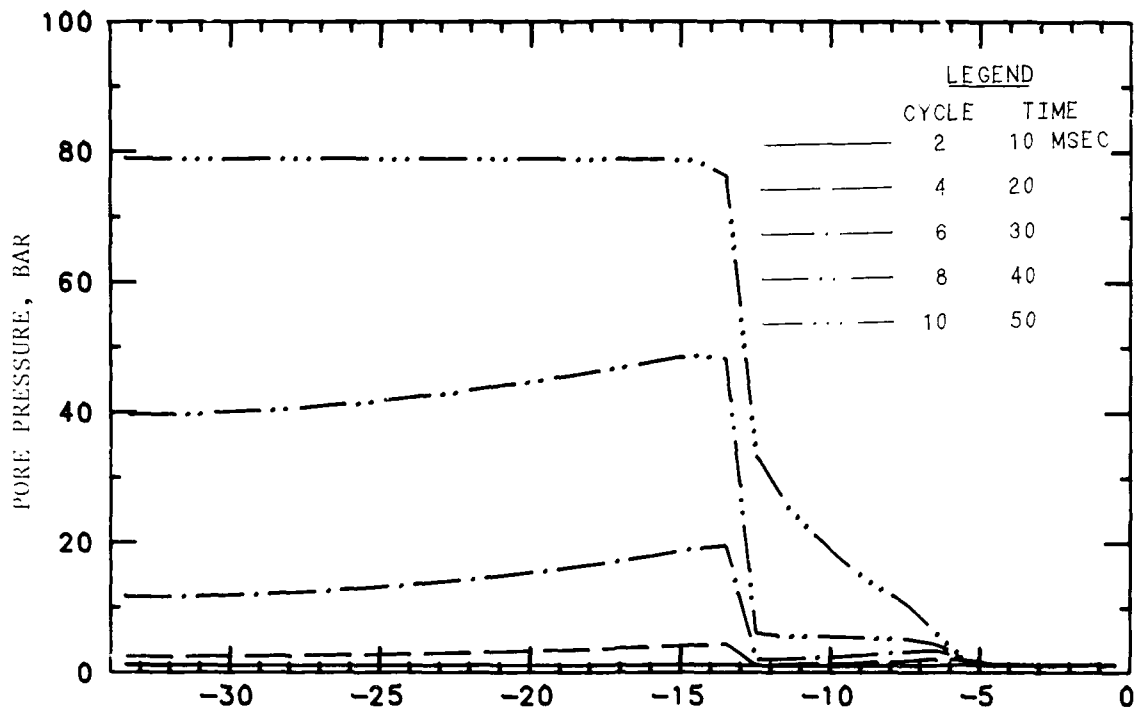


Figure 3.31. Pore-fluid pressure and effective vertical stress versus depth at various times for Case E607.

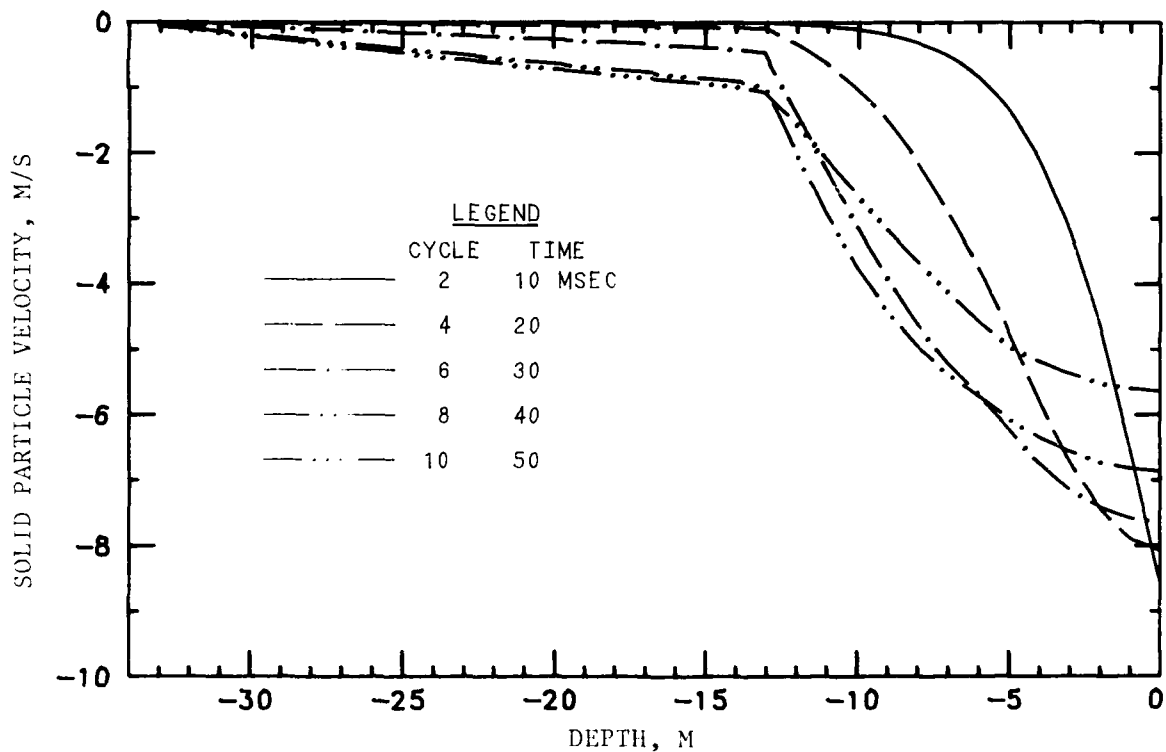
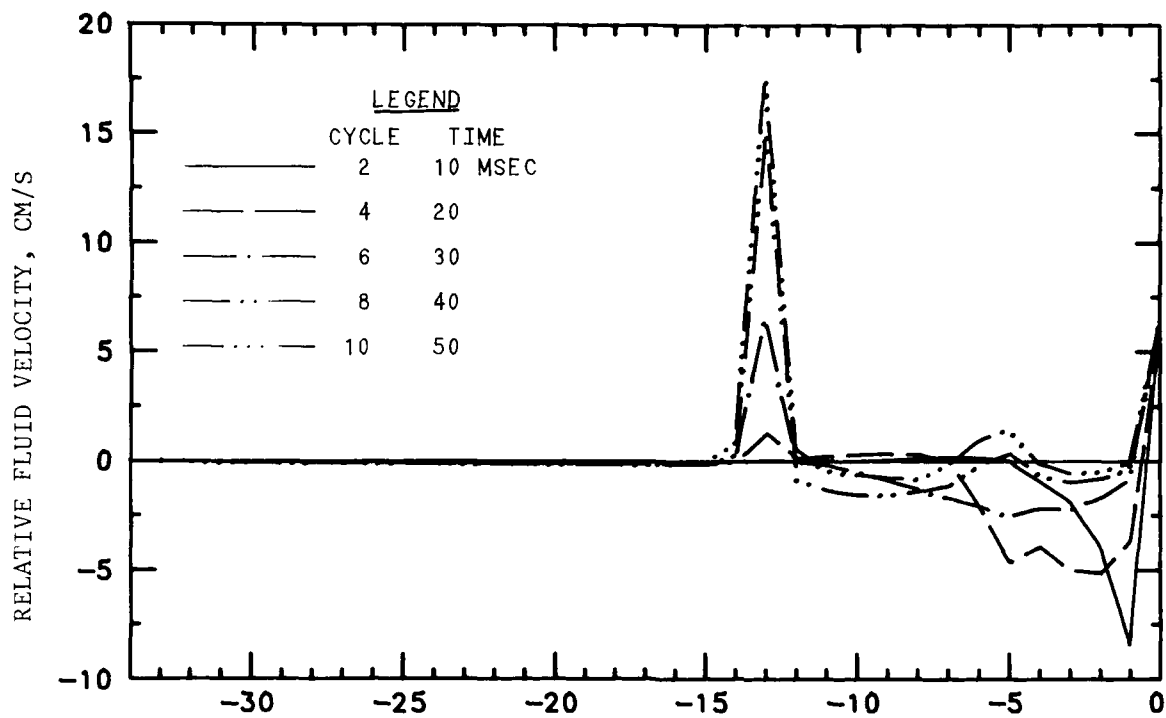


Figure 3.32. Relative fluid velocity and solid particle velocity versus depth at various times for Case E607.

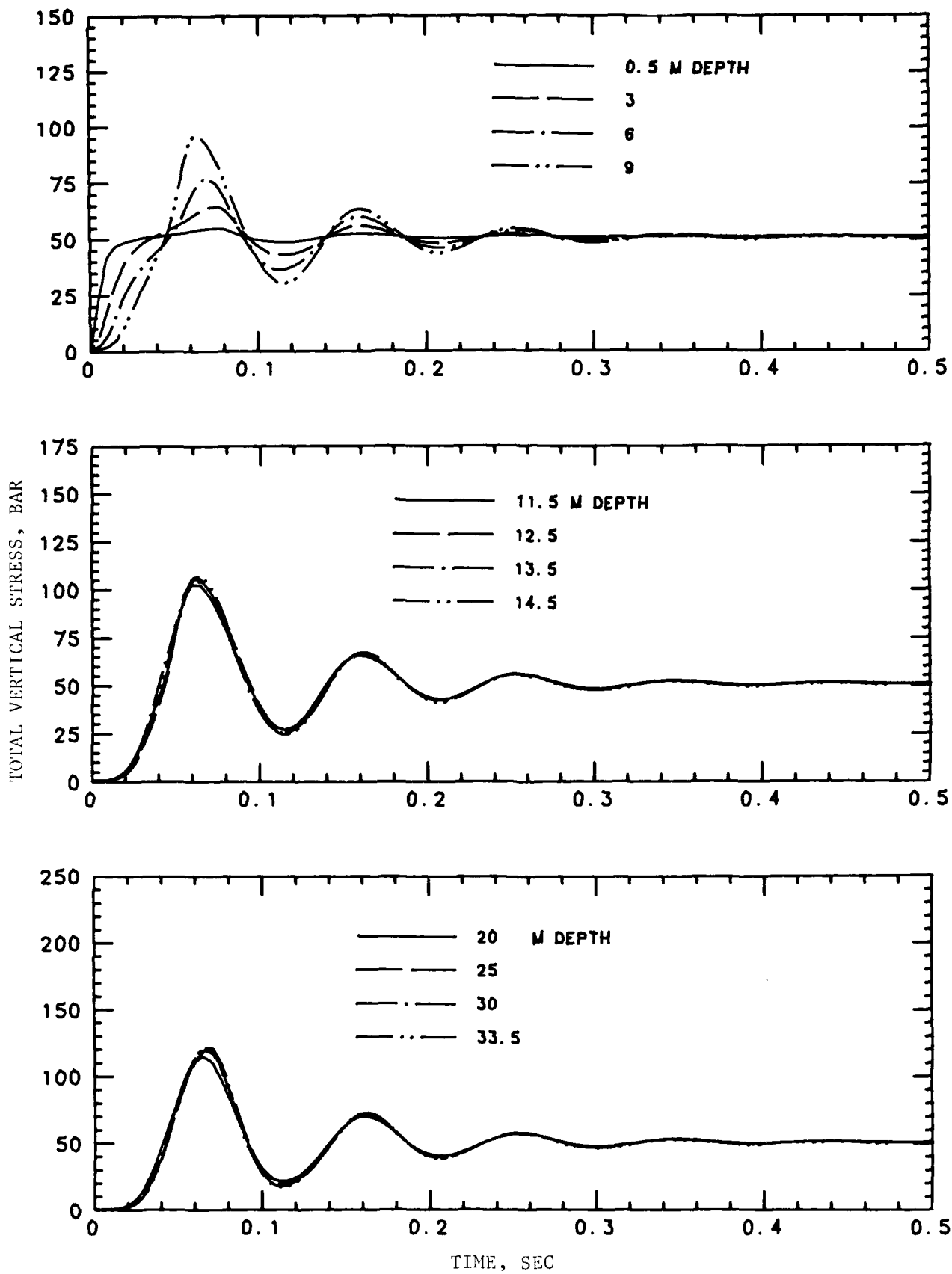


Figure 3.33. Total vertical stress versus time ($0 < t < 0.5$ sec) at various depths for Case E607.

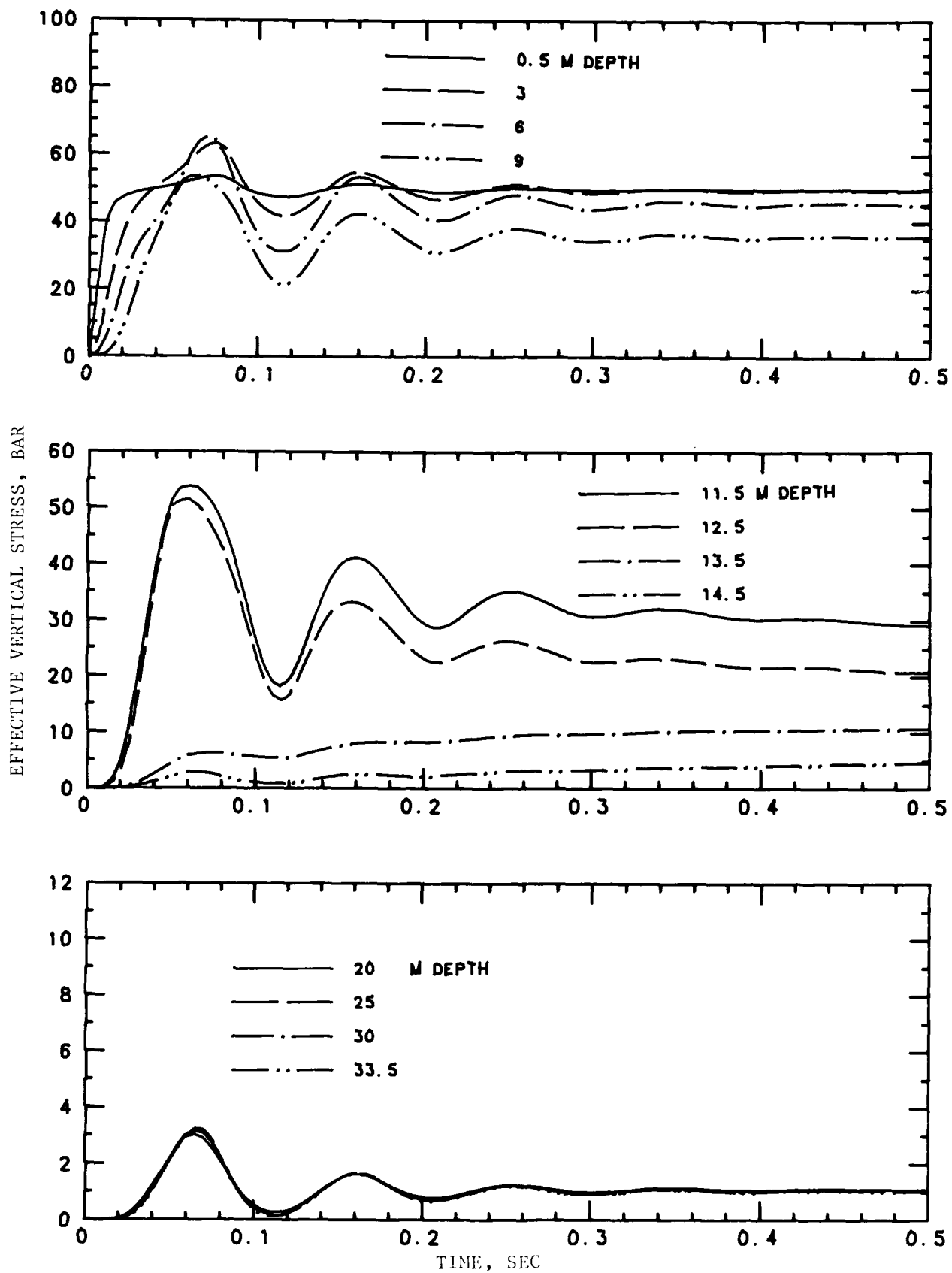


Figure 3.34. Effective vertical stress versus time ($0 < t < 0.5$ sec) at various depths for Case E607.

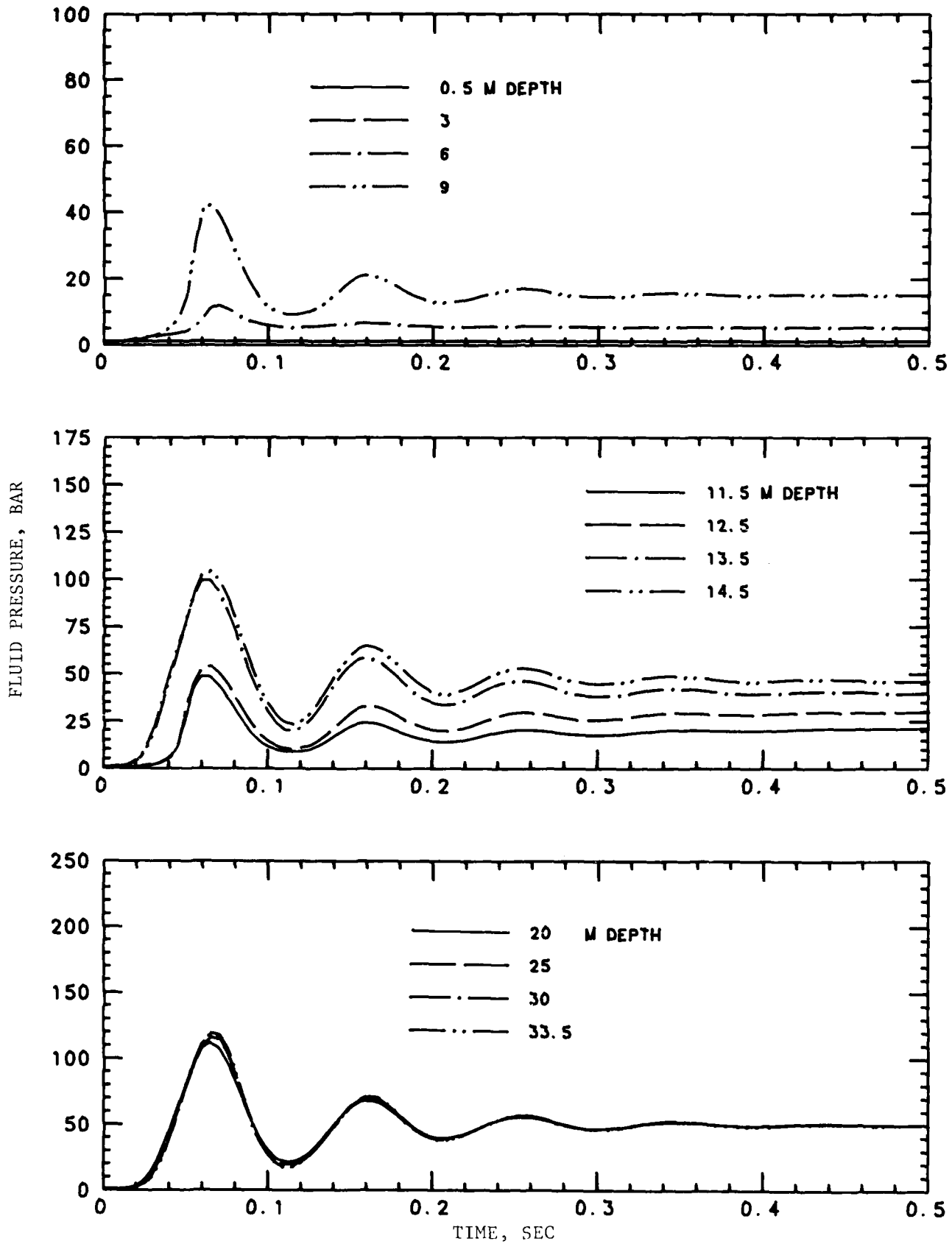


Figure 3.35. Pore-fluid pressure versus time ($0 < t < 0.5$ sec) at various depths for Case E607.

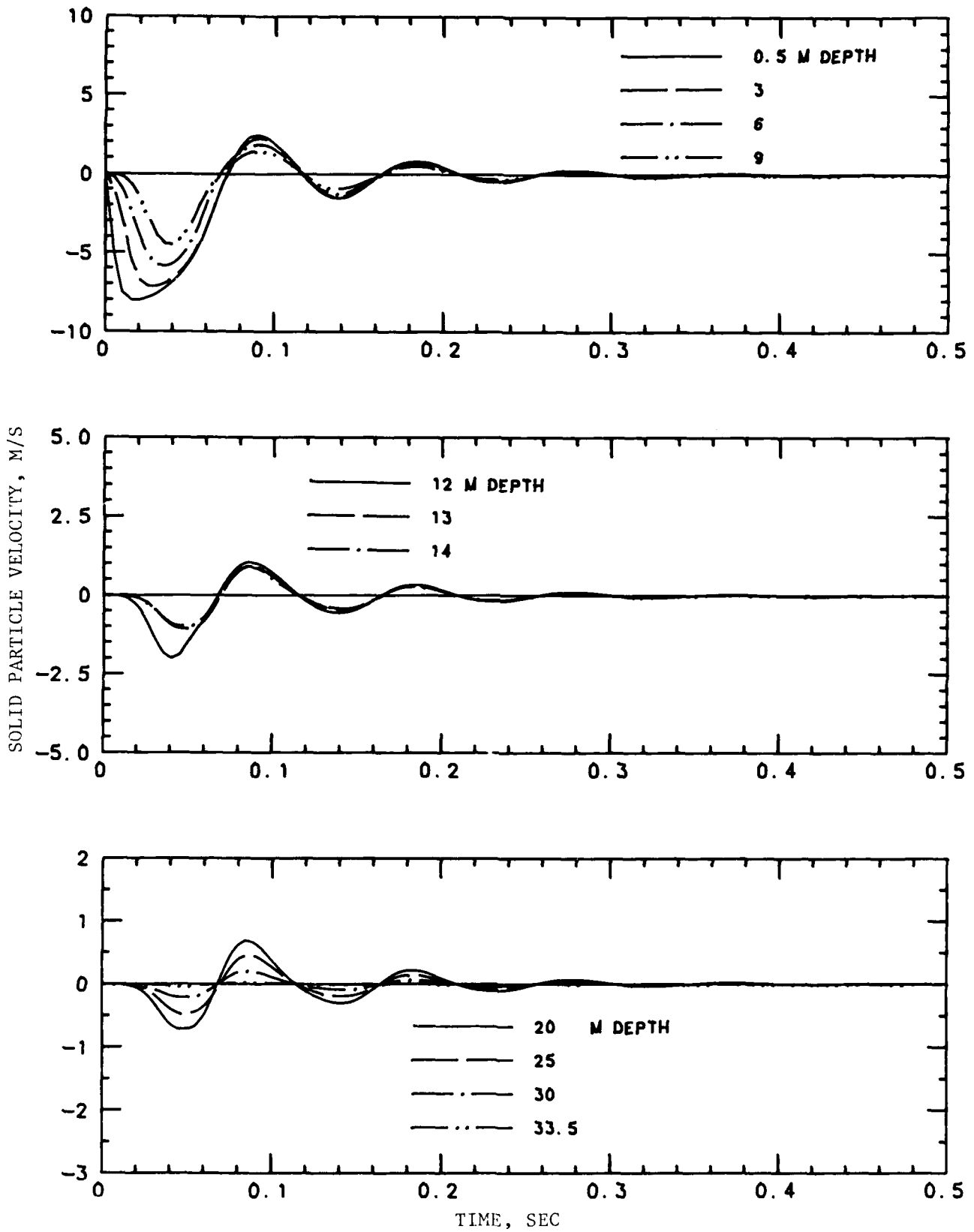


Figure 3.36. Solid particle velocity versus time ($0 < t < 0.5$ sec) at various depths for Case E607.

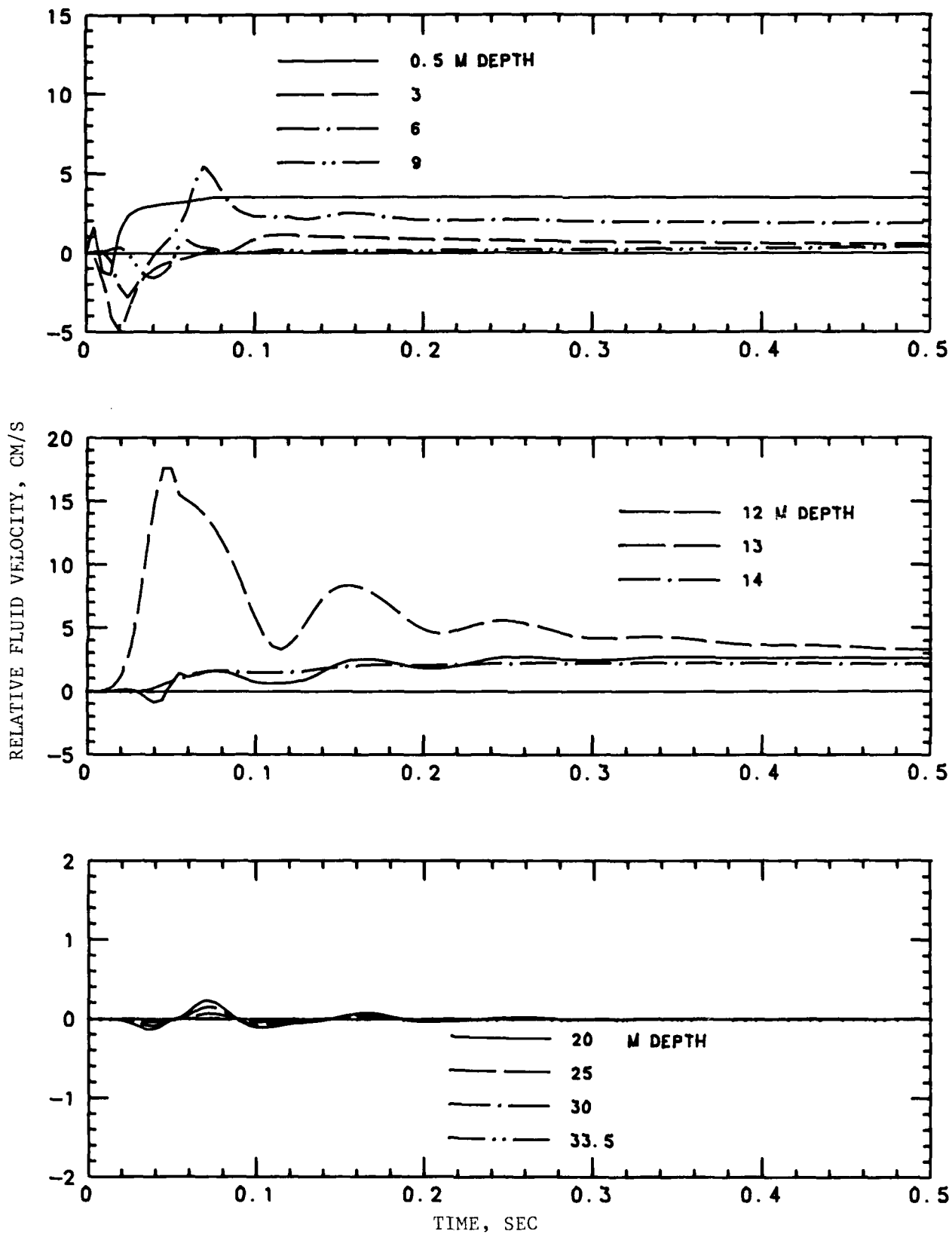


Figure 3.37. Relative fluid velocity versus time ($0 < t < 0.5$ sec) at various depths for Case E607.

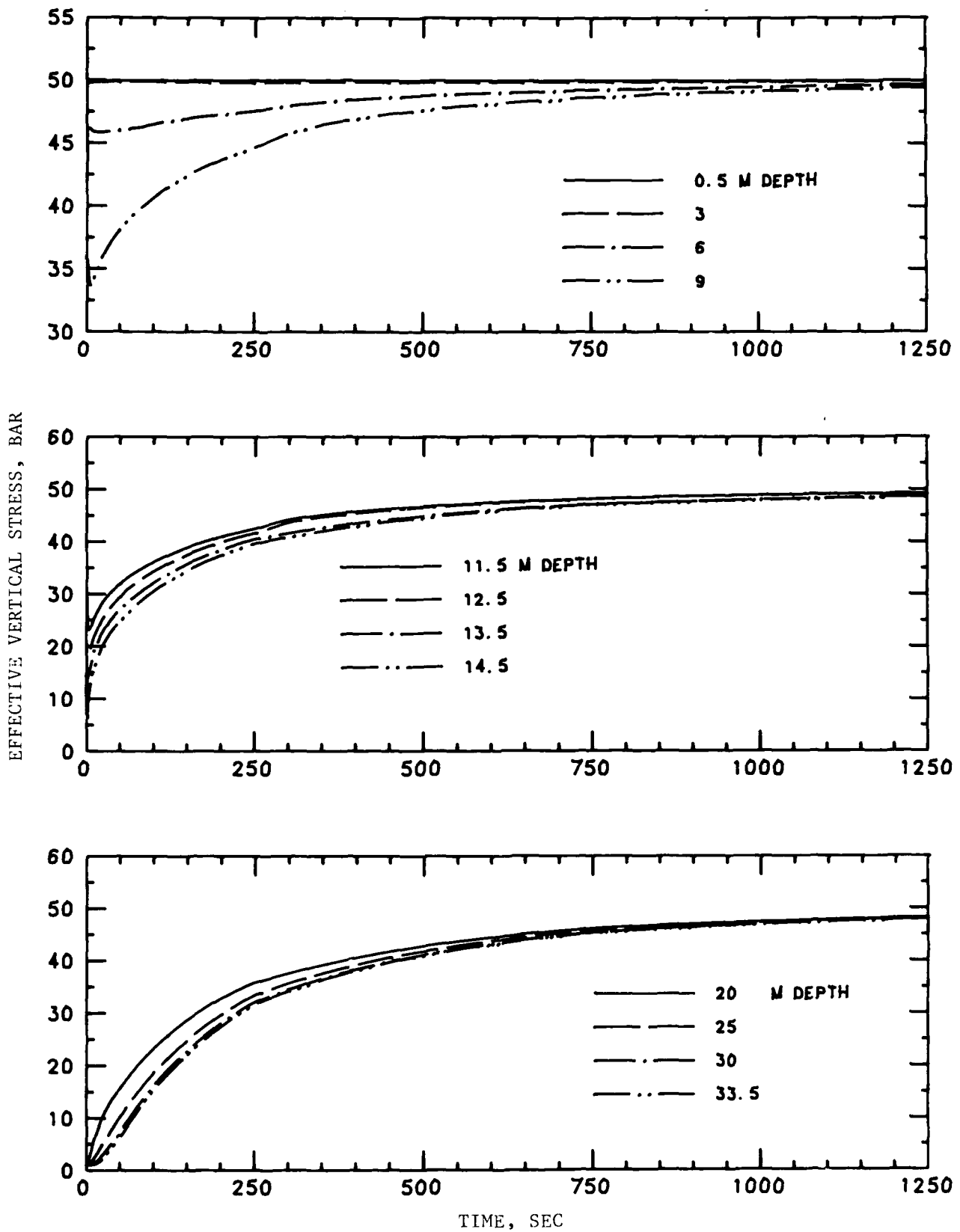


Figure 3.38. Effective vertical stress versus time ($0 < t < 1250$ sec) at various depths for Case E607.

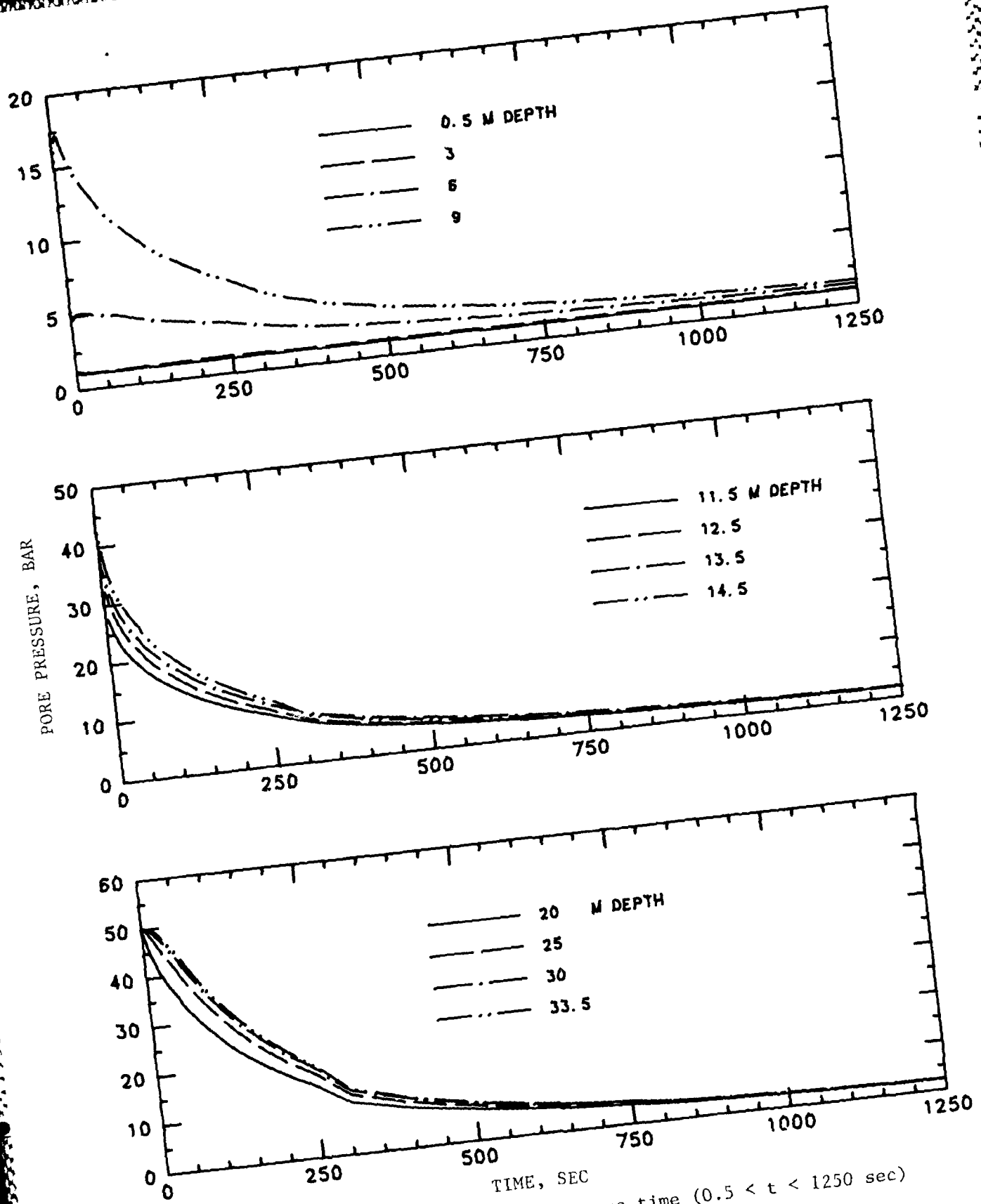


Figure 3.39. Pore-fluid pressure versus time ($0.5 < t < 1250$ sec) at various depths for Case E607.

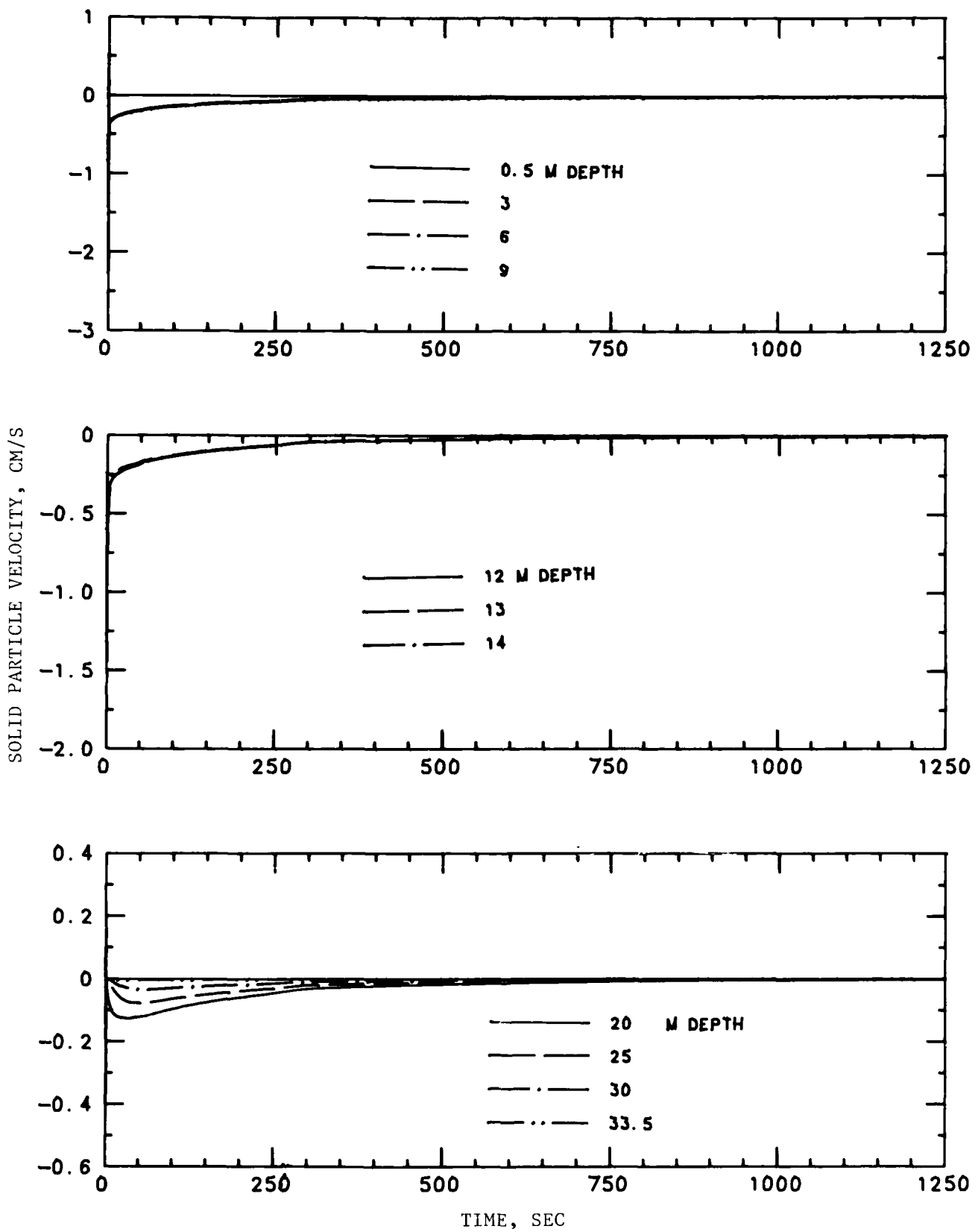


Figure 3.40. Solid particle velocity versus time ($0.5 < t < 1250$ sec) at various depths for Case E607.

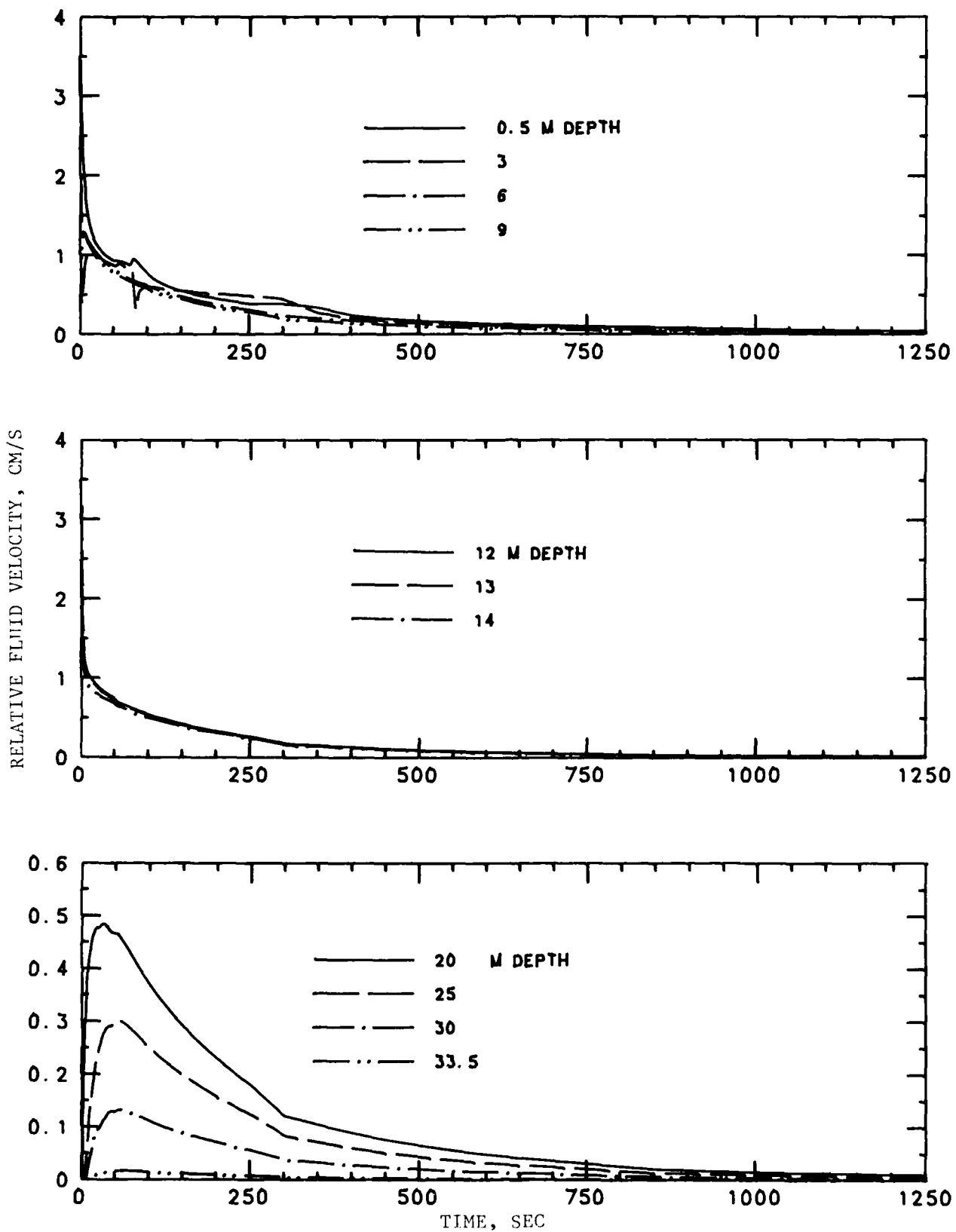


Figure 3.41. Relative fluid velocity versus time ($0.5 < t < 1250$ sec) at various depths for Case E607.

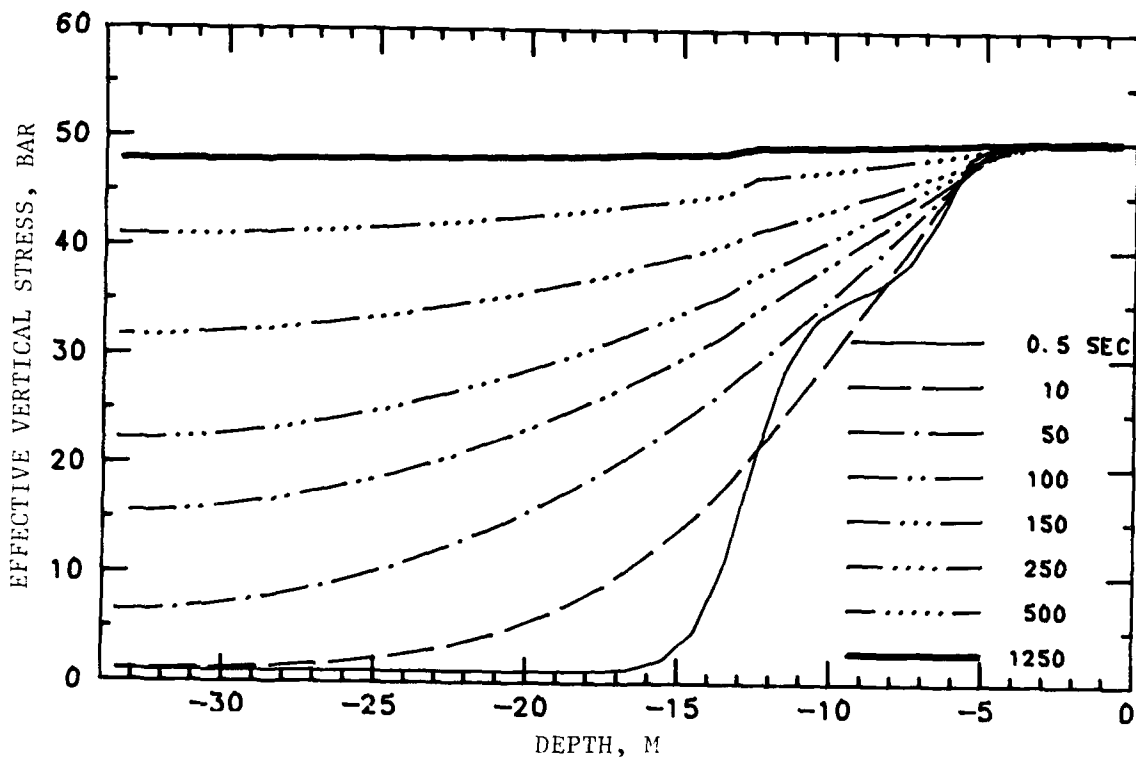
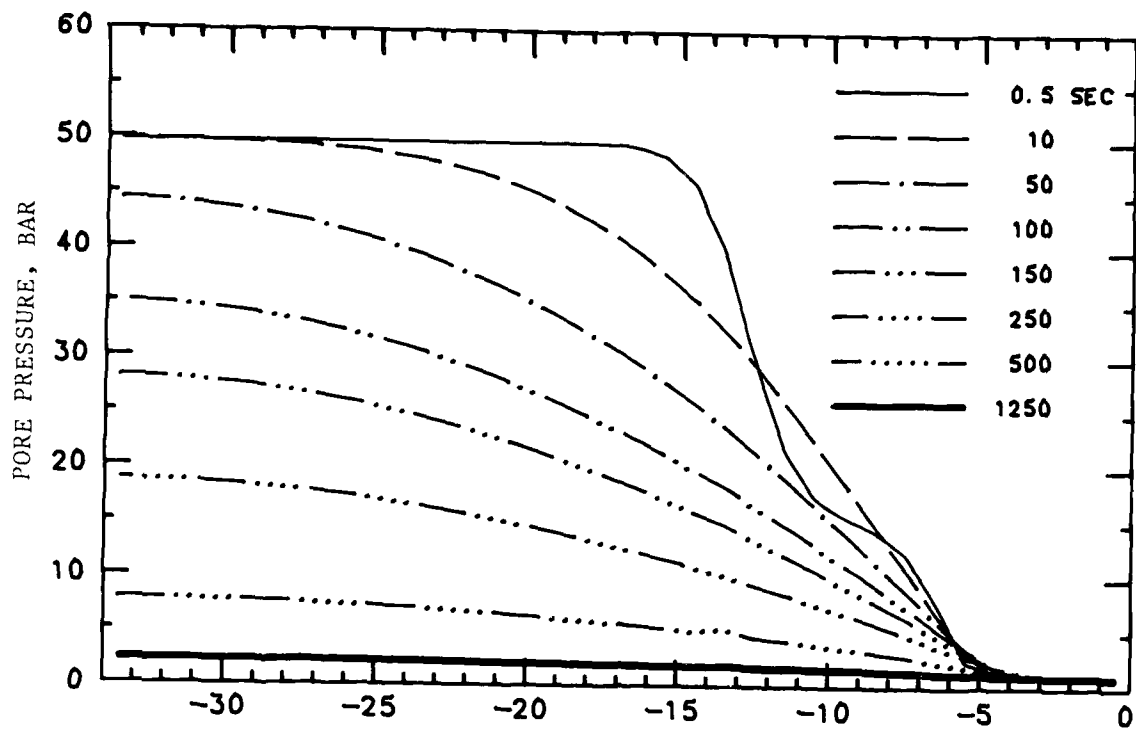


Figure 3.42. Pore-fluid pressure and effective vertical stress versus depth at late times for Case E607.

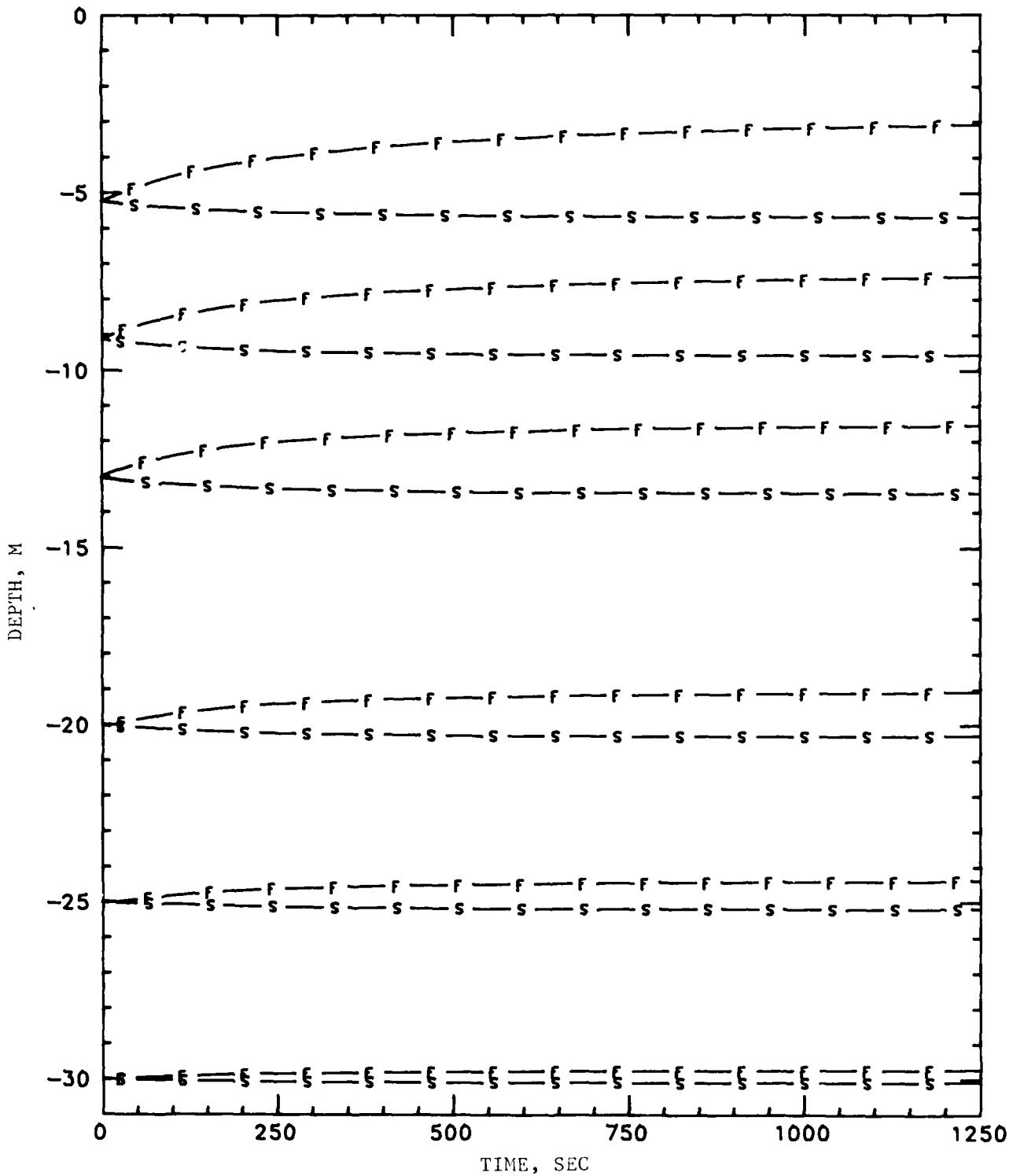


Figure 3.43. Displacements of selected fluid and solid tracers versus time for Case E607.

CHAPTER 4

SUMMARY, CONCLUSIONS, AND RECOMMENDATIONS

As part of a WES study of blast-induced soil liquefaction effects, the M-DICE code was developed to provide a rational methodology for calculating multiphase flows in wet porous soils. The code includes separate treatments of the pore-fluid pressures and soil lattice effective stress behavior, which thus yields the total stress behavior. More importantly, the relative flow of the pore-fluid and soil lattice is also treated by calculating the separate flow of each, including their mutual interactions due to drag. With this fully multiphase modeling, the M-DICE code was used to calculate the ground motions and crater formation from the MISERS BLUFF II-1 high-explosive test event and from a postulated 1 Mt nuclear surface burst (Reference 2-5).

Both M-DICE calculations went beyond the time most cratering codes stop. In so doing, they showed the existence of significant residual pore pressures and associated relative velocities, particularly in the 1 Mt nuclear calculation. The subsequent dissipation and redistribution of these excess pore pressures provide a potential mechanism for significant late time ground motions, including further slumping of the crater slopes and surface settlements. Unfortunately, because M-DICE (like all current numerical cratering and ground shock codes) is formulated in an explicit manner, calculating to very late times is simply not practical. The time step is limited by a stability criterion which is a function of stress wave speeds. An implicit numerical technique, however, would remove the explicit time step limitation, allowing for much larger time steps (factors of 1000 or more), limited by the desired accuracy and perhaps only by the particle velocities.

In this study a 1-D implicit multiphase finite difference formulation which calculates the relative flow and dynamic stress behavior in wet porous soils was developed and incorporated into a computer code called CRIME. Various 1-D test cases are presented which demonstrate the ability of CRIME to efficiently calculate to very late times with time steps much larger (factors > 1000) than permitted by standard explicit techniques. In particular, the loading and subsequent consolidation of realistic layered geology and varying saturation has been successfully simulated as follows: A constant 50-bar overpressure loading is applied to the surface of the top three layers (to 34-m depth) of the MISERS BLUFF II-1 site. The early time ($t < 0.5$ sec) distribution of the load is determined by the degree of saturation. Most of the load is carried by the soil lattice in the dry Material A (0 to 5 m) and by the pore-water in the saturated Material C (13 to 34 m). The late time redistribution (consolidation) of the differential stress loads is governed by the soil permeability (0.01 cm/s). The CRIME calculation of this consolidation process to over 20 minutes is summarized in Figure 3.42; implicit time steps as large as 100 sec (20,000 times explicit) were used.

The 1-D results presented in this report show that the implicit approach we have taken can be used to efficiently calculate relative flow and dynamic stress behavior in wet porous soils. Extending the finite differencing of the governing equations to 2-D would be relatively straightforward, i.e., there will be four unknowns governed by four equations at each grid point in the 2-D formulation instead of the two unknowns and two equations in the 1-D formulation. A computationally efficient algorithm which solves the resulting set of coupled algebraic equations will have to be developed, and the more complicated configuration of various air/water/solid interface boundaries will have to be implicitly resolved.

We recommend that the implicit CRIME formulation be extended to 2-D, and that its efficiency and effectiveness for calculating blast-induced cratering and ground shock phenomenology to very late times be demonstrated.

REFERENCES

1. Baladi, G. Y. and Barnes, D. E. June 1984. "LAYER Code Calculations for the MISERS BLUFF II-1 Event Using Total Stress and Effective Stress Constitutive Models," Technical Report (review draft), U. S. Army Engineer Waterways Experiment Station, Vicksburg, MS.
2. Rosenblatt, M., Hassig, P. J., Schlamp R. J., Garza, G. A., Lee, H. N., Killian, B., and Veyera G. E. February 1986. "Blast-Induced Multiphase Flow in Wet Porous Soils: Report 1, Early Time Simulation of the MISERS BLUFF II-1 Event Using Multiphase Mixture and Effective Stress Constitutive Models," CRT 3749-1F, California Research and Technology, Inc., Chatsworth, CA.
3. Hassig, P. J., Rosenblatt, M., Garza, G. A., and Veyera, G. E. May 1986. "Blast-Induced Multiphase Flow in Wet Porous Soils: Report 2, Late Time M-DICE Simulation of the MISERS BLUFF II-1 Event," CRT 3749-2F, California Research and Technology, Inc., Chatsworth, CA.
4. Hassig, P. J., Garza, G. A., Melendez, R. M., and Rosenblatt, M. March 1987. "Blast-Induced Multiphase Flow in Wet Porous Soils: Report 3, Early Time M-DICE Simulation of a 1 Mt Nuclear Surface Burst at the MISERS BLUFF II-1 Site," CRT-TM-3730-01, California Research and Technology, Inc., Chatsworth, CA.
5. Hassig, P. J., Rosenblatt, M., and Garza, G. A. May 1987. "Blast-Induced Multiphase Flow in Wet Porous Soils: Report 4, Late Time M-DICE Simulation of a 1 Mt Nuclear Surface Burst at the MISERS BLUFF II-1 Site," CRT 3749-F, California Research and Technology, Inc., Chatsworth, CA.
6. Carmen, P. C. 1956. Flow of Gases Through Porous Media, Butterworths Scientific Publications, London.
7. Richtmyer, R. D. and Morton, K. W. 1967. Difference Methods for Initial-Value Problems, Second Edition, John Wiley and Sons, New York.
8. Prevost, J. H. 1985. "Wave Propagation in Fluid-saturated Porous Media: An Efficient Finite Element Procedure," International Journal of Soil Dynamics and Earthquake Engineering, Vol 4, No. 4, pp 183-202.

DISTRIBUTION LIST

DEPARTMENT OF DEFENSE

Director
 Defense Nuclear Agency
 ATTN: DFSP (Dr. G. W. Ullrich)
 SPWE (Mr. C. B. McFarland)
 SPWE (MAJ Mike Pelkey)
 SPWE (Dr. E. J. Rinehart)
 Technical Library
 Washington, DC 20305-1000

Director
 Defense Nuclear Agency
 Nevada Operations Office
 ATTN: TDNV (Mr. J. W. LaComb)
 P.O. Box 98518
 Las Vegas, NV 89193-8518

Director
 Defense Advanced Research Project Agency
 ATTN: Technical Library
 1400 Wilson Blvd.
 Arlington, VA 22209

Director
 Defense Intelligence Agency
 ATTN: Technical Library
 Washington, DC 20301-6111

Defense Technical Information Center
 ATTN: TC
 Cameron Station
 Alexandria, VA 22314

DEPARTMENT OF THE ARMY

Commander
 US Army Corps of Engineers
 ATTN: CERD-L
 CERD-M (Mr. B. O. Benn)
 CEIC-ET (Mr. R. L. Wight)
 CEIM-SL
 Washington, DC 20314-1000

Division Engineer
 US Army Engineer Division, Huntsville
 ATTN: CEHND-SR
 P.O. Box 1600
 Huntsville, AL 35807-4301

Director
 US Army Construction Engineering Research
 Laboratory
 ATTN: Technical Library
 P.O. Box 4005
 Champaign, IL 61820-1305

District Engineer
 US Army Engineer District, Omaha
 ATTN: CEMRO-ED-S (Mr. Bob Kelley)
 CEMRO-ED-CH (Mr. Bill Gauber)
 215 N. 17th Street
 Omaha, NE 68102-1278

Commander/Director
 US Army Cold Regions Research and
 Engineering Laboratory
 ATTN: Technical Library
 72 Lyne Road
 Hanover, NH 03061-1290

DEPARTMENT OF THE ARMY (CONTINUED)

Commandant
 US Army Engineer School
 ATTN: ATZA-CD (COL Fred Parker)
 Technical Library
 Fort Belvoir, VA 22060-5281

Commander
 Harry Diamond Laboratories
 Department of the Army
 ATTN: Technical Library
 2800 Powder Mill Road
 Adelphi, MD 20783-1197

Commander
 US Army Nuclear and Chemical Agency
 ATTN: Technical Library
 7500 Backlick Road, Bldg. 2073
 Springfield, VA 22150

DEPARTMENT OF THE NAVY

Naval Civil Engineering Laboratory
 ATTN: Technical Library
 Port Hueneme, CA 93043

Naval Facilities Engineering Command
 200 Stoval Street
 ATTN: Technical Library
 Alexandria, VA 22332

DEPARTMENT OF THE AIR FORCE

Air Force Institute of Technology
 Air University
 ATTN: Technical Library
 Wright-Patterson AFB, OH 45433

Air Force Office of Scientific Research
 ATTN: Technical Library
 Bolling AFB, DC 20332

Air Force Weapons Laboratory (AFSC)
 ATTN: NTEDE (Mr. J. N. Thomas)
 Technical Library
 Kirtland AFB, NM 87117-6008

Air Force Engineering and Services Center
 (AFSC)
 ATTN: Technical Library
 Tyndall AFB, FL 32403

Commander
 Ballistic Missile Office (AFSC)
 ATTN: MYEB (LTC D. H. Gage)
 Technical Library
 Norton AFB, CA 92409-6468

DEPARTMENT OF ENERGY

Lawrence Livermore National Laboratory
 ATTN: Technical Library
 P.O. Box 808
 Livermore, CA 94550

Los Alamos National Laboratory
 ATTN: Technical Library
 P.O. Box 1663
 Los Alamos, NM 87545

DISTRIBUTION LIST (CONCLUDED)

DEPARTMENT OF ENERGY (CONTINUED)

Sandia National Laboratories
ATTN: Technical Library
P.O. Box 5800
Albuquerque, NM 87185

Sandia National Laboratories
ATTN: Technical Library
Livermore, CA 94550

DEPARTMENT OF DEFENSE CONTRACTORS

Mr. J. L. Bratton
Applied Research Associates, Inc.
4300 San Mateo Blvd., NE, Suite A220
Albuquerque, NM 87110

Mr. S. E. Blouin
Applied Research Associates, Inc.
Box 120A, Waterman Road
South Royalton, VT 05068

Mr. J. L. Drake
Applied Research Associates, Inc.
3202 Wisconsin Avenue
Vicksburg, MS 39180

Dr. J. G. Trullio
Applied Theory, Inc.
930 S. LaBrea Avenue
Los Angeles, CA 90036

Dr. Y. Marvin Ito (10 copies)
Mr. S. H. Schuster
Mr. K. N. Kroeyenhagen
Mr. Martin Rosenblatt
Mr. P. J. Hassig
California Research & Technology, Inc.
20943 Devonshire Street
Chatsworth, CA 91311-2376

Technical Library
New Mexico Engineering Research Institute
University of New Mexico
Box 25, University Station
Albuquerque, NM 87131

Mr. J. G. Lewis
Dr. Don Simons
Dr. M. M. Balaban
R&T Associates
P.O. Box 2695
Marina del Rey, CA 90291

Dr. H. B. Read
Mr. Steve Payton
Mr. Norton Biren
C-Cinet
P.O. Box 1620
La Jolla, CA 92038-1620

Dr. Lynn Seaman
391 International
221 Ravenswood Avenue
Menlo Park, CA 94025

Mr. Norman Ligner
Dr. M. J. Katona
TRW Defense Systems Group
P.O. Box 1210
San Bernardino, CA 92402

DEPARTMENT OF DEFENSE CONTRACTORS (CONTINUED)

Dr. D. J. Ness
TRW Defense and Space Systems Group
One Space Park, Bldg. 134/Rm 9835
Redondo Beach, CA 90278

Dr. I. S. Sandler
Weidlinger Associates
333 Seventh Avenue
New York, NY 10001

Dr. Jeremy Isenberg
Weidlinger Associates
620 Hansen Way, Suite 100
Palo Alto, CA 94304

Dr. R. T. Allen
Dr. Dan Patch
Pacifica Technology
P.O. Box 148
Del Mar, CA 92014

END

DATE

FILMED

8-88

DTIC